Design and Control of a Cable-Driven Sectorial Rotary Actuator for Open-Loop Force Control

Jordan Downey Neal

Thesis submitted to the faculty of the
Virginia Polytechnic Institute and State University
in partial fulfillment of the requirements for the degree of

Master of Science
In
Mechanical Engineering

Tomonari Furukawa, Chair
Dennis Hong, Co-Chair
Alfred Wicks

September 25, 2015
Blacksburg, VA

Keywords: Cable Drive, Delta, Force Control, Haptic, Impedance, Open-Loop, Rotary Actuator

Design and Control of a Cable-Driven Sectorial Rotary Actuator for Open-Loop Force Control

Jordan Downey Neal

ABSTRACT

This thesis focuses on the detailed design, implementation, and testing of a unique high performance rotary actuator for use in a custom haptic force feedback device. This six degree of freedom (DoF) position input and three DoF force output haptic device is specifically designed to recreate force sensations with the goal of improving operator performance in remote or simulated environments. By upholding the strict design principles of an ideal force-source actuator, the developed actuator and consequently the haptic controller can successfully replicate forces accurately and realistically. In the comprehensive presentation of this design, numerous analytical tools are also developed and presented with the intention of them being resourceful in the design or improvement of other haptic actuators, specifically cable-driven force feedback designs. These tools which include a linear system model can be valuable not only in the development but in the control of cable-driven actuators.

Due to the imposed design criteria, the developed 1.045 Nm (1.359 Nm peak) cable-driven sectorial rotary actuator exhibits numerous properties that are desired in an open-loop force controlled actuator. These properties include low inertia (6.53e-04 $kg \cdot m^2$), low perceived mass (0.102 kg), small torque resolution (3.84e-04 Nm), small position resolution (21.5 arcsec), and high bandwidth (300 Hz). Due to the efficient cable transmission the design is also backdrivable, isotropic, low friction, and zero backlash. As a result of these numerous intrinsic properties, a high fidelity force feedback haptic actuator was conceived and is presented in this thesis.

This work was supported by DARPA through grant N65236-12-1-1002.

Acknowledgements

There are numerous people who have supported me in what is culminating in this thesis and I would like to acknowledge them in this section. First I would like to recognize my committee, Dr. Furukawa, Dr. Hong, and Dr. Wicks. Thank you all for your guidance throughout my graduate studies. I have learned invaluable amounts of knowledge, both in and out of the classroom, from all of you and know that you have helped to make me the engineer I am today.

To my labmates both past and present, it has been an unforgettable ride. Few can say that they have accomplished what we have and I could not be any more proud to say I worked with each and every one of you. I wish you all great success in your future endeavors and hope we cross paths again.

To my parents, thank you for all that you have done throughout my college studies. It has been quite the journey and you both have been nothing but encouraging and supportive the entire way. I cannot thank you both enough for all that you have done, but know that you both have had an undeniably influential and positive impact on my life.

To my wife, thank you for continually motivating me and pushing me towards my goals. There were multiple times where I faltered and you were there to get me through it. Without your support and encouragement I would not be where I am today.

And to the rest of my family and friends, thank you for always showing a deep interest in my work and supporting me in all that I do. I could not have asked to be surrounded by a greater group of people then all of you. I appreciate all that you have done and continue to do and know that your support does not go unappreciated.

Thank you all.

All photos are by the author unless otherwise noted.

Table of Contents

List of Figures

List of Tables

Chapter 1

Introduction

Haptics refers to anything that pertains to the sense of touch. In the robotics and virtual reality communities however haptics has a more specific meaning. In these communities haptics refers to the real or simulated touch interactions between humans and physical devices. These physical devices, or haptic interfaces, are specifically designed with consideration to human factors [1], [2], [3] to recreate touch sensations with the goal of improving operator performance in remote or simulated environments.

Due to the number and sensitivity of the various sensory systems humans possess, designing effective haptic devices is no easy task. What this thesis seeks to present is the design of an actuator for use in a haptic force-feedback device. The actuator is arguably the most important element of any haptic interface, and no level of design can recover from poor actuation especially when implemented in open-loop control. The actuator presented is to be employed in the haptic controller also touched upon in this thesis. This controller was designed to be a general purpose haptic interface with the intention of it being used for mobile robotic platform teleoperation.

This study is significant because of the growing impact haptics are having on society as they continually get integrated into new products. Haptics are becoming more mainstream, and specifically force feedback devices are slowly finding their way to consumer markets. However, arguably one of the greatest limitations of haptic devices is also related to its actuation. Thus any improvements or contributions in actuator design can lead to significant contributions in the implementation of haptic interfaces.

1.1 Objective

This thesis seeks to present the detailed design, implementation, and testing of a unique high performance rotary actuator for use in a custom haptic force feedback device. By upholding the strict design principles of an ideal force-source actuator, the developed actuator and

consequently the corresponding haptic controller should be able to successfully replicate forces accurately and realistically. In the comprehensive presentation of this design, numerous analytical tools are also to be developed and presented with the intention of them being resourceful in the design or improvement of other haptic actuators, specifically cable-driven force feedback designs. These tools which include a linear system model can be valuable not only in the development but in the control of cable-driven actuators.

1.2 Outline

Chapter 2 comprises an overview of the research previously conducted for impedance-class haptic devices. This chapter includes current designs for haptic interfaces, the design principles that define these designs, and the transmissions that drive them.

Chapter 3 presents a broad overview of the haptic controller in which the developed actuator is implemented. This chapter discusses the configuration of the chosen design, its corresponding kinematics and dynamics, its workspace, its force feedback properties, and a brief introduction to its actuation system.

Chapter 4 details the design and analysis of the developed actuator. This chapter includes a comprehensive discussion of each component of the design and its corresponding impact on the performance of the actuator.

Chapter 5 presents the actuator model designed to simulate and weigh design tradeoffs in the development of the actuator. This chapter contains the state space description of the model as well as its corresponding parameters.

Chapter 6 covers the experiments performed on the actuator to validate the design. These tests include a frequency response and a step response, as well as their corresponding performance measures.

Chapter 7 summarizes the work completed in this thesis and makes recommendations for future work to be completed that is relevant to the design of the actuator.

Chapter 2

Literature Review

Haptic interfaces typically fall into two categories, kinesthetic or cutaneous devices. Kinesthetic devices are based on position and force information whereas cutaneous devices are based on tactile information. This literature review focuses on kinesthetic haptic devices, specifically force-feedback, as the objective of this thesis is to present the design of an actuator for a kinesthetic haptic interface.

A kinesthetic device typically operates in a loop where the device senses the position or force from the operator which is then applied to a simulated or remote environment. The response from the environment is then conveyed back to the operator through the device via position or force with the intention of replicating the experience the operator would have if actually interacting with a real environment.

2.1 Haptic Impedance-Class Interface Design

Kinesthetic haptic interfaces typically fall into two categories in terms of kinematic structure, these being serial and parallel [4]. A serial kinematic structure is made up of a single chain of linkages, connected by joints, from the base to the end effector where the position of each linkage is dependent on the position of the preceding linkages. On the other hand, a parallel kinematic structure is made up of multiple chains of linkages connected by joints that independently connect the base to the end effector. Parallel structures are usually characterized and easily identified by a closed kinematic loop. In comparison to serial mechanisms, parallel mechanisms typically offer greater stiffness, forces, and lower inertia [5], [6]. However, they are also more susceptible to limited workspaces, singularities, and more complex control and designs. Multiple commercial haptic devices were developed that fall into these two categories. Haption [7] and Sensable Technologies, now known as Geomagic [8], both produce a line of serial kinesthetic haptic interfaces. Geomagic actually produced one of the most widely used haptic devices, the Phantom Premium [9] which has been the focus of numerous studies quantifying its performance [10], [11], [12]. As for

parallel devices, Quanser [13], Force Dimension [14], and Novint [15] all produced widely used commercial parallel mechanisms. These mechanisms have also been the focus of their own studies involving the quantification of their performance in addition to conveying their designs [16], [17], [18]. However, when these commercial devices do not meet certain criteria or when it was desired to implement new designs, researchers even developed their own haptic interfaces such as in [19], [20], [21], and [22]. The number of haptic devices in existence today is overwhelming and multiple publications have taken steps to survey the current haptic interfaces to more easily compare the various devices [5], [23], [24]. A few publications have even tabulated the various mechanism structures of popular haptic devices, which includes serial, parallel, and even hybrid designs [6], [25].

All of these previously presented designs share a common characteristic in terms of kinesthetic haptic devices in that they all are considered to be of the ground-based impedance class. There are two basic classes which are used to describe kinesthetic devices, impedance and admittance [4], [5]. An impedance device senses the position of the operator and then applies a force to the operator corresponding to the response in the simulated or remote environment. In contrast an admittance device is just the opposite, it senses the force applied by the operator and then restricts the position of the operator based upon the response in the simulated or remote environment. The class of the device is significant because it has a substantial impact on the device's design. For example, an admittance class device is inherently nonbackdrivable and has velocity-source actuators vs an impedance class device which is inherently backdrivable and has force-source actuators [24], [26]. Each design has its strengths and weaknesses, for example impedance devices are better at replicating soft touch sensations whereas admittance devices are better at replicating hard touch sensations [5]. However, due to a variety of reasons, admittance devices are not as common, yet commercially available admittance devices do exist such as the HapticMaster [27]. The HapticMaster and all of the previously presented devices are considered to be ground-based devices. Both impedance and admittance class devices can either be considered grounded or ungrounded. Grounded simply refers to the forces felt by the operator are with respect to the physical ground such as the floor where as ungrounded refers to the devices being body-based and applying forces at the points of attachment [5], [23], [26].

Seeing as the intention is to develop a grounded, open-loop force controlled actuator, admittance class and ungrounded devices are not considered. Thus what is to follow is the driving principles behind grounded impedance class devices. Each principle presents a unique contribution in terms of high fidelity open-loop force control with particular emphasis on haptic feedback.

2.1.1 Backdrivability

In order to even implement open-loop force control, the actuator must be backdrivable [6]. If no forces are being reflected, the operator must experience little or ideally no resistance when driving the device and it must be independent of direction and position [5], [26]. This principle goes in hand with reducing the friction and inertia of the design as increased

friction and inertia reduce the ability to backdrive the design. The need for backdrivability substantially impacts the transmission implemented as some designs are inherently nonbackdrivable.

2.1.2 Backlash

Backlash can be detrimental to high fidelity force replication. The lost motion can prevent the continuous or instantaneous application of force to the operator [4]. Furthermore it can create significant issues including instability when implementing a closed-loop system due to its nonlinearity and discontinuity. As a result the design must account for backlash and reduce it or complete remove it all together.

2.1.3 Bandwidth

The controller must exhibit a large bandwidth in order to convey a multitude of force frequencies [4], [5]. By having a large bandwidth the controller will be capable of providing an immersive experience to the operator and allow for more intuitive control. In order to increase the bandwidth, multiple design principles must be considered. In this case, increasing the stiffness and actuation forces and decreasing the inertia, mass, and parasitic forces aid in increasing the bandwidth of the design.

2.1.4 Friction

Similar to backlash, friction which includes static, dry, damping, and the like can detract from the fidelity of the replicated forces [4], [5], [6], [26]. It can create significant issues including instability when implementing a closed-loop system and can diminish the magnitude and sensitivity of the forces reflected to the operator. It is for all practical purposes impossible to eliminate friction from the design, however precautions should be taken to reduce it as much as possible and compensate for what remains.

2.1.5 Inertia and Mass

To the operator the haptic controller should appear physically transparent, as in it should not impede the operator unless a force is desired to be imposed. One way to accomplish transparency is to reduce the inertia of the controller as much as possible [5], [6], [26]. Seeing as inertia is the resistance of a physical object to change in motion it makes intuitive sense to attempt to design the controller with little inertia. Inertia is also a property of and is directly proportional to mass. Thus the inertia can be reduced by reducing the effective mass where ideally the device would be massless [28], [29]. Reduced inertia and mass has the added benefit of increasing the bandwidth of the system and requiring smaller actuation forces and torques to achieve the same acceleration. As a result smaller actuators can be used to achieve the same force reflection capabilities.

2.1.6 Isotropy

Isotropy refers to the properties of the device being uniform throughout its workspace. This is specifically applicable to the properties of mass, inertia, resolution, stiffness, and friction that can vary as a function of position, especially for more complicated higher DoF designs. Undesired torque ripple, torque cogging, and hysteresis also fall into this category [4]. Having properties that vary as a function of position not only increases the complexity of the control but it also negatively affects the fidelity of the force feedback. Thus it is typically desired to strive for isotropy and design the device so that the variation in the properties throughout the workspace is reduced [9], [26], [30].

2.1.7 Stiffness

It is desirable to have a high stiffness controller in order to reflect as large of a range of forces as possible to the operator where ideally the device would be infinitely rigid [4], [6], [26], [28]. However this is for all practical purposes not possible so the stiffness of the device must be increased without significantly sacrificing other design principles. In doing so the bandwidth of the controller can also be increased, leading to a greater number of frequencies that the controller can replicate. Thus the stiffness is significant because it directly impacts how fast the controller can respond to demanded forces.

2.1.8 Range

Range refers to the range of forces that the controller can reflect in addition to the range of motion that the controller can achieve. It is desirable to be able to reflect relatively large and small forces in a large workspace, independent of the location within the workspace [4], [5], [6]. In doing so the operator is provided a sufficient space in which to control as well as the ability to replicate a large range of forces that would be seen in the physical and virtual environment. By providing a large workspace and large range of forces the controller can provide a more immersive experience and ultimately more intuitive control.

2.1.9 Resolution

The capability to resolve small forces and positions is essential to replicating forces sufficiently and realistically [4], [5]. Although this is a discrete system, the finer the resolution the more continuous the output forces will appear. High position resolution enables the ability to resolve very fine motions from the operator and high force resolution enables the ability to apply very fine changes in the force output. This is essential as the force output is computed based upon the position reading thus a high resolution in both factors increases the stability and fidelity of the system. This is especially significant when rendering forces, as the position resolution not only has spatial impacts but also controls the maximum stiffness that can be rendered from the device [26], [31].

2.2 Haptic Impedance-Class Transmissions

Few transmissions exist that satisfy the desired criteria imposed by the impedance-class devices. The most predominant are direct drives, cable drives, or more recently friction drives [4], [26]. Direct drives are, as their name implies, when the motor directly drives the joint and no gearing element is used at all. These drives require high power motors and thus are not very practical nor common. On the other hand, friction drives act as typical gearing but instead of gear teeth they utilize friction resulting from the normal force at the point of contact [32]. Friction drives however have limited force transmission capability which restricts their use. But easily the most common transmission used in impedance-class haptic devices is the cable drive. The cable drive is also the type of transmission utilized in the actuator design presented in this thesis and is thus the topic for the remainder of this literature review.

Cable transmissions, in comparison to typical gear transmissions, are relatively low inertia, mass, and torque ripple while also displaying relatively high stiffness, efficiency, and zero backlash [4], [26], [33], [34]. They do not require lubrication and the only maintenance required is pre-tensioning the cable assembly. Due to these attributes, cable transmissions are readily found in precision instruments outside haptics as well such as the designs found in [35], [36], [37], and [38].

Cable drives can take various configurations where they are typically considered open or closed circuit [39]. However, despite their configuration, most drives specifically implement what is referred to as a capstan drive. Its title originates from the fact that the transmission relies on the capstan equation to operate, and more specifically frictional forces. In capstan drives the cable is wrapped around an input pulley or drum sufficiently to prevent slip which is then used to induce tensions in the cable that in turn drives an output pulley or drum. The designs found in [9], [17], and many others implement this drive.

Although capstans drives have numerous advantages, depending on the design implementation, they can be susceptible to inaccuracies that can detract from its effectiveness and cause variability in its output torque [40]. Thus careful and precise consideration must be undertaken when designing these drives. For example, a sufficiently flexible cable must be implemented as its bending rigidity can reduce the efficiency of the drive [41], [42], [43], [44]. The cable must also be axially stiff to reduce the compliance in the design. Thus the axial stiffness of the cable is an especially important factor in the performance of the actuator and thus its approximation is a common area of research [45], [46]. No matter what level of precision is taken, however, the cable can and readily does slip resulting in transmission error [47] which at times needs to be accounted for via calibration [48]. Due to these issues, the basis of the drive, the capstan equation, is readily modified to provide a better approximation of the dynamics of the system [49], [50].

2.3 Summary

Despite the numerous publications on haptic impedance-class devices, very few provide tools for the design of their corresponding actuators. Most if not all focus more broadly on the device as a whole. Although this is quite practical the issue with this is that impedance-class devices rely on an “ideal” force-source actuator. An actuator that meets the previously described characteristics is no easy task. Although it can be accomplished as evident from the numerous designs in existence, few consider or at least present the true impacts of the design choices made at the actuator level. Thus what is to follow is the presentation of the conceived haptic controller which then leads into the design of the actuator implemented in this device.

Chapter 3

Haptic Controller

The developed haptic controller was designed with the intention of it being used as a universal teleoperation interface to a mobile robotic platform. This haptic controller takes the form of a six DoF input device (three DoF translation, three DoF rotation) with three DoF force feedback (three DoF translation) to the operator. The intention of the force feedback being the enabling factor for more intuitive control. The conceived design for the haptic controller can be seen in Figure 3.1 and in the CAD model of Figure 3.2 below. What is to follow in this section is an overview of the importance of this particular design configuration, its corresponding kinematics and dynamics, and more importantly how its workspace and force feedback relate to its actuation system.

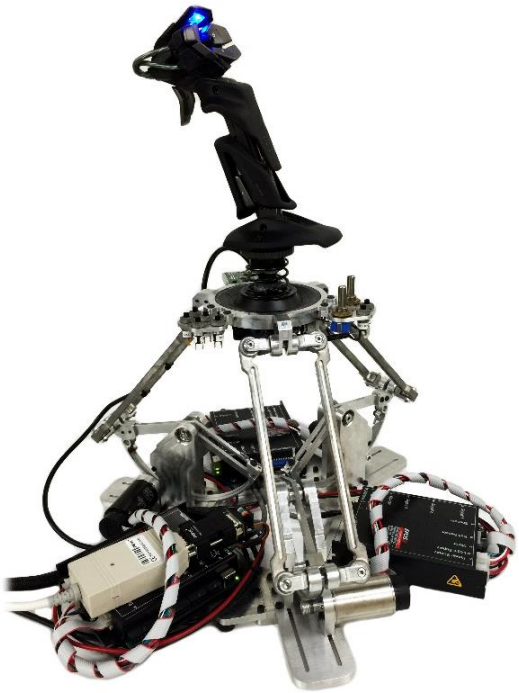

Figure 3.1: Isometric view of the conceived haptic controller.

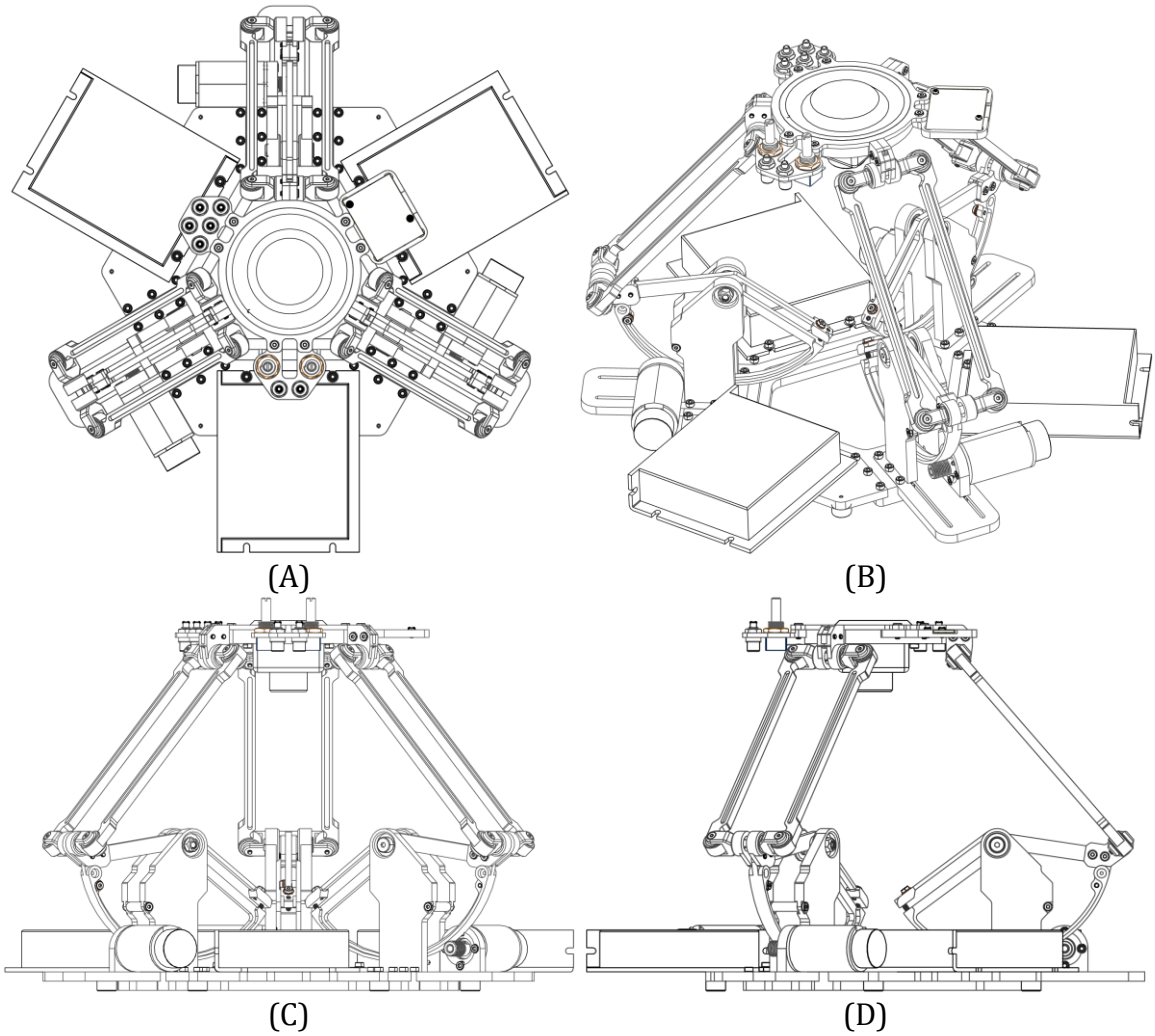

Figure 3.2: Top (A), isometric (B), front (C), and right (D) views of the haptic controller model without the joystick interface.

3.1 Delta Configuration

A parallel kinematic structure is implemented in the form of a delta robot as a result of the numerous intrinsic properties of the design that align with the desired properties of the impedance-class haptic interface. A simplified delta robot can be seen in Figure 3.3 where each revolute joint is represented by a cylinder aligned to the axis of the corresponding joint.

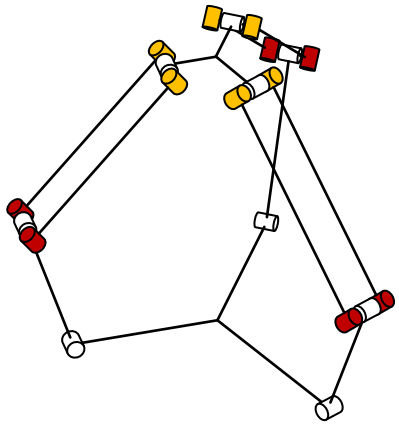

Figure 3.3: Simplified parallel kinematic structure of the delta configuration.

The delta parallel structure is ideal for haptic control as a direct result of its ability to produce a wide range of dynamic behaviors. This is evident in the numerous successful haptic devices based on the delta configuration. To note the most significant and applicable properties, of all the revolute joints in the design only the first revolute joint at the base of each chain needs to be actuated. Locating the motors at the base of the mechanism significantly reduces the mass and inertia of the device without the use of complicated transmission devices. Furthermore, having the actuators and linkages in parallel not only increases the effective stiffness of the device but also increases the reflected forces that can be seen from the device. These advantages alone result in greater force feedback range, bandwidth, and fidelity enabling a much more dynamic and ideal haptic device. A significant disadvantage of typical parallel structures, however, is that they tend to have a smaller workspace in comparison to their serial counterparts. Yet the delta parallel structure exhibits a relatively large workspace, as seen in section 3.2, and even still workspace limitations can typically be circumvented in software.

3.1.1 Kinematics

In order to relate the position, velocity, and acceleration of the end effector in Cartesian space to the position, velocity, and acceleration of the actuators in joint space, the kinematics of the delta were formulated and are presented in Appendix A. The kinematics are invaluable to not only the control but to the analysis and design of the haptic controller. More importantly, these equations were used to determine the desired kinematic performance criteria for the actuator which includes the position range and resolution.

3.1.2 Dynamics

In order to reflect force feedback to the user, the force at the end effector in Cartesian space needs to be mapped to the torques of the actuators in joint space. Thus the dynamics of the delta were formulated and are presented in Appendix B. The dynamics, similar to the kinematics, are invaluable to not only the control of the haptic controller but to the analysis and design of the mechanism as well. Furthermore, these equations were used to determine

the desired dynamic performance criteria for the actuator which includes the torque range and resolution.

3.2 Workspace

The workspace of the haptic controller is significant because it defines the volume in which the user operates as well as the required range of motion of the actuators. However, a significant disadvantage of parallel kinematic structures as opposed to serial kinematic structures is that they typically have a limited workspace. The workspace is also inversely proportional to the device stiffness, mass, inertia, force reflection and resolution, and position accuracy and resolution. As a result, the workspace was taken into cautious consideration in the design of the device. There are numerous approaches to the design of delta based devices. Most formulate the issue into an optimization problem. In this case a more direct approach is applied and the dimensions are designed to compete with other existing delta devices. The modularity of the device accounts for any non-optimality by allowing for device dimensions to be easily changed if even necessary. Furthermore, although a large workspace is beneficial it is not necessary as there are numerous ways to circumvent workspace limitations in software.

In terms of the delta configuration, only five dimensions define the workspace of the haptic controller, d_1, d_2, d_3, d_4, and θ, as defined in kinematics section of Appendix A and as shown in Table 3.1 below. The most significant factors in designing the workspace were ensuring that the workspace is free of singularities as well as collisions. Singularities occur when the device loses one or more degrees of freedom in Cartesian space. This is typically common at the workspace boundary. If a singular position exists, then the Jacobian matrix will be noninvertible at that position. Thus a relatively easy way to ensure that the workspace is singularity free is to ensure that the Jacobian matrix is invertible throughout the workspace. The invertibility of the Jacobian can be checked easily by determining whether its determinant is equal to zero, if it is then a singularity has been reached. In this case the workspace is completely absent of singularities. Collisions, on the other hand, take into account the physical mechanical design and thus must be ensured in the CAD model of the haptic device. In this case, the haptic controller is designed so that it is incapable of colliding with itself unless the user approaches the boundary of the workspace in which case a hard stop is reached. The resulting workspace possessing these attributes can be seen in the following figures showing the isometric, front, right, and top views respectively as well as the workspace's properties as tabulated in Table 3.1.

Table 3.1: Haptic controller dimensions and workspace properties

Parameter	Value	Unit
Dimensions		
d_1	0.080	m
d_2	0.080	m
d_3	0.160	m
d_4	0.055	m
θ	(-36.0 *to* 84.0) 120.0	deg
Workspace		
X-Range	(-0.130 *to* 0.130) 0.260	m
Y-Range	(-0.127 *to* 0.139) 0.266	m
Z-Range	(0.0 *to* 0.169) 0.169	m
Volume	4.190e-3	m^3

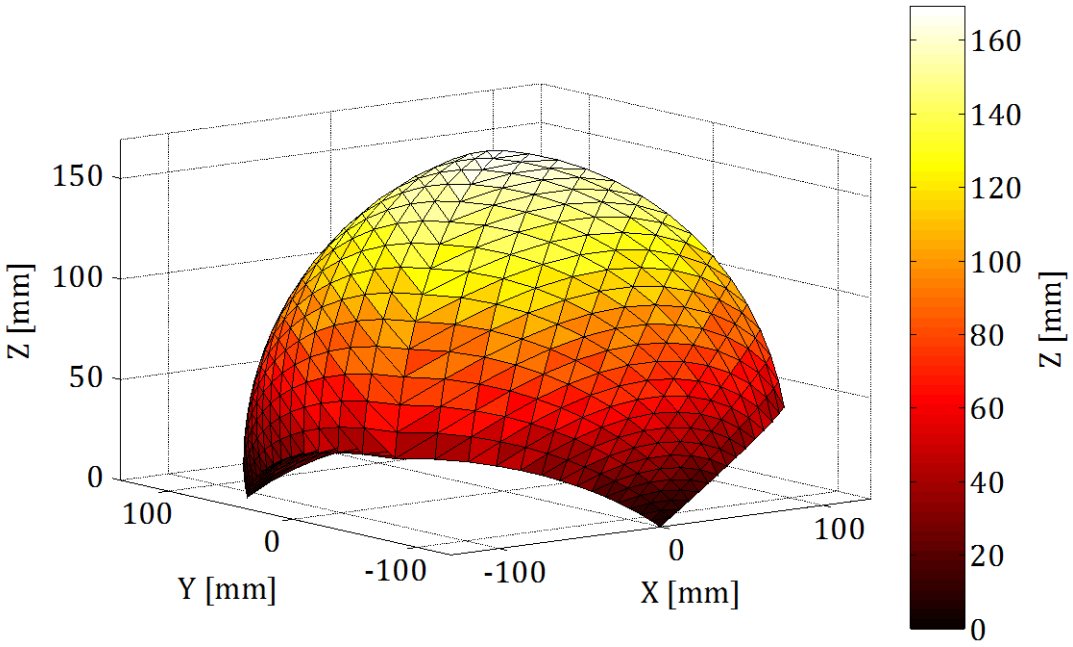

Figure 3.4: Isometric view of the haptic controller workspace.

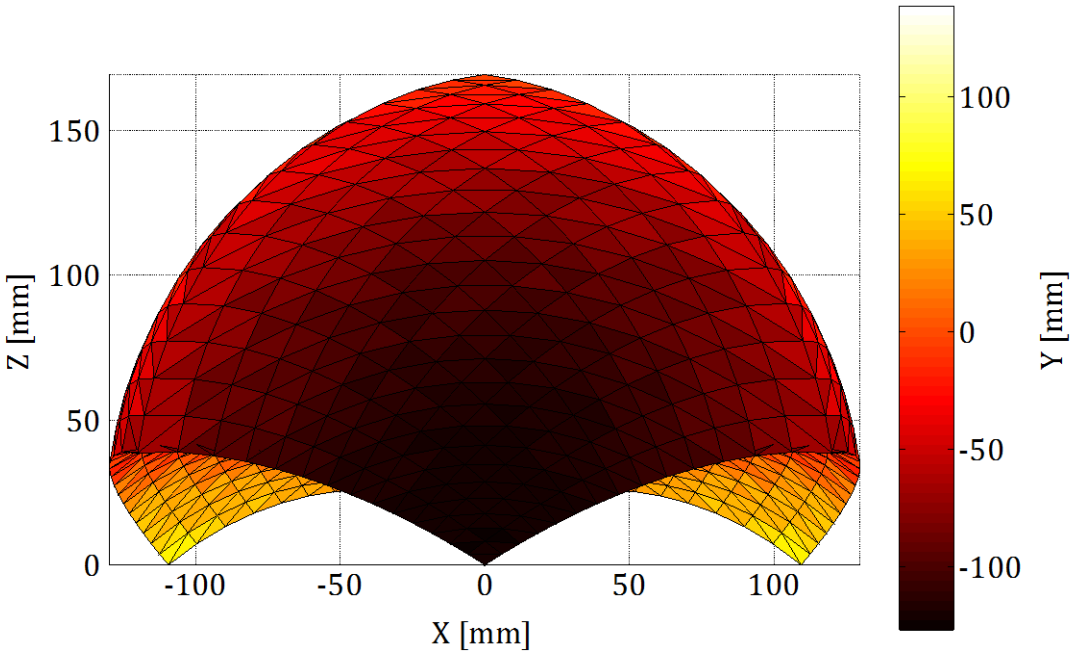

Figure 3.5: Front (XZ plane) orthogonal view of the haptic controller workspace.

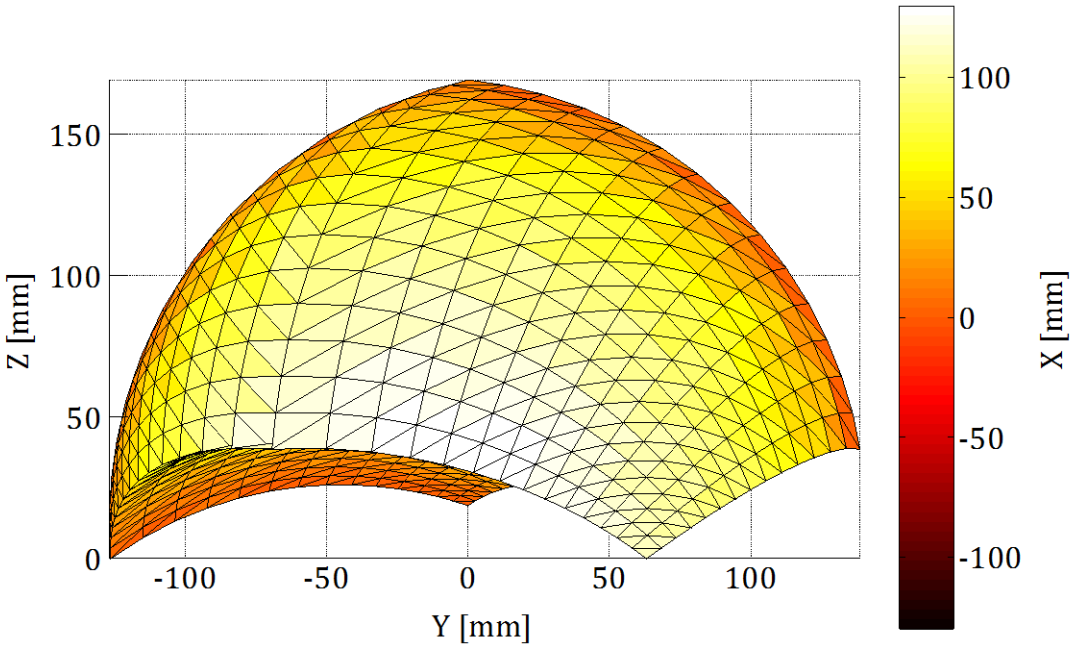

Figure 3.6: Right (YZ plane) orthogonal view of the haptic controller workspace.

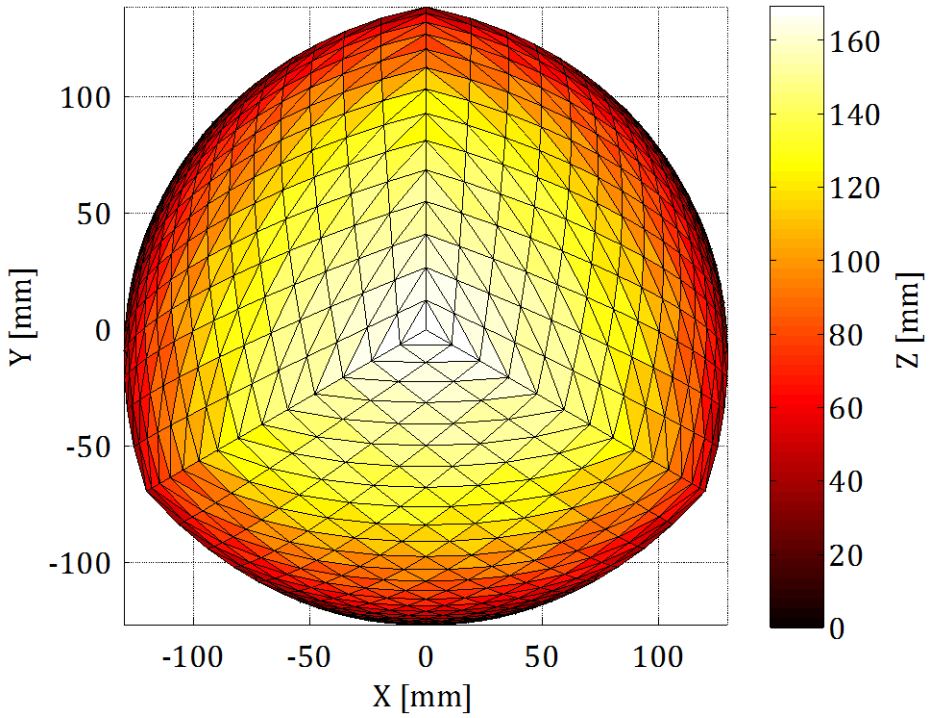

Figure 3.7: Top (XY plane) orthogonal view of the haptic controller workspace.

3.3 Force Feedback

Similar to the formulation of the controller's workspace, the force feedback of the controller was designed to compete with other existing haptic devices. However, the formulation of the controller's force feedback was not as direct. Although it is desired for the controller's properties to be isotropic throughout its workspace it is not possible with the delta configuration. As a result, numerous properties of the controller vary as a function of its position, and the performance of the force feedback is one of them. To determine the required torques from the actuators to achieve the desired force feedback properties throughout the workspace, a 1 mm three dimensional grid interior to the workspace of the haptic controller was generated and the force feedback performance was computed at each point. The resulting minimum, maximum, and average force feedback properties are tabulated in Table 3.2. These properties represent the maximum force that can be continuously applied by the actuators in each dimension without overheating the motors. Depending upon the position in the workspace, the max continuous force feedback will fall in the range from the tabulated minimum to the tabulated maximum with a value likely near the tabulated average. In utilizing this method, the actuators could be designed to ensure that the desired force feedback properties were available throughout the entire workspace of the haptic controller.

Table 3.2: Haptic controller force feedback properties

Parameter	Min	Max	Avg.	Unit
X-Force	9.33	47.62	17.25	N
Y-Force	9.68	47.30	18.69	N
Z-Force	15.64	159.65	25.76	N

3.3.1 Actuation

Using the kinematics and dynamics of the delta configuration, an actuation system capable of supporting the positions and forces resulting from the desired workspace and force feedback was conceived. The actuation system consists of three identical rotary actuators oriented 120 degrees apart at a radius of 80 mm (d_1) to the axis of rotation of the actuator as shown in Figure 3.8. These actuators work concurrently to not only produce the three orthogonal translational forces at the output of the device but also to quantify the position and velocity of the operator to be used in its control. What is to follow in Chapter 4 is the detailed analysis, design, modeling, and experimental validation of these actuators and their impact on the force fidelity of the haptic controller.

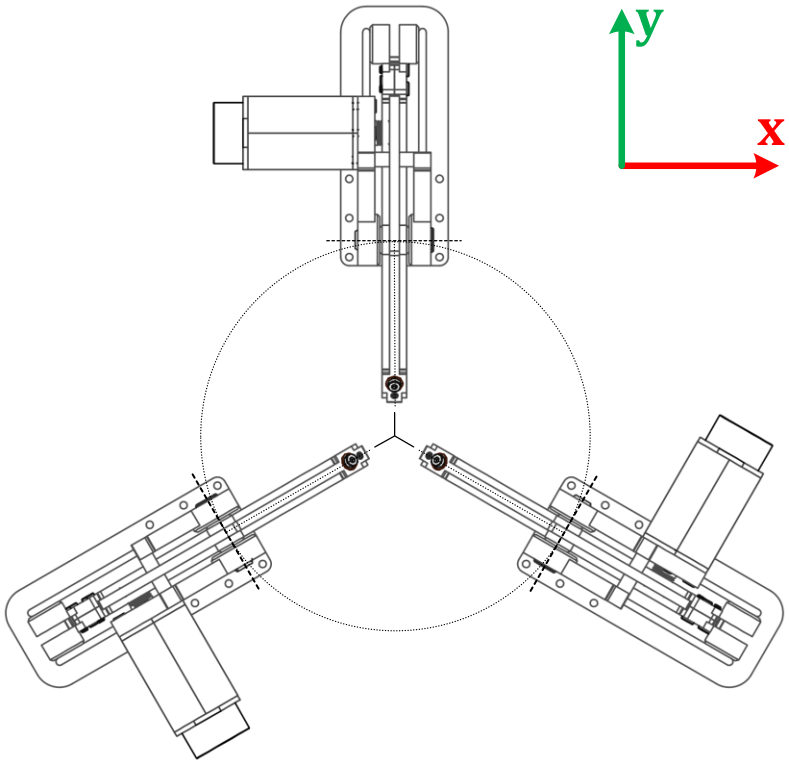

Figure 3.8: Top view of the haptic controller's actuation system.

Chapter 4

Actuator Analysis and Design

The key to high fidelity open-loop force control in any haptic controller is largely dependent on the actuator. This section focuses on the analysis and design of the actuator utilized in the delta haptic controller. Below is a figure of the conceived actuator with its major components labeled in addition to a corresponding table presenting its performance characteristics. The following sections will touch upon the design and analysis of these components with the goal of conveying the importance of each and how they relate to high fidelity open-loop force control.

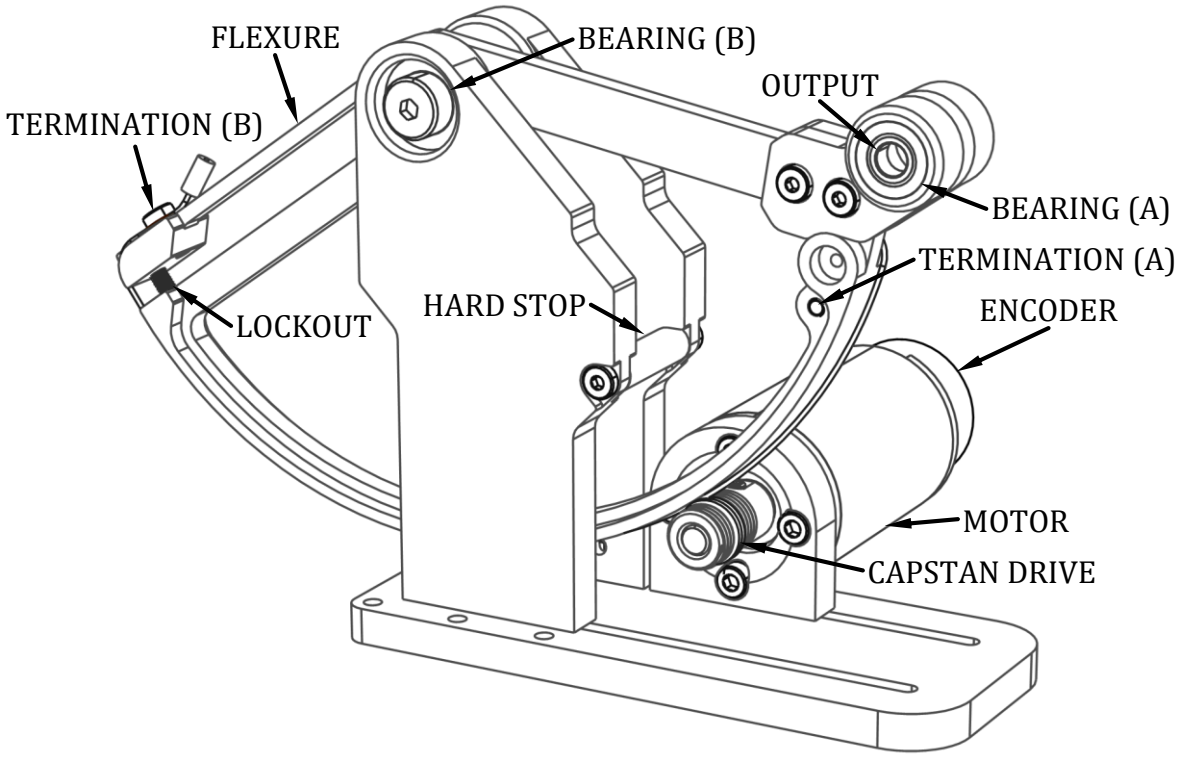

Figure 4.1: Isometric view of the actuator with major components labeled.

Table 4.1: Actuator performance characteristics

Parameter	Value	Unit
Inertia	6.53e-04	$kg \cdot m^2$
Perceived mass	0.102	kg
Continuous torque	1.045	Nm
Peak torque (9.5 N preload)	1.359	Nm
Torque resolution	3.84e-04	Nm
Angular range	120.0	deg
Angular resolution	21.5	arcsec
Bandwidth	300	Hz
Communication rate (1 node)	2000	Hz
Communication rate (3 nodes)	666	Hz

4.1 Motor

The key to high fidelity force control begins at the motor which in this case is an electronically commutated (EC) brushless motor. Brushless motors, as opposed to typical brushed direct current (DC) motors, have their windings on the stator and their permanent magnets on the rotor, similar to the arrangement of synchronous or stepper motors. As a result, the windings of brushless motors have to be electronically commutated. The commutation is performed according to the rotor position, which is measured using Hall sensors, where each phase is applied a voltage sequentially to actuate the rotor. Despite the need for more sophisticated electronic commutation systems, brushless motors can mimmick the linear behavior of a typical brushed DC motor and thus have the same speed-torque profile which makes control relatively easy. An additional advantage is that they are not limited by a mechanically commutated brush system and thus exhibit a longer life and can obtain higher speeds and bandwidths with lower friction.

For this application, the specific motor of choice is the Maxon EC-4pole 30. What makes the EC-4pole 30 the motor of choice is that it has been specifically optimized for power density. It exhibits one of the highest torque densities with one of the lowest mechanical time constants in comparison to both brushed and brushless motors. This is achieved by the 4-pole design, winding arrangement, high quality magnetic materials, and overall electromechanical design. Typically brushless motors of this configuration have one pair of permanent magnetic poles on the rotor. The EC-4pole contains two pole pairs which results in a greater total magnetic flux in the air gap and thus increases the torque produced by the motor. This is in addition to the use of high power neodymium (NeFeB) magnets which allows the rotor mass and inertia to be decreased, despite the increase in the number of pole pairs. Maxon's knitted winding arrangement is especially significant because it makes use of a slotless design which not only increases the motor torque but also exhibits no torque cogging. As a result, depending on the commutation method, the output torque can be a smooth constant profile independent of the rotor position, which is ideal for force control.

Maxon offers four different versions of this motor for a 30 mm diameter and a power rating of 100 W. Each version contains a different winding made of different diameter wire, which in turn changes the electrical characteristics of the motor. As the wire diameter is decreased the number of turns are correspondingly increased. This has the result of increasing the winding resistance as well as the inductance, requiring a larger nominal voltage and a lower nominal current. It also has the added effect of increasing the torque constant and decreasing the speed constant. In terms of robotic applications it is ideal to have a high voltage power bus in order to decrease the required current and thus enable the use of smaller cables. As a result, the motor with the largest terminal resistance was chosen and its relevant properties are presented in the following table.

Table 4.2: Maxon EC-4pole 30 motor specifications

Parameter		Value	Unit
Nominal operating points			
No load speed, n_0		17800	rpm
No load current, I_0		290	mA
Nominal speed		16800	rpm
Nominal torque (max. continuous)		69.4	mNm
Nominal current (max. continuous)		2.96	A
Stall torque		1470	mNm
Electrical data			
Terminal resistance phase to phase, R		0.836	Ω
Terminal inductance phase to phase, L		0.118	mH
Torque constant, k_t		25.5	mNm / A
Speed constant, k_n		374	rpm / V
Speed / torque gradient		12.2	rpm / mNm
Number of pole pairs		2	-
Number of phases		3	-
Mechanical data			
Mechanical time constant, τ_m		2.35	ms
Rotor inertia, J		18.3	gcm²
Axial play at axial load	< 8.0 N	0	mm
	> 8.0 N	0.14	mm
Radial play		preloaded	-
Max. axial load (dynamic)		5.5	N
Max. radial loading, 5 mm from flange		25	N

It is worth noting that tolerances can significantly influence the values reported in Table 4.2. The winding resistance can fluctuate by as much as ±7% as a result of varying wire diameter due to the production and winding process. The magnetic properties can fluctuate by as much as ±8%, which are directly proportional to the torque constant. Even the no-load current has a tolerance of ±50%. As a result, the tolerances need to be taken into consideration when actuating the motors and accounted for if they prove to be a significant issue.

4.1.1 Dynamics

The electrical and mechanical equations of motion for a DC motor are as follows

$$V = L\frac{dI}{dt} + RI + k_b\dot{\theta} \tag{4.1}$$

$$J\ddot{\theta} = k_t I - b\dot{\theta} \tag{4.2}$$

where V is the voltage applied to the motor, I is the motor's winding current, k_b or $1/k_n$ is the motor's back electro magnetic force (EMF) constant, $\dot{\theta}$ is the rotor's angular velocity, b is the motor's viscious friction constant, and the remaining variables are as defined in Table 4.2. These equations completely describe the dynamics of the motor and are used in formulating the following equations of this section.

A significant parameter which Maxon fails to provide for the motor is the viscious friction constant. This variable is necessary in deriving the system model of the actuator. In order to determine an equivalent value for the constant, a first order system was conceived from equations 4.1 and 4.2 as shown in equation 4.3.

$$J\ddot{\theta} = \frac{k_t}{R}V - \left(\frac{k_t k_b}{R} + b\right)\dot{\theta} \tag{4.3}$$

This equation was derived by assuming that the impedance due to the inductance is negligible and that the electrical time constant is substantially faster then the mechanical time constant. From equation 4.3. the inclusive equation for the mechanical time constant of a DC motor which accounts for viscious friction was derived as shown below.

$$\tau_m = J\left(\frac{k_t k_b}{R} + b\right)^{-1} = \frac{J}{b_e} \tag{4.4}$$

From equation 4.4 it can be concluded that the equivalent viscious damping coefficient can be approximated as

$$b_e = \frac{k_t k_b}{R} + b \approx \frac{k_t k_b}{R} \tag{4.5}$$

where the viscious friction constant, b, of the rotor is considered negligible per Maxon. As for the chosen Maxon motor, its equivalent viscious friction constant evaluates to 7.778e-04 Nm·s/rad. As previously stated, this constant is necessary for the purposes of modeling the system as well as for compensating for frictional forces in the control of the actuator.

In addition to the mechanical time constant provided by Maxon, the electrical time constant can prove to be useful in comparing the transient behavior of the different parts of the system. In regards to electrical equation of motion in 4.1, it can be assumed that the transient behavior of the current is significantly faster then the transient behavior of the rotor. As a result the rotors velocity can be assumed to remain constant when considering the current,

which results in a similar first order differential equation with an electrical time constant given by equation 4.6.

$$\tau_e = \frac{L}{R} \tag{4.6}$$

Using equation 4.6, the electrical time constant of the Maxon motor can be approximated as 0.141 ms. In this case the electrical time constant is 16.6 times faster then the mechanical time constant provided by Maxon, which agrees with our assumption in terms of the speed of the transient behaviors.

Seeing as the motor is typically operated in a quasi-static configuration, only a few of the previously presented parameters are directly applicable in terms of the force control. As with a typical dc motor, there exists a directly proportional, electromechanical constant relating the motor current to the produced torque known as the torque constant, k_t. The equation relating the two is given below

$$T_u = k_t I \tag{4.7}$$

where I is the motor current and T_u is the produced torque. However, as with any mechanical system there exists friction. And the magnitude of the motor's friction can be drawn from the no-load current given in Table 4.2. The no-load current takes into consideration both a constant friction torque and a speed dependent friction torque at the no-load speed. However, for practical purposes the speed dependent component is significantly smaller than the constant component and thus can be neglected. Incorporating this current, I_0, into the previously presented equation results in equation 4.8.

$$T_u = k_t(I \pm I_0) \tag{4.8}$$

This relation is valuable because it allows the use of the motor's current to perform open-loop force control on the actuator where accounting for the no-load current gives a better approximation of the true torque.

Although the motor is typically operated in a quasi-static configuration, the rotor inertia comes into play in terms of the effective mass experienced by the user at the end effector. A low rotor inertia is thus desired, especially considering that the motor's inertia gets amplified by the square of the transmission ratio. In this case the motor's relatively low rotor inertia is only 18.3 gcm^2 which is made possible by the powerful but compact neodymium magnets on the rotor.

4.2 Encoder

The operators input to the haptic controller is quantified via the actuator's position and velocity. In order to measure the angular position and velocity of the actuator, a Maxon digital magneto-resistance (MR) encoder is implemented on the motor's rotor to directly

measure its output. The relevant specifications of the encoder are detailed in Table 4.3 at the end of this section. This encoder relies specifically on the MR principle which includes a multipole magnetic disc mounted on the motor shaft that produces a sinusoidal voltage in the MR sensor. An integrated circuit makes the magnetic encoder appear as a incremental quadrature encoder via interpolation. The circuit also includes an electronic line driver which improves signal quality by creating steeper signal edges as well as producing complementary signals for each of the three channels to help eliminate interference on the signal lines. This is relevant to this application because the signal lines are run in parallel to the motor's power lines and thus are exposed to a significant amount of electromagnetic noise. Furthermore, this is especially important in terms of incremental encoders because electromagnetic interference can result in signal losses and thus accumulated errors in the position value. The three signal channels in this case consist of two phase shifted square wave signals A and B as well as an index channel, I, which is used for referencing or counting revolutions.

In order for the actuator to be able to resolve very small changes in angular position and velocity the encoder must have a high number of pulses per revolution (increments). Furthermore, an encoder with a higher pulse count can also provide a smoother, more ripple-free commutation of the motor. As a result, the encoder with highest number of pulses per revolution that was capatible with the chosen motor was selected, which in this case is 1000 pulses per revolution. In terms of the number of pulses some positioning systems, including the maxon EPOS2 controllers to be discussed, have the ability to count the rising and falling edges of the two square wave signals A and B. This results in four times the resolution for quadrature encoders, in this case 4000 quadcounts per revolution, where for every single pulse cycle there exists four quadcounts. Typically the drawback of a higher number of pulses per revolution is reduced maximum operating speed. However, the actuator is operated at relatively low speeds in addition to not being designed for continuous rotation, thus this is not an issue.

Table 4.3: Maxon MR encoder specifications

Parameter	Value	Unit
Type		
Pulses per revolution	1000	-
Number of channels	3	-
Max. operating frequency	200	kHz
Max. speed	12000	rpm
Technical data		
Phase shift (1 pulse cycle = 360°)	90 ± 45	deg
Index pulse width (1 pulse cycle = 360°)	90 ± 45	deg
Moment of inertia of code wheel	≤ 0.7	gcm^2

4.3 Motor Controller

In order to commutate and drive the chosen brushless motor, a digital motor controller with an integrated power stage was required. In this case a Maxon motor controller, the EPOS2 50/5, networked on a CANopen system was used. An image of this motor controller can be seen in the following figure.

Figure 4.2: Isometric view of the Maxon EPOS2 50/5 motor controller, from website www.maxonmotorusa.com, used under fair use, 2015.

This motor controller is ideal for open-loop force control because it can not only take advantage of the full performance of the brushless motor chosen but it exhibits numerous properties that align with the desired characteristics of the haptic controller. The properties of the EPOS2 50/5 that are most relevant are presented in the following table.

Table 4.4: Maxon EPOS2 50/5 motor controller specifications

Parameter	Value	Unit
Ratings		
Nominal power supply voltage, V_{cc}	11…50	VDC
Max. output voltage	0.9 · V_{cc}	VDC
Max. output current, I_{max} (<1 sec)	10	A
Continuous output current, I_{cont}	5	A
Switching frequency	50	kHz
Max. speed @ sinusoidal commutation (1 pole pair)	25000	rpm
Max. speed @ block commutation (1 pole pair)	100000	rpm
Inputs		
Digital	11	-
Analog (12-bit, ±10 V)	2	-
CAN ID (DIP switch)	1…127	-
Outputs		
Digital	5	-
Analog (20 kHz, 12-bit, 0…10 V)	1	-

In order to take full advantage of the motor's torque output, the chosen motor controller must be able to meet or exceed the max continuous current of the driven motor. The EPOS2 can not only output 5 amps continuously, approximately 2 amps greater than the max continuous current of the motor, but it can also supply impulses as high as 10 amps for less than a second. As a result, the max continuous operating range of the motor and the desired force output range can be achieved. Furthermore, if the max continuous current of the motor were to be increased, by for example active cooling, the motor controller has the potential to drive the motor at even greater currents and thus provide even greater feedback forces to the operator.

Considering a brushless motor is to be controlled, a motor controller capable of electronically commutating brushless EC motors with digital Hall sensors and an encoder was required. Brushless commutation typically involves taking feedback of the rotor position, via the Hall sensors and encoder, and determining a set of winding currents for that position in order to produce a desired torque. The EPOS2 can not only drive the brushless motors using basic block commutation but it can also drive the motors using sinusoidal current commutation by space vector control. Using this commutation method is the most advanced in terms of commutating brushless motors. When implemented with a high encoder resolution, this commutation method produces the smoothest output torque with minimal torque ripple and noise in the motor.

It is also worth noting that the motor controller has numerous general purpose inputs and outputs (I/O). Although not currently used, the I/O allows the ability to expand upon the capabilities of the haptic controller by integrating additional sensing and features into the device.

4.3.1 Current Controller

Seeing as the motors will be operated in force control, the current controller implemented on the motor controller is especially important. The controller must be able to measure currents in milliAmps, command currents in milliAmps, and update at a sufficiently high frequency. The current control loop implemented on the EPOS2 runs at a frequency of 10 kHz, far greater then the bandwidth of both the main motion controller (~600 Hz) as well as the dynamics of the system. It is ideal to have the lower level controllers running as quickly as possible, at least two times faster then the fastest frequency in the system, in order to reduce the total latency, increase the stability of the system in terms of control, and take advantage of the full bandwidth of the actuator.

With almost any haptic deivce, it is ideal to have high force resolution at the output, which translates to high current resolution at the input. The EPOS2 current controller can measure and command current values to 1 mA resolution which equates to about 25.5 μNm at the output of the motor. This current resolution enables very fine control of the force output and although it is discrete the step size is so small that the output appears continuous to the operator.

To regulate the current, the EPOS2 uses an integrated proportional-integral (PI) controller. A block diagram of the implemented controller architecture in the frequency domain is shown below.

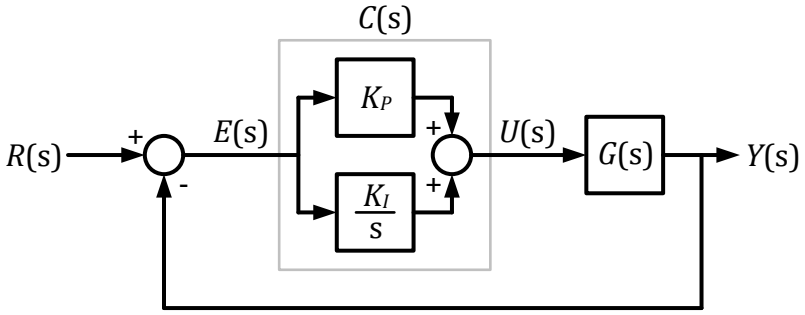

Figure 4.3: Block diagram of the current regulator implemented on the motor controller.

In terms of the diagram, $R(\mathrm{s})$ is the desired input current, $Y(\mathrm{s})$ is the actual output current, $E(\mathrm{s})$ is the error between the input and output current, $C(\mathrm{s})$ is the current proportional-integral (PI) controller, and $U(\mathrm{s})$ is the voltage input to the plant representing the motor electrical, $G(\mathrm{s})$. The PI controller, $C(\mathrm{s})$, is described in more detail as provided by equation 4.9

$$C(\mathrm{s}) = \frac{U(\mathrm{s})}{E(\mathrm{s})} = K_P + \frac{K_I}{\mathrm{s}} \tag{4.9}$$

where K_P is the proportional constant and K_I is the integral constant. It is these constants that are responsible for tuning the current controller to the desired response. As for the plant, it can be described in more detail by equation 4.10.

$$G(\mathrm{s}) = \frac{Y(\mathrm{s})}{U(\mathrm{s})} = \frac{\frac{1}{L}}{\mathrm{s}+\frac{R}{L}} \tag{4.10}$$

The plant transfer function, $G(\mathrm{s})$, was conceived by taking the Laplace transform of equation 4.1 and manipulating variables to have it appear as shown in equation 4.10. It was assumed that the transient behavior of the current was significantly faster then the transient behavior of the rotor. As a result the rotors velocity was again assumed to remain constant when considering the current and neglected from the equation.

With the equations for the controller and plant defined, the equation for the entire feedback loop was formulated as given by equation 4.11.

$$\frac{Y(\mathrm{s})}{R(\mathrm{s})} = \frac{C(\mathrm{s})G(\mathrm{s})}{1+C(\mathrm{s})G(\mathrm{s})} = \frac{\frac{K_P}{L}\mathrm{s}+\frac{K_I}{L}}{\mathrm{s}^2+\left(\frac{K_P+R}{L}\right)\mathrm{s}+\frac{K_I}{L}} \tag{4.11}$$

This continous, frequency domain model of the current control system was then used to model the response of the motor to various demanded inputs using different PI gains in MATLAB. Prior to testing, the model was first discretized using the zero-order hold method

at the sample rate of 10 kHz. The zero-order hold method was chosen since the control inputs to the system are piecewise constant over the sampling period. For these staircase inputs, this method provides an equivalent result between the continuous and discrete time systems in the time domain.

The gains of the discrete current controller were then chosen to reduce current oscillations and provide a low time constant for the transient of the response. Thus the gains of the controller were chosen to produce a response similar to a critically damped system. In doing so the system approaches the desired value very quickly without inducing oscillation. This was accomplished by first determining gains that produced the desired response in the model and then testing those gains on the motor using a software package provided by Maxon known as EPOS Studio. EPOS studio was used because it allowed the use of a data recorder executed in the current regulator at the 10 kHz sample rate. Unfortunately the recorder was limited to a ring buffer size of 512 words, but it was sufficient to test the current controller and determine a set of desirable gains. Once a set of parameters were identified the verification of the resulting control system was tested with a unit step response. The control parameters were incrementally tuned to get the desired response and after each iteration the controller was tested. The step response and its corresponding performance measures resulting from the final gains is presented in the following figure and table respectively.

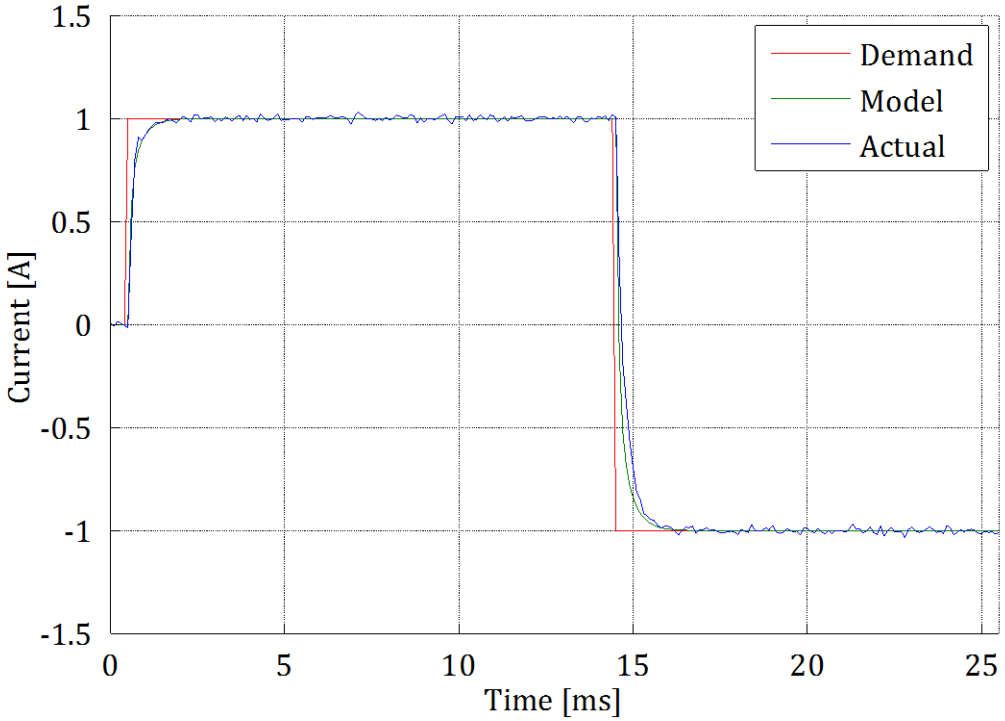

Figure 4.4: Step response of the modeled and actual current controller to a demanded input current.

Table 4.5: Current controller step response performance measures

Parameter	Value	Unit
Sample rate	10000	Hz
Sample period	0.1	ms
Rise time (10% to 90%)	4	sample periods
Time constant (63.2%)	2	sample periods
Settling time (2%)	10	sample periods
Overshoot	0	%
Undershoot	0	%
Steady-state error	0.0	mA

Based upon the performance measures, the response of the current controller exhibits no overshoot or oscillation as desired. It also rises quite rapidly with a rise time of 4 sample periods and even settles within 2% of the final value in 10 sample periods. With a response this fast the current will settle to its final value before the next current command is demanded. Furthermore, thanks to the I gain, the controller has zero steady-state error, which is necessary for the actual current to converge with the demanded value.

To further quantify the closed-loop current controller, the frequency response of the current controller model was generated and is shown plotted in Figure 4.5. As evident from the plot, the system has a bandwidth of approximately 1003 Hz and introduces relatively little phase shift to the system. Furthermore, it does not resonate and the gain remains reasonably constant in the passband, both of which are desired characteristics for a current controller.

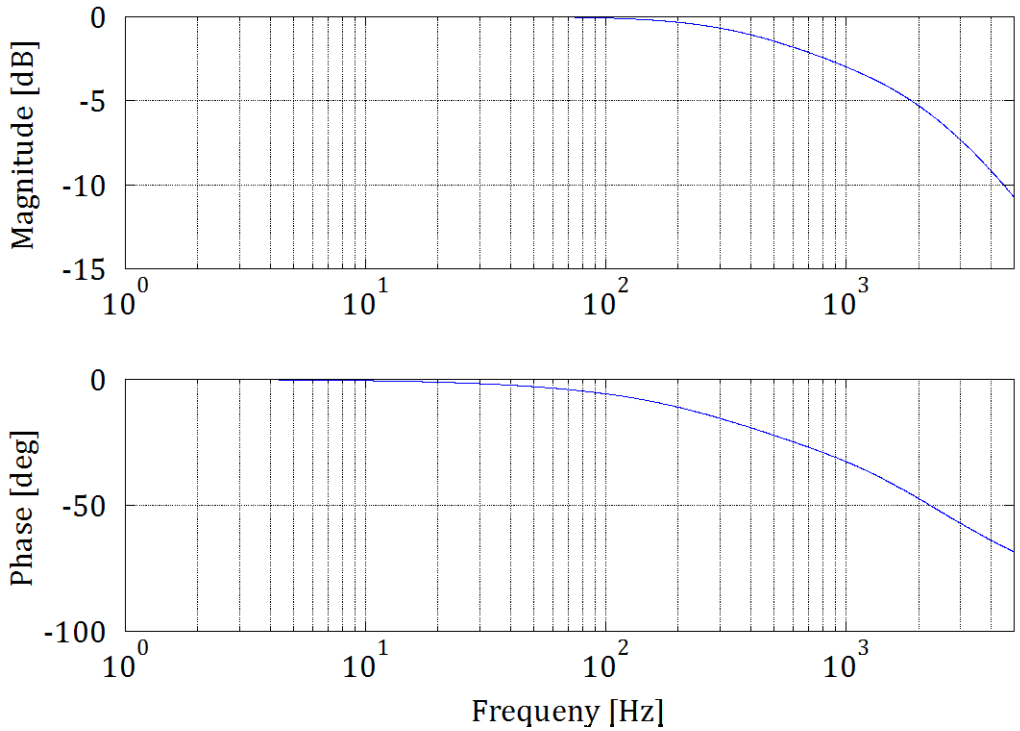

Figure 4.5: Bode plot of the current controller's frequency response.

It is worth noting that as a result of the tolerances in the motor properties, gains should be chosen for each actuator individually. Furthermore, when implementing multiple actuators concurrently the responses need to be relatively equivalent thus the gains should be chosen to produce a unit step response with comparable time constants for each motor. With that being said, the proportional and integral gains resulting from the motor tested in Figure 4.4 and Figure 4.5 is shown in the following table.

Table 4.6: Current controller proportional-integral gains

Parameter	Value	Unit
EPOS2		
P-Gain	300	-
I-Gain	130	-
SI		
P-Gain	1.172	Ω
I-Gain	5.078e+03	Ω/s

The table includes two sets of gains because the gains used in the model cannot be used directly in the EPOS2 motor controller. The gains must be converted from SI units to values that are recognized by the EPOS and this is accomplished using the following conversions.

$$K_{P\ldots EPOS2} = 2^8 \cdot K_{P\ldots SI} \tag{4.12}$$

$$K_{I\ldots EPOS2} = \frac{2^8}{10^4} \cdot K_{I\ldots SI} \tag{4.13}$$

It is evident from the step response of Figure 4.4 that there is an observable amount of noise in the system. This is not a surprise as current transducers are typically susceptible to significant amounts of noise. The noise in the transducer is also a reason why the implemented controller is only a PI controller as opposed to a proportional-integral-derivative (PID) controller as the derivative term is sensitive to measurement noise. However, a derivative term is also not necessary due to the inherent damping effect produced by the inductance of the motor. Nevertheless, the motor controller can resolve to 1 mA, but it is not necessarily accurate to 1 mA due to this noise. To better understand the magnitude of the noise in the system, the input was commanded to zero and the output of the current sensor was recorded resulting in the data populating Figure 4.6 and the metrics populating Table 4.7.

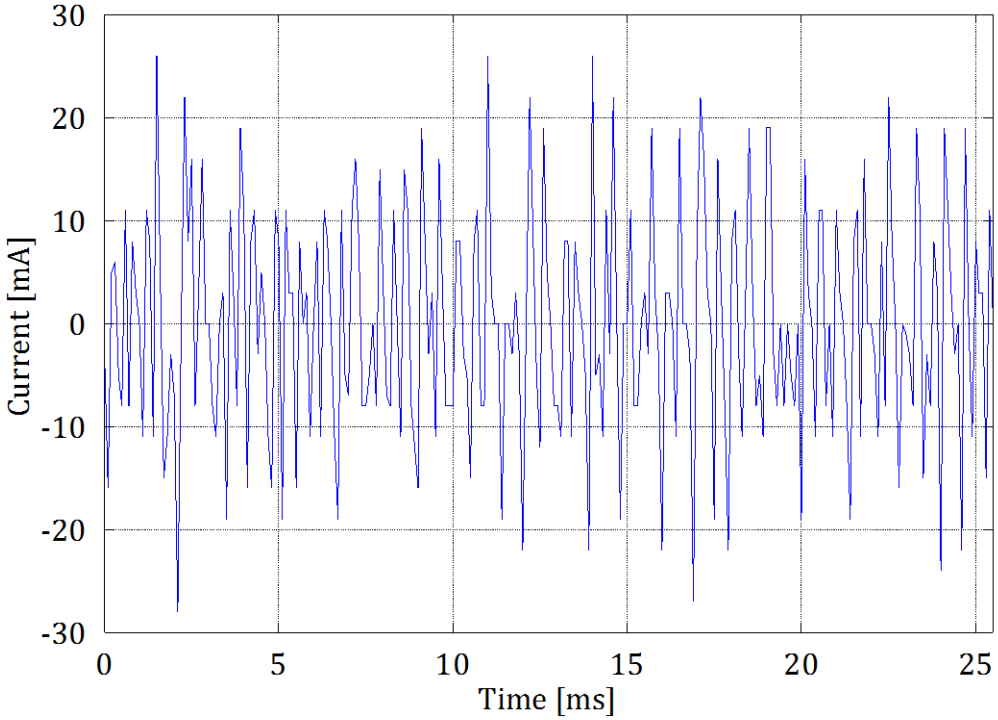

Figure 4.6: Plot of the measured noise from the current controller sensor.

Table 4.7: Current controller noise metrics

Parameter	Value	Unit
Max	26	mA
Min	-28	mA
Range	54	mA
Mean	0.00391	mA
Variance	120.271	mA^2
Standard deviation	10.967	mA
Average power	119.801	mA^2

From Table 4.7 it can be observed that the noise in the current signal is approximately zero mean and remains within the range of ±30 mA (<±1 mNm). This amount of noise is not much of a cause for concern as it is relatively small in magnitude and fluctuates at an exceptionally high frequency, far greater than the mechanical bandwidth of the actuator. As a result, the actuator will simply act as a low pass filter and attentuate the noise to a negligible magnitude. However, the properties of the noise if desired can be used as an input disturbance to the system model and thus are included.

4.3.2 Communication

The EPOS2 motor controllers are intended to be implemented in a single communication network in which they communicate to a single master computer. The communication occurs via a controller area network (CAN) bus using the CiA CANopen specification DSP-

402 version 2.0 (Device Profile Drives and Motion Control) communication protocol. Although the EPOS2 motor controllers have the option of being controlled via USB 2.0 or RS232 serial interfaces, a CAN bus interface was implemented for its high reliability, consistency, and popularity in the embedded control systems community. The CAN bus in this instance is high-speed and thus is capable of 1 Mbit/s data rates, which is the fastest data rate currently achievable by a CAN bus. The motor controllers represent a single electronic control unit or node within the CAN network. The nodes are identified by a unique node ID (CAN ID) that is defined using a dual in-line package (DIP) switch on each of the controllers. In this case, the node IDs of the motor controllers are defined according to the serial chains ($i = 1,2,3$) in which they actuate in the haptic controller, as previously presented in Chapter 3. The nodes communicate to the master computer via a single channel PCAN-USB adapter, which translates all CAN messages to USB 1.1 and vice versa. The overall structure of the embedded system can be seen in the following diagram.

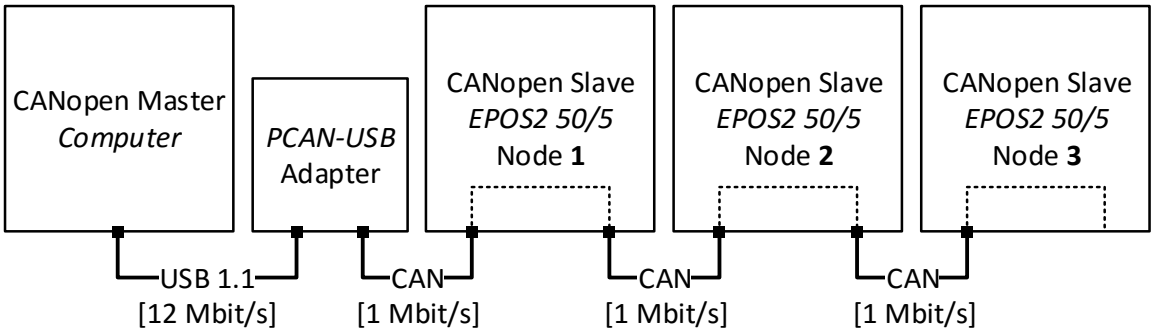

Figure 4.7: Communication diagram of the actuation system.

4.4 Transmission Element

In order to achieve the desired force output to be conveyed to the operator, the actuator cannot be directly driven by a mechanically grounded motor. A transmission element must be used to amplify the force output. In doing so it must also coincide with the desired performance specifications of the haptic controller and not impede the force fidelity experienced by the operator. What is to follow is the detailed analysis and design of such a drive as used in the sector rotary actuator.

4.4.1 Analysis

Below is a figure displaying a simplified capstan drive with major dimensions labeled. In this case the cable is wrapped once around the threaded input pulley and its ends are terminated on the output pulley not pictured.

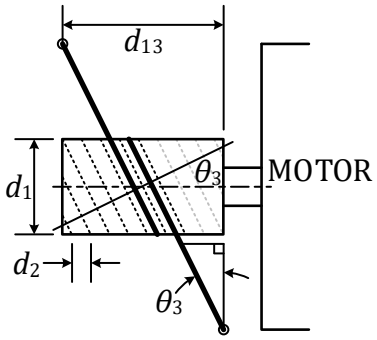

Figure 4.8: Simplified diagram of the capstan drive input pulley.

In Figure 4.8, the major diameter of the input pulley is defined as d_1, the lead of the thread is defined as d_2, the minimum width of the output pulley is defined as d_{13}, and the helix angle of the thread is defined as θ_3. The cross section of a single V-thread groove found on the input pulley is given in Figure 4.9. The geometry of the thread is significant in that it not only determines the effective diameter to be used in defining the gear ratio but also the frictional forces experienced by the cable. All the dimensions shown in the figure are symmetric about the vertical centerline, which intersects the axis of the screw thread in the plane of the figure.

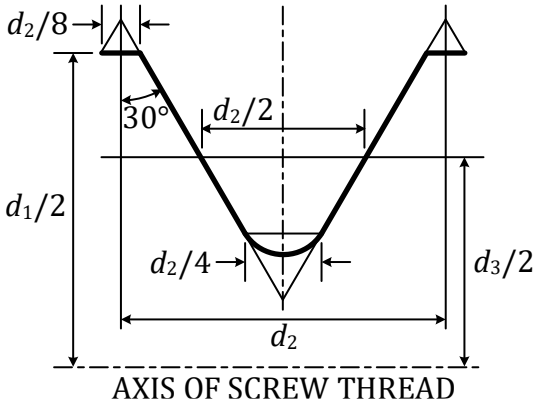

Figure 4.9: Cross-section of a single V-thread groove found on the input pulley.

With regard to Figure 4.9, the variables d_1 and d_2 are as defined in the previous figure. The variable d_3 represents the mean or pitch diameter of the thread. This variable, d_3, can be formulated in terms of the pitch and major diameter as provided by the following equation.

$$d_3 = d_1 - \frac{3}{8\tan(30°)} d_2 \tag{4.14}$$

Using the lead, d_2, and pitch diameter, d_3, of the thread, the mean helix angle of the thread, θ_1, can be calculated as shown below.

$$\theta_1 = \tan^{-1}\left(\frac{d_2}{\pi d_3}\right) \tag{4.15}$$

As seen from Figure 4.8 and the corresponding equations, the lead is especially significant because it not only directly effects the helix angle of the thread but it also limits how narrow

the pulley can physically be. This is a result of the fact that the cable must travel one lead length for every revolution of the input pulley. Thus it is desired to reduce the lead as much as possible. It is also worth noting that capstan pulleys are not always threaded. However, threaded pulleys are advantageous because they not only keep the cable tracked but they also substantially increase the frictional force, which will be discussed shortly.

In order to simplify the analysis of the input pulley geometry, the section view previously presented in Figure 4.9 is rotated about the vertical centerline by the thread helix angle, θ_1, into the plane normal to the cable. The result is given by the following free-body diagram of Figure 4.10 where F_n is the force induced by the cable, F_r are the reaction forces, d_4 is the diameter of the cable, and d_5 is the effective input diameter. It is worth noting that the axis of the screw thread is no longer in the plane of the figure and that the deflection of the cable at the points of contact is not considered.

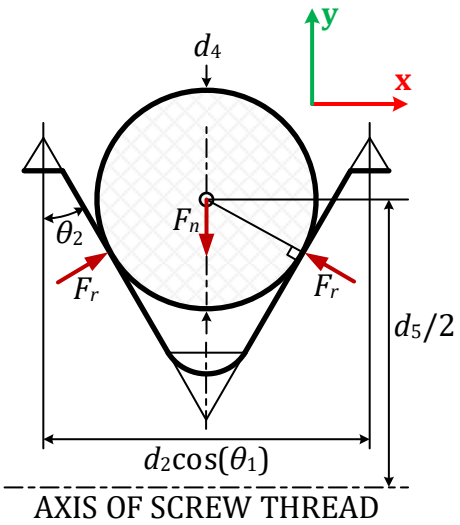

Figure 4.10: Cross-section of a single V-thread groove normal to the cable.

The slope of the groove, θ_2, now becomes a function of the helix angle and is given by the following equation.

$$\theta_2 = \tan^{-1}(\cos(\theta_1)\tan(30°)) \tag{4.16}$$

Making use of the two previous figures and simple trigonometry the effective diameter of the input pulley is given by the following equation.

$$d_5 = d_1 - \frac{7}{8\tan(30°)}d_2 + \frac{1}{\sin(\theta_2)}d_4 \tag{4.17}$$

In order to get a better approximation of the true effective diameter of the capstan input pulley the helix angle formed at the point of contact between the cable and the thread should be used in place of the mean helix angle calculated in equation 4.14. This also has the added benefit of determining the true slope of the groove, θ_2, and thus the actual reaction forces seen by the cable. This can be accomplished by first completing the calculations as presented.

Once the initial approximation of d_5 and θ_2 are known then the following equation can be used in place of d_3 in equation 4.15 and the calculations are then repeated until the solution converges.

$$d_3^* = \sqrt{(d_5 - d_4 \sin(\theta_2))^2 + (d_4 \cos(\theta_2) \sin(\theta_1))^2} \tag{4.18}$$

In this case this is not necessary as the approximation is well within the dimensional tolerances of the components used in the capstan drive. However, this may be useful for other designs of larger scale where not accounting for the true helix angle at the point of contact could be significant.

Once the effective diameter of the input pulley is known the actual helix angle formed by the center of the cable can be calculated by the following equation.

$$\theta_3 = \tan^{-1}\left(\frac{d_2}{\pi d_5}\right) \tag{4.19}$$

This equation proves resourceful when the helix formed by the cable is to be defined. It is necessary to define the helix in order to determine the forces vectors imposed by the cable, which is to be discussed shortly.

Before determining the equation for the helix, the frictional forces seen by the cable are pursued. First a force balance is performed in the y-direction with respect to Figure 4.10 resulting in the following equation.

$$\sum F_y = -F_n + 2 \sin(\theta_2) F_r = 0 \tag{4.20}$$

Solving for F_n as a function of F_r results in equation 4.21

$$F_n = 2 \sin(\theta_2)\, F_r \tag{4.21}$$

and the corresponding friction force is defined as in equation 4.22

$$F_f = 2\mu F_r = \frac{\mu}{\sin(\theta_2)} F_n \tag{4.22}$$

where μ is the coefficient of static friction. As seen in equation 4.22, the use of a V-thread effectively increases the friction coefficient by a factor of $1/\sin(\theta_2)$, which for a 60° V-groove of 1 mm lead is approximately 2. This is significant because the cable cannot be allowed to slip on the input pulley. Thus it is desired to have as large of a friction force as possible along the line of contact of the cable and the input pulley.

The friction coefficient specifically comes into play in the most critical equation used in the design known as the standard capstan equation given by equation 4.23

$$F_h = F_l e^{\mu\theta} \tag{4.23}$$

where F_l and F_h is the tension in the cable on the low load side and high load side, respectively, and θ is an arbitrary angle of contact in radians. It can be observed from equation 4.23 that in addition to the friction coefficient, the angle of contact is also especially significant. This results from the fact that increasing the angle of contact also exponentially increases the load capability of the drive.

The force components from the capstan equation of 4.23 are also depicted in the free-body diagram of Figure 4.11 where an input torque, T_u, drives the input pulley, which in turn applies forces to the cable and actuates the output pulley. It is worth noting that the figure is in the plane normal to the axis of rotation and that there are components of the tension forces acting out of the plane due to the helix angle.

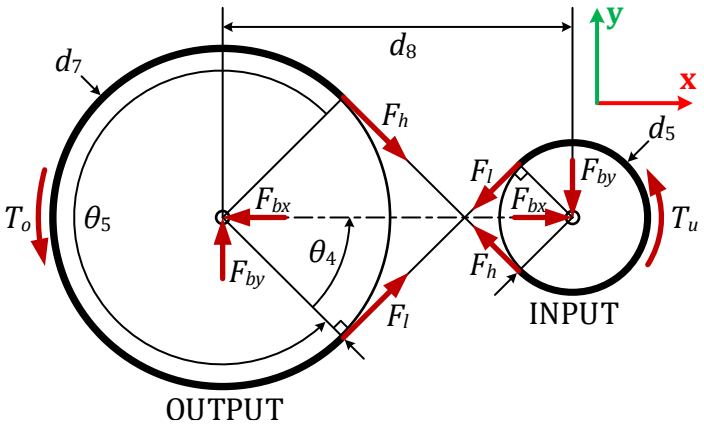

Figure 4.11: Free-body diagram of the input and output pulley.

Using the geometry of the figure and recognizing the fact that both pulleys have the same angle of contact, θ_5, with the exception of multiple turns, the following equations and corresponding constraints can be formulated defining the angle of contact for the input pulley.

$$\theta_4 = \cos^{-1}\left(\frac{d_5+d_7}{2d_8}\right)$$
$$2d_8 \geq d_5 + d_7, 0 \leq \theta_4 < \frac{\pi}{2} \tag{4.24}$$

where d_7 is the effective diameter formed by the cable on the output pulley. Unlike the input pulley, the output pulley is not threaded due to its termination thus the effective diameter is given by equation 4.25

$$d_7 = d_6 + d_4 \tag{4.25}$$

where the actual diameter of the output pulley is given by d_6. With these equations defined the angle of contact of the input pulley, θ_5, can then be defined by equation 4.26.

$$\begin{gathered}\theta_5 = 2\pi k_r - 2\theta_4 \\ k_r \geq 1\end{gathered} \tag{4.26}$$

In this case, k_r is the number of revolutions the cable is wrapped around the input pulley and for the equation to be applicable θ_4 must be expressed in radians. From equation 4.24 and 4.26, it can be concluded that having $d_5 + d_7$ approximately equal to $2d_8$ is ideal as it maximizes the contact angle as well as reduces the overall length of the cable. And as previously stated increasing the angle of contact exponentially increases the ability of the drive to hold greater loads and decreases the ability of the cable to slip on the input pulley.

Another factor in determining whether the cable will slip, in addition to the angle of contact, are the tension forces experienced by the cable. The tension forces seen by the cable can be expanded upon as shown below

$$\begin{gathered}F_l = F_p - F_u \\ F_h = F_p + F_u\end{gathered} \tag{4.27}$$

where F_p is the preload force and F_u is the force due to the input torque. A preload is necessary to remove any compliance or slack from the cable and ensure adequate frictional force exists to prevent the cable from slipping on the input pulley. Substituting the expanded values, the angle of contact θ_5 (radians), and accounting for the effective increase in the coefficient of friction into equation 4.23 results in equation 4.28.

$$F_p + F_u = \left(F_p - F_u\right)e^{\frac{\mu}{\sin(\theta_2)}\theta_5} \tag{4.28}$$

In order to incorporate the input torque into equation 4.28 a torque balance was performed about the input pulley using the free-body diagram of Figure 4.11 resulting in equations 4.29 and 4.30.

$$\sum M_z = T_u + \frac{d_5}{2}\cos(\theta_3)\,F_l - \frac{d_5}{2}\cos(\theta_3)\,F_h = 0 \tag{4.29}$$

$$F_u = \frac{1}{d_5\cos(\theta_3)}T_u \tag{4.30}$$

Substituting equation 4.30 into equation 4.28 and solving for the preload force results in equation 4.31.

$$F_p = \frac{-\left(1+e^{\frac{\mu}{\sin(\theta_2)}\theta_5}\right)}{d_5\cos(\theta_3)\left(1-e^{\frac{\mu}{\sin(\theta_2)}\theta_5}\right)}T_u \tag{4.31}$$

Equation 4.31 is especially significant in terms of drive design because it can be used to determine the preload necessary to prevent slipping given an input torque, friction coefficient, and pulley dimensions. It is desired to minimize the preload as much as possible

as it generates friction in the bearings due to the radial load in addition to placing additional stress on the cable and assembly. It is also warranted to minimize the distance between the two pulleys, d_8, as this dimension can result in undesired radial loads as well, in addition to further cable deflection. Thus, equation 4.31 can be used to calculate a cable preload sufficient to prevent slipping, but not in excess to induce additional stresses in the assembly.

In order to determine the forces induced in the input and output pulley by the cable preload and input torque, the equations for a helix were derived according to the coordinate frame defined in Figure 4.11. The z-axis in this case is constrained to the axis of rotation of the input pulley. This results in the following three-dimensional vector defining the helix as a function of an angle in radians at which the cable enters and exits the pulley.

$$\mathbf{h}(\theta) = \left(-\frac{d_5}{2}\cos(\theta), \frac{d_5}{2}\sin(\theta), -\frac{d_2}{2\pi}\theta\right) \quad \theta_4 \leq \theta \leq \theta_4 + \theta_5 \tag{4.32}$$

To determine the tangent to the helix curve, the derivative of the previous equation was derived and is shown in the following equation.

$$\dot{\mathbf{h}}(\theta) = \left(\frac{d_5}{2}\sin(\theta), \frac{d_5}{2}\cos(\theta), -\frac{d_2}{2\pi}\right) \quad \theta_4 \leq \theta \leq \theta_4 + \theta_5 \tag{4.33}$$

From equation 4.33, the unit tangent vector was derived by normalizing the derivative vector $\dot{\mathbf{h}}(\varphi)$ via the 2-norm given below.

$$\left|\dot{\mathbf{h}}(\theta)\right|_{\mathbf{2}} = \frac{\sqrt{d_2^2 + \pi^2 d_5^2}}{2\pi} = \frac{d_5}{2\cos(\theta_3)} = \frac{d_2}{2\pi\sin(\theta_3)} \tag{4.34}$$

Thus the unit tangent vector of the helix is then given by equation 4.35

$$\frac{\dot{\mathbf{h}}(\theta)}{\left|\dot{\mathbf{h}}(\theta)\right|_{\mathbf{2}}} = (\sin(\theta)\cos(\theta_3), \cos(\theta)\cos(\theta_3), -\sin(\theta_3)) \quad \theta_4 \leq \theta \leq \theta_4 + \theta_5 \tag{4.35}$$

which is used to determine the components of the cable forces and the subsequent reaction forces seen by the assembly.

Taking a closer look at the induced forces and recognizing that the radial load for both pulleys are equal and opposite, a force balance was performed on the input pulley as shown below. Here the bearing forces are as defined in Figure 4.11. The reaction force F_{bz} is defined as a force aligned with the axis of rotation of the input pulley and oriented such that it is pointing out of the plane of Figure 4.11.

$$\sum F_x = F_{bx} - \cos(\theta_3)\sin(\theta_4)\,F_l - \cos(\theta_3)\sin(\theta_4)\,F_h = 0 \tag{4.36}$$

$$\sum F_y = -F_{by} - \cos(\theta_3)\cos(\theta_4)F_l + \cos(\theta_3)\cos(\theta_4)F_h = 0 \tag{4.37}$$

$$\sum F_z = F_{bz} + \sin(\theta_3)\,F_l - \sin(\theta_3)F_h = 0 \tag{4.38}$$

With the force balances defined, the variables were expanded into their constituent components and the radial forces were solved for resulting in the following equations

$$F_{bx} = 2\cos(\theta_3)\sin(\theta_4)\,F_p \tag{4.39}$$

$$F_{by} = 2\cos(\theta_3)\cos(\theta_4)F_u = \frac{d_5+d_7}{d_5 d_8}T_u \tag{4.40}$$

$$F_{bz} = 2\sin(\theta_3)F_u = \frac{2\tan(\theta_3)}{d_5}T_u \tag{4.41}$$

where the magnitude of the radial resultant force is given by equation 4.42.

$$F_{br} = \sqrt{(F_{bx})^2 + \left(F_{by}\right)^2} \tag{4.42}$$

The most valuable contribution of these equations is that they help to ensure that the bearings are not overloaded in the motor or output pulley. They also help to ensure that excess forces are not induced due to a poor design. For example, it can be concluded that as $d_5 + d_7$ approaches $2d_8$ that the radial force resulting from the preload drops to zero whereas the radial force from the input torque rises to $2T_u/d_5$. Thus this trade off must be considered when evaluating the design.

Up to this point, all of these equations have been unique to the cable drive. However, in contrast to these equations, the transmitted torque is identical to that of typical gearing. In this case the effective gear ratio of the cable drive is given by equation 4.43

$$k_g = \frac{d_7}{d_5} \tag{4.43}$$

and the corresponding output torque is given by equation 4.44

$$T_o = k_g T_u \tag{4.44}$$

where T_o and T_u are as defined in Figure 4.11. Although this is a simple relation, it is invaluable to the control of the actuator and how accurate the demanded force is to the actual force. As evident from equation 4.43, any discrepancies in the effective input and output diameters of the pulleys can lead to miscalculations in the applied forces. This is partly why such a level of detail was taken in deriving the calculations.

Now that the significant parameters are defined, the last relations to be introduced quantify the lengths of the cable sections required to drive the design. Below are the three equations

defining the arc length of the helix formed about the input pulley, the arc length of the helix formed about the output pulley, and the free cable length joining the two pulleys, respectively. For these equations all the angles are defined in radians and the desired range of motion of the output pulley is defined as θ_6.

$$d_9 = \theta_5 \sqrt{\left(\frac{d_5}{2}\right)^2 + \left(\frac{d_2}{2\pi}\right)^2} \tag{4.45}$$

$$d_{10} = \theta_6 \sqrt{\left(\frac{d_7}{2}\right)^2 + \left(\frac{k_g d_2}{2\pi}\right)^2} \tag{4.46}$$

$$d_{11} = \frac{2d_8 \sin(\theta_4)}{\cos(\theta_3)} \tag{4.47}$$

The minimum cable length necessary to operate in the entire workspace of the cable drive can then determined from the sum of the previously defined dimensions and is given by the following equation. Using equation 4.48, the total cable length can be reduced, thus avoiding introducing additional elasticity into the system due to cable deflection.

$$d_{12} = d_9 + d_{10} + d_{11} \tag{4.48}$$

In order to take full advantage of the design and operate in the entire range of motion defined by θ_6, relations must also exist that specify the minimum width of the pulleys. This includes accounting for the helix angle and ensuring that the pulley widths are large enough for the cable to remain tangent to the helix throughout the workspace. The first relation defines the width of the output pulley, d_{13}, which is given by the following equation

$$d_{13} = \sin(\theta_3) d_{12} \tag{4.49}$$

which can also be written as

$$d_{13} = \frac{\theta_5 + k_g(\theta_6 - 2\theta_4)}{2\pi} d_2 + \frac{2\sin(\theta_4)}{\pi} \frac{d_2 d_8}{d_5} \tag{4.50}$$

where all the angles are defined in radians. The input pulley, on the other hand, requires a smaller minimum width in order to operate in the entire range of motion and is given by the following equation

$$d_{14} = \frac{(\theta_5 + k_g \theta_6)}{2\pi} d_2 \tag{4.51}$$

where all angles are also defined in radians. Using both equation 4.50 and 4.51, the width of the transmission can be designed logically and not over designed so as to avoid introducing excess mass and inertia into the design.

4.4.2 Design

Using the previously presented analysis, geometric and static parameters were chosen and calculated for the capstan drive based upon the requirements of the actuator. All of the parameters are listed in the following table and those explicitly chosen are marked with a bullet point whereas the remaining parameters were either calculated using the equations found in the previous section or are published values.

Table 4.8: Capstan drive design parameters

Parameter	Value	Unit	Description
Lengths			
• d_1	10.0	mm	Input major diameter
• d_2	1.0	mm	Lead of V-thread
d_3	9.350	mm	Pitch diameter of V-thread
• d_4	0.762	mm	Cable diameter
d_5	10.009	mm	Effective input diameter
• d_6	150.0	mm	Output diameter
d_7	150.762	mm	Effective output diameter
• d_8	80.5	mm	Distance between pulley axes
d_9	93.847	mm	Input pulley arc length
d_{10}	157.957	mm	Output pulley arc length
d_{11}	8.587	mm	Free cable length
d_{12}	260.391	mm	Minimum cable length
d_{13}	8.021	mm	Minimum width of output pulley
d_{14}	8.004	mm	Minimum width of input pulley
Angles			
θ_1	1.894	deg	V-thread mean helix angle
θ_2	29.986	deg	Effective slope of V-thread groove
θ_3	1.822	deg	Cable helix angle
θ_4	3.056	deg	Capstan non-contact region
θ_5	1073.888	deg	Capstan angle of contact
• θ_6	120.0	deg	Output pulley range of motion
Forces			
F_u	6.937	N	Input tension
F_p	7.271	N	Minimum preload tension
F_l	0.334	N	Low load tension
F_h	14.209	N	High load tension
F_{bx}	0.775	N	X-Bearing force
F_{by}	13.848	N	Y-Bearing force
F_{bz}	0.441	N	Z-Bearing force
F_{br}	13.869	N	R-Bearing force
Torques			
• T_u	0.0694	Nm	Input torque (max. continuous)
T_o	1.045	Nm	Output torque (max. continuous)

Dimensionless			
• k_r	3	-	Number of cable revolutions
k_g	15.062	-	Effective gear ratio
μ	0.1	-	Coefficient of friction

In order to achieve the desired force output range, an output torque of approximately 1 Nm was necessary. To attain such an output using the Maxon EC-4pole 30 motor, a gear ratio of approximately 15 was required at the max continuous current of the motor. Typically, gear ratios for haptic devices range from 10:1 to 25:1. However, it is desired to use the minimum required gear ratio as additional gearing will nominally only increase the mass, inertia, and friction of the device with little added benefit. To achieve the desired gear ratio the design strategy was to first minimize the input pulley diameter. This has the added benefit of increasing the gear ratio, decreasing the reflected inertia, and decreasing the total cable length. The drawback of making the input pulley smaller is that it increases the forces seen by the cable and requires additional preload to compensate. Thus the diameter was chosen to ensure that the resultant forces were well within the rated strength of the cable and the radial bearing force was well within the max radial loading of the motor and output pulley bearings. Ultimately the input pulley major diameter was determined to be 10 mm based upon the previous criteria, the motor shaft diameter (5 mm), and the minimum bend radius of the cable. And as for the corresponding diameter of the output pulley, a diameter of approximately 150 mm was chosen to achieve the desired gear ratio.

With regard to the V-thread found on the input pulley, the lead chosen must be as small as possible to reduce both the axial length of the pulleys and the helix angle of the thread. However, the lead must be large enough to accommodate a qualified cable capable of supporting the desired loads in addition to having a bend radius of approximately 5 mm. As a result, a lead of 1.0 mm was chosen. A lead of this dimension ensures that a cable of sufficient strength or diameter will seat in the groove of the thread and not contact the outer diameter of the shaft. This is significant because if the cable diameter is too large to seat in the groove then both the equations for the effective diameter and friction forces will be compromised. This design also has the added benefit of being a standard thread for a M10 shaft and thus remains relatively easy to manufacture. The implemented design for the capstan drive on the input pulley is shown in Figure 4.12. The figure includes an overlaid cross-section view so that the seating of the cable in the thread can be more easily observed.

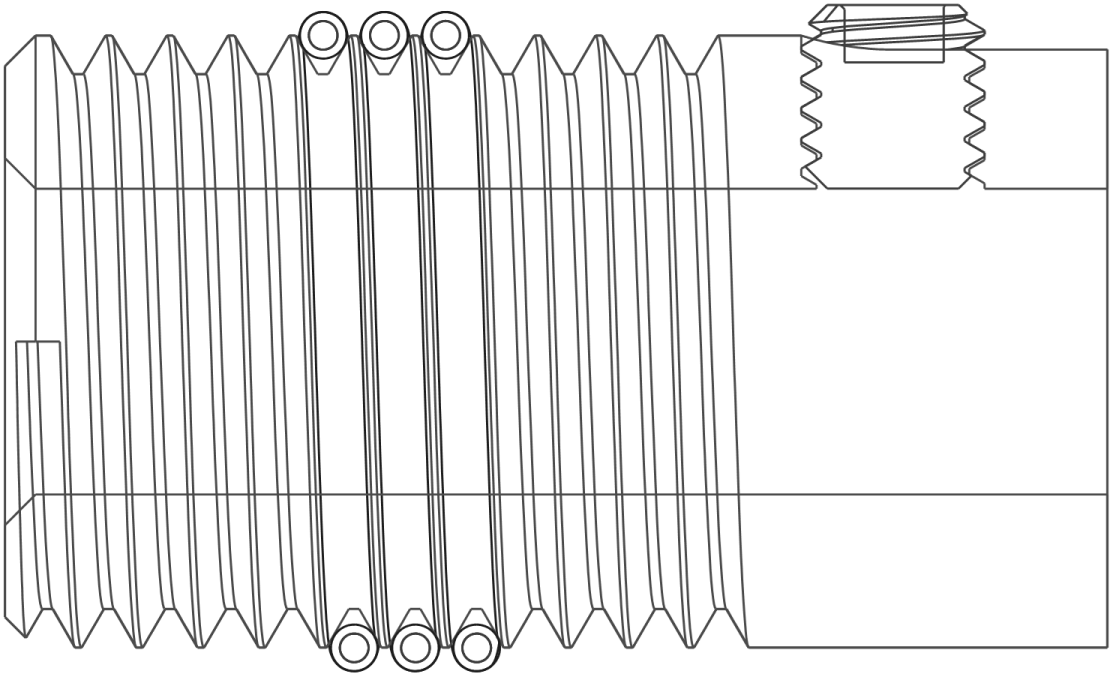

Figure 4.12: Capstan drive input pulley model.

In order for the transmission to be as effective as possible, the selected cable must be both axially stiff yet flexible to bending laterally. As a result, a cable with a large number of wires per strand and a small rope diameter was required. A 302/304 (18-8) stainless steel cable of 7x19 construction class, which refers to the number of strands by the number of wires per strand, was thus chosen. Using a cable this finely-stranded allowed for a tight bend radius without inducing yielding in the outermost fibers. To protect these fine wires from abrasion, a nylon coated cable was also chosen. A nylon coating helps to not only protect the cable and aluminum pulleys from wear but also provides fatigue resist as well. However, one issue that the coating fails to mend is that as the number of wires per strand is increased the stiffness of the cable decreases. As a result, the chosen cable is also low-stretch which refers to the rope being physically stretched during construction to minimize elongation during operation. This is desired in terms of the transmission performance as it increases the stiffness of the cable as well as the bandwidth of the assembly. The remaining detailed specifications for the cable are shown in Table 4.9 and an example of the cross-section of the cable can be seen in Figure 4.13.

Table 4.9: Cable properties

Parameter	Value	Unit
Load capacity	45	N
Breaking strength	270	N
Coated diameter	0.762	mm
Bare diameter	0.610	mm
Strands	7	-
Strand diameter	0.203	mm
Wires per strand	19	-
Wire diameter	0.0406	mm
Wire cross-sectional area	0.00130	mm^2
Total metallic area	0.173	mm^2

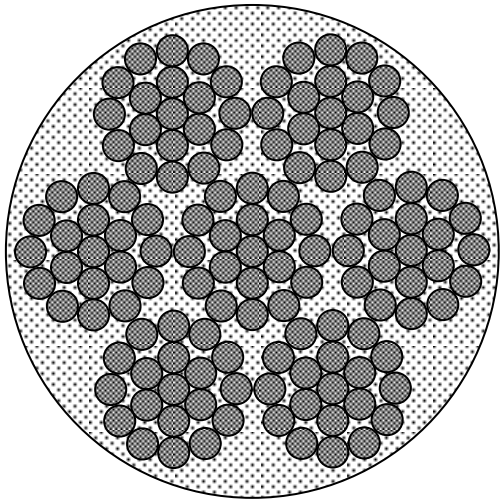

Figure 4.13: Stranded 7x19 construction class cable cross-section.

As seen in Table 4.9 the metallic cross-sectional area of the cable is provided. This parameter is necessary to determine the effective stiffness of the cable. However, this is not a published value and was calculated based upon the geometry of the construction class and the bare rope diameter. As seen in Figure 4.13, to calculate the area of a single wire, the diameter of a single strand was first approximated as one third of the bare diameter of the cable. Then the diameter of a single wire was approximated as one fifth the diameter of a single strand. And thus the area of a single wire can then be calculated and the corresponding total metallic area is simply the area of a single wire multiplied by the number of strands and the number of wires per strand.

The stiffness of the cable is a significant limitation in the bandwidth of the design. To assist in mitigating this compliance, the design minimizes the total length of the cable to reduce the undesired cable stretch. This is partly accomplished by minimizing the distance between the pulley axes. Decreasing this distance also has the added benefit of decreasing the overall size of the design. Thus, a value of 80.5 mm was chosen, just exceeding the minimum value of 80.386 mm. This decision is also reflected in the angle of contact since the contact angle increases as the distance between pulley axes decreases. To further increase the angle of

contact, the cable is wrapped 3 revolutions about the input pulley as seen in Figure 4.12. This number of revolutions was chosen to help compensate for the low friction coefficient of nylon on aluminum as well as to reduce the required preload force. The preload force must be greater than the largest input force in order to ensure positive tension always remains in the entire cable and slipping does not occur. As seen from Table 4.8, the difference between the input tension and minimum preload tension is simply 0.334 N. This is a direct result of the large angle of contact as well as the effective increase in the friction coefficient due to the V-thread.

To further reduce the undesired cable stretch and compliance, the cable was promptly terminated beyond the range of motion of the actuator using copper stop compression sleeves and washers. In this case the range of motion was dictated by the desired workspace of the haptic controller, which resulted in a range of motion of 120° for the actuator. Figure 4.14 shows the actuator at the boundaries of its workspace which is constrained by a single mechanical hard stop. By promptly terminating the cable beyond the boundary of the workspace, the total cable length is decreased reducing the total possible deflection of the cable for a specified loading.

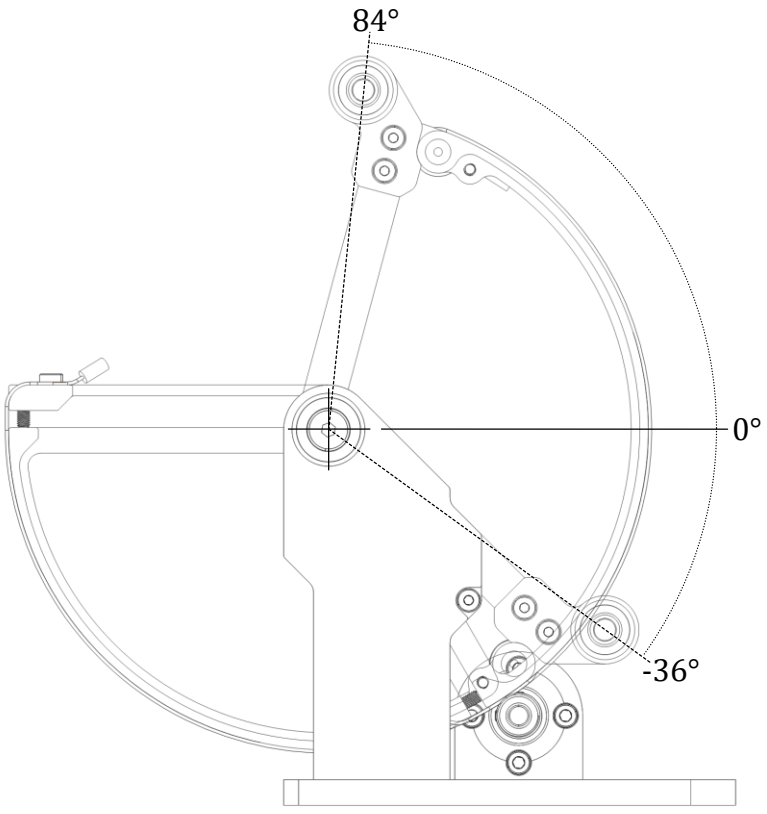

Figure 4.14: Actuator range of motion.

4.5 Preloading Element

Due to the nature of the transmission element chosen, a preloading element must be incorporated in order to tension the cable assembly. Similar to the transmission elements, numerous designs exist for pretensioning cable drives. However, most rely on not knowing the actual preload applied to the cable. A few designs overcome this with the use of spring elements, however they lack the ability to lock out the preload thus introducing compliance into the system. Furthermore, they introduce additional components increasing the complexity of the system as well. Thus it was desired to design a preloading element that could impart a desired preload while also meeting the desired performance specifications sought in the haptic controller. A flexure was concluded to be the preloading element of choice due to the fact that it can be designed for a specific preload while also being able to be physically incorporated into the transmission. This design also has the additional advantage of enabling complete control over the design and form factor where the design is not constrained to commercial off the shelf components.

4.5.1 Analysis

The flexure in this case takes the form of a cantilever beam with a rectangular cross-section as shown in Figure 4.15.

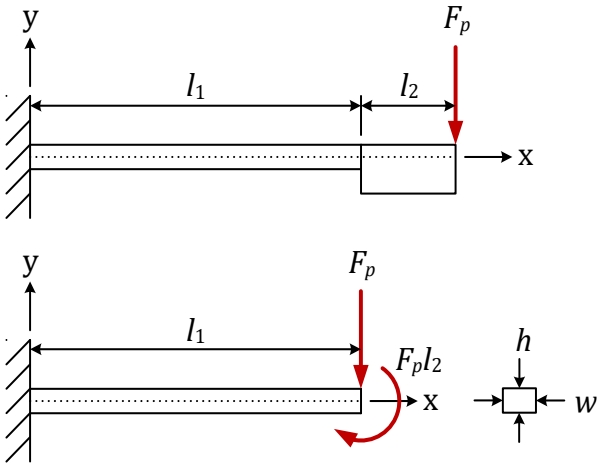

Figure 4.15: Free-body diagram of an end-loaded, rectangular cross-section, cantilever flexure.

This cantilever consists of two different cross-sectional areas. The end of the flexure is intended to be rigid in comparison to the rest of the beam so that the cable can be terminated here and the flexure can be locked out via some mechanical means. As a result the end of the flexure is significantly larger in height and width and is significantly shorter in length. For the purpose of this analysis, it is assumed that its deflection is negligible with respect to the rest of the flexure. Only the small cross-section of the flexure, $0 \leq x \leq l_1$, will be considered in terms of deflection.

The area moment of inertia of the solid, rectangular section about its neutral axis is given by equation 4.52

$$I = \frac{wh^3}{12} \tag{4.52}$$

and its section modulus is given by equation 4.53.

$$Z = \frac{wh^2}{6} \tag{4.53}$$

Here the variable w represents the width of the flexure and h represents its height as depicted in Figure 4.15.

Using the principle of superposition, the deformation of the flexure is obtained using the linear combination of the two individual loading conditions. The first condition considers only the deflection of the flexure due to the point load and the second condition considers only the deflection of the flexure due to the moment load.

The shear force, bending moment, neutral surface slope, and the displacement all as a function of x resulting from the point load is given by the following four equations respectively.

$$V_1(x) = F_p \tag{4.54}$$

$$M_1(x) = -F_p(l_1 - x) \tag{4.55}$$

$$\theta_1(x) = -F_p \frac{x(2l_1 - x)}{2EI} \tag{4.56}$$

$$y_1(x) = -F_p \frac{x^2(3l_1 - x)}{6EI} \tag{4.57}$$

The corresponding equations for the moment loading are also given by the following four equations.

$$V_2(x) = 0 \tag{4.58}$$

$$M_2(x) = -F_p l_2 \tag{4.59}$$

$$\theta_2(x) = -F_p \frac{l_2 x}{EI} \tag{4.60}$$

$$y_2(x) = -F_p \frac{l_2 x^2}{2EI} \tag{4.61}$$

From the principle of superposition the total shear force, bending moment, neutral surface slope, and displacement are simply the sum of the two components and are given by the equations below.

$$V(x) = V_1(x) + V_2(x) = F_p \tag{4.62}$$

$$M(x) = M_1(x) + M_2(x) = -F_p(l_1 + l_2 - x) \tag{4.63}$$

$$\theta(x) = \theta_1(x) + \theta_2(x) = -F_p \frac{x(2l_1+2l_2-x)}{2EI} \tag{4.64}$$

$$y(x) = y_1(x) + y_2(x) = -F_p \frac{x^2(3l_1+3l_2-x)}{6EI} \tag{4.65}$$

These equations are resourceful in not only ensuring the flexure does not fail due to the shear forces and bending moment, but also in determining the deflection of the flexure due to the desired preload. However, these equations only apply for $0 \leq x \leq l_1$. In order to determine the deflection at the free end of the flexure the rigid member of the flexure is taken into consideration. It is assumed that the larger cross-section remains rigid so its neutral surface slope remains constant. As a result, the slope of the neutral surface for $l_1 \leq x \leq l_2$ is given by equation 4.66

$$\theta(x) = -F_p \frac{l_1(l_1+2l_2)}{2EI} \tag{4.66}$$

and the corresponding deflection is given by equation 4.67.

$$y(x) = -F_p \frac{l_1\left(l_1(2l_1+3l_2)+3(l_1+2l_2)(x-l_1)\right)}{6EI} \tag{4.67}$$

The effective stiffness of the flexure at its free end can then be approximated using the following equation.

$$k = \frac{6EI}{l_1\left(l_1(2l_1+3l_2)+3l_2(l_1+2l_2)\right)} \tag{4.68}$$

Using these equations, the desired preload can be achieved at a specified deflection. As a result, the flexure can compensate and remove any slack in the cable while imparting the desired preload.

4.5.2 Design

The first step in designing the flexure is determining the necessary preload force to impose upon the cable. As seen in section 4.4.2 the minimum preload force for the maximum continuous torque of the motor is 7.271 N. Thus incorporating a safety factor of approximately 1.3 into the preload results in a desired preload force of approximately 9.5 N. A preload force of this magnitude helps to ensure the cable will not slip on the input pulley

and the tension of the cable will always remain positive despite the torque induced by the motor.

The second step in designing the flexure was determining the desired deflection of the beam at its end. A larger deflection allows for the ability to remove a greater amount of slack from the cable. Furthermore, a larger deflection allows for finer control over the force imposed on the cable due to the flexure's spring constant. As a result, the height and width of the beam were chosen to result in a deflection of approximately 3 mm at the end of the beam under a 9.5 N load. A deflection of this magnitude also ensured that the small deflection approximation used in the equations remained valid. The magnitude of 3 mm was accomplished by not only minimizing the cross-sectional area of the beam but by making the flexure as long as possible within the constraints of the output sector pulley. These dimensions and the remaining that fully define the flexure are tabulated in the following table.

Table 4.10: Flexure properties

Parameter	Value	Unit
Flexible length, l_1	55.0	mm
Rigid length, l_2	15.0	mm
Width, w	4.0	mm
Height, h	2.5	mm
Area moment of inertia, I	5.208	mm^4
Section modulus, Z	4.167	mm^3
Preload force, F_p	9.5	N
Max deflection at preload	3.016	mm
Effective stiffness, k	3.173	N/mm
Modulus of elasticity, E	68.98	GPa

To ensure the flexure would not fail due to yielding, the shear and bending moment diagrams of the beam across its length were derived and are shown in Figure 4.16. It is evident from the plot that the max shear force present in the beam is simply the preload force or 9.5 N. And as for the max bending moment, the largest value is at the base of the flexure where a 0.665 Nm moment is induced. The failure mode due to yielding results from this bending moment. However even at this loading condition a factor of safety of approximately 1.5 is still achieved.

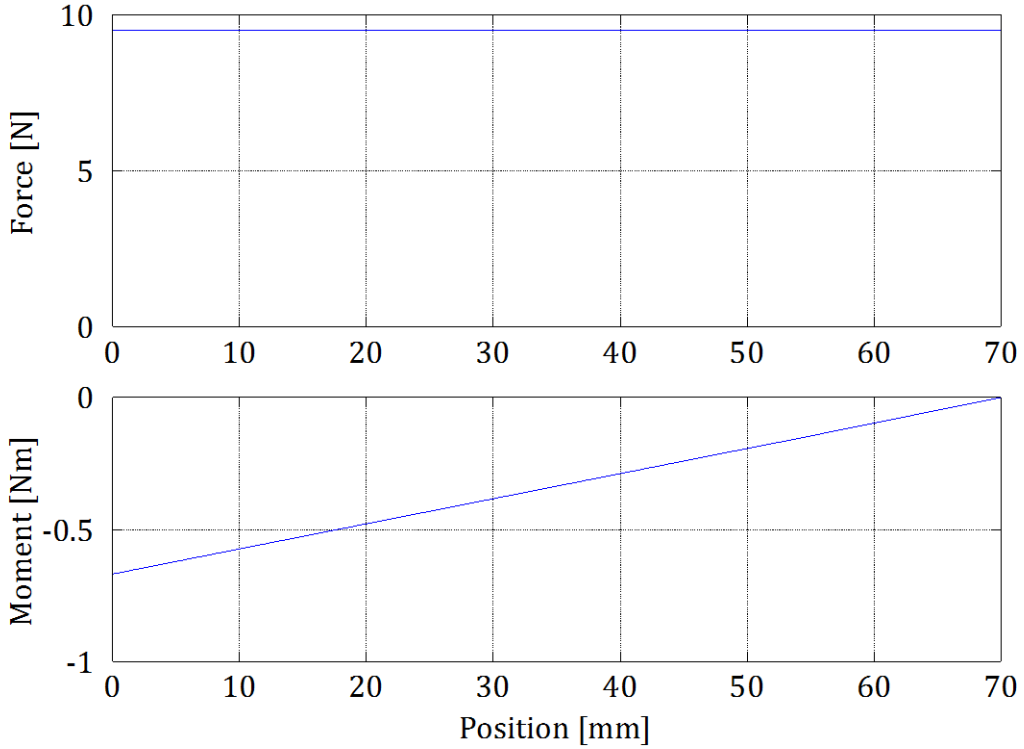

Figure 4.16: Plots of the shear force and bending moment across the flexure.

A unique characteristic of this design in comparison to other flexures, specifically cantilever beam configuration, is that the flexure was designed to be nominally in the deformed state when unloaded. Instead of designing the beam to be initially straight, the neutral axis of the flexure was designed using equations 4.65 and 4.67 for the deflected beam. The plots of these equations including the angle of deflection is shown in Figure 4.17. Designing the flexure in this manner is advantageous because under the proper loading the beam becomes straight. As a result, it is much easier and more precise to guarantee the desired preload force as opposed to a typical cantilever flexure. The flexure can be seen in both the nominal and deflected state in Figure 4.18.

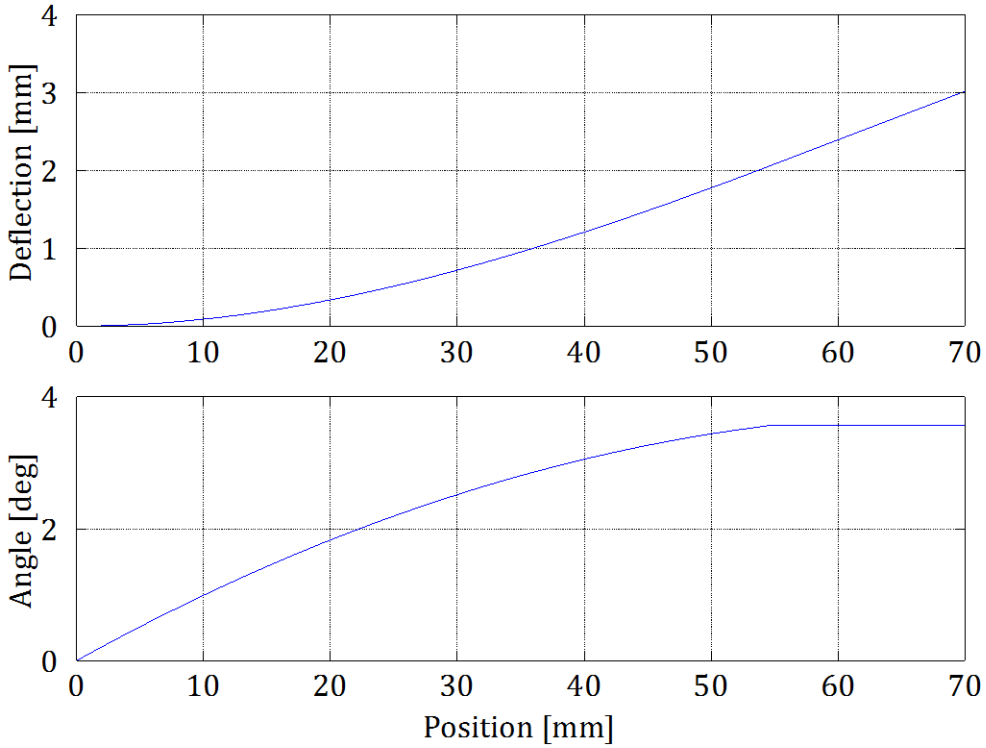

Figure 4.17: Plots of the flexure's unloaded neutral axis curve and its corresponding slope angle.

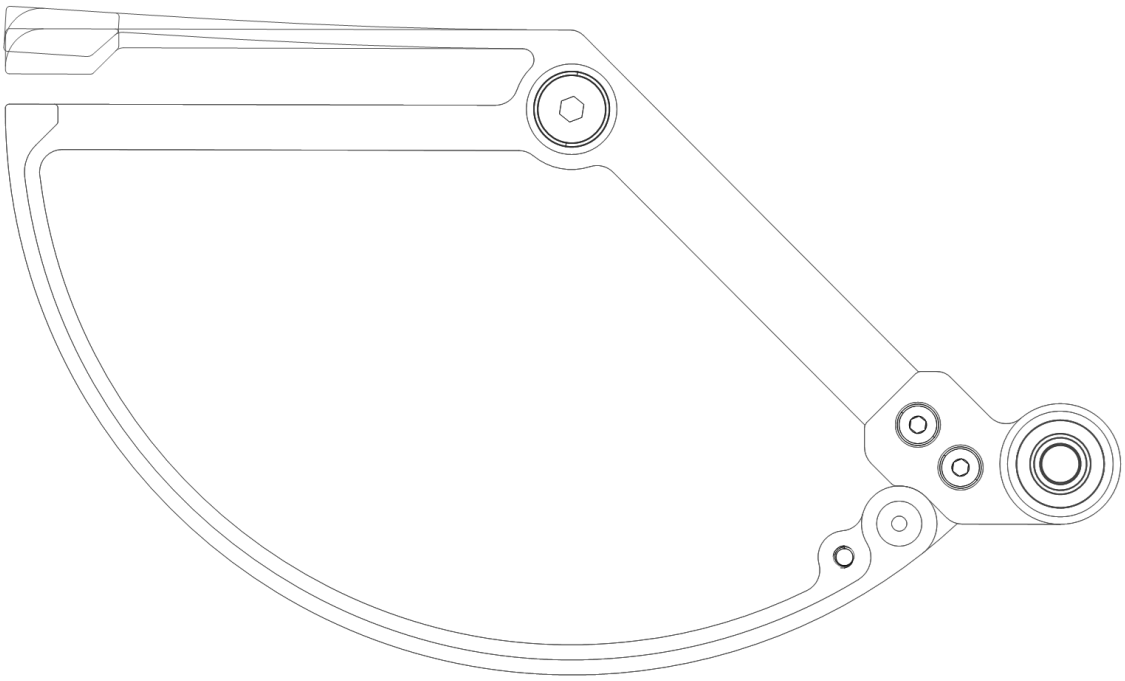

Figure 4.18: Output sector pulley with flexure shown in nominal and deflected state.

In order to confirm the validity of the calculations and ensure that the flexure will straighten from the desired preload, a finite element analysis was performed on the flexure in NX Unigraphics. The bore of the output sector pulley was constrained to be fixed and a force of

9.5 N was applied to the end of the flexure. The analysis resulted in the following figure showing the stresses induced in the flexure. It can be observed that the beam visually deflected into a straight configuration. The loading also agrees with the calculated bending moment diagram as the largest stresses are concentrated at the base of the flexure. In this case specifically the beam deflected 3.130 mm at its end, which is within 4% of the calculated value of 3.016 mm.

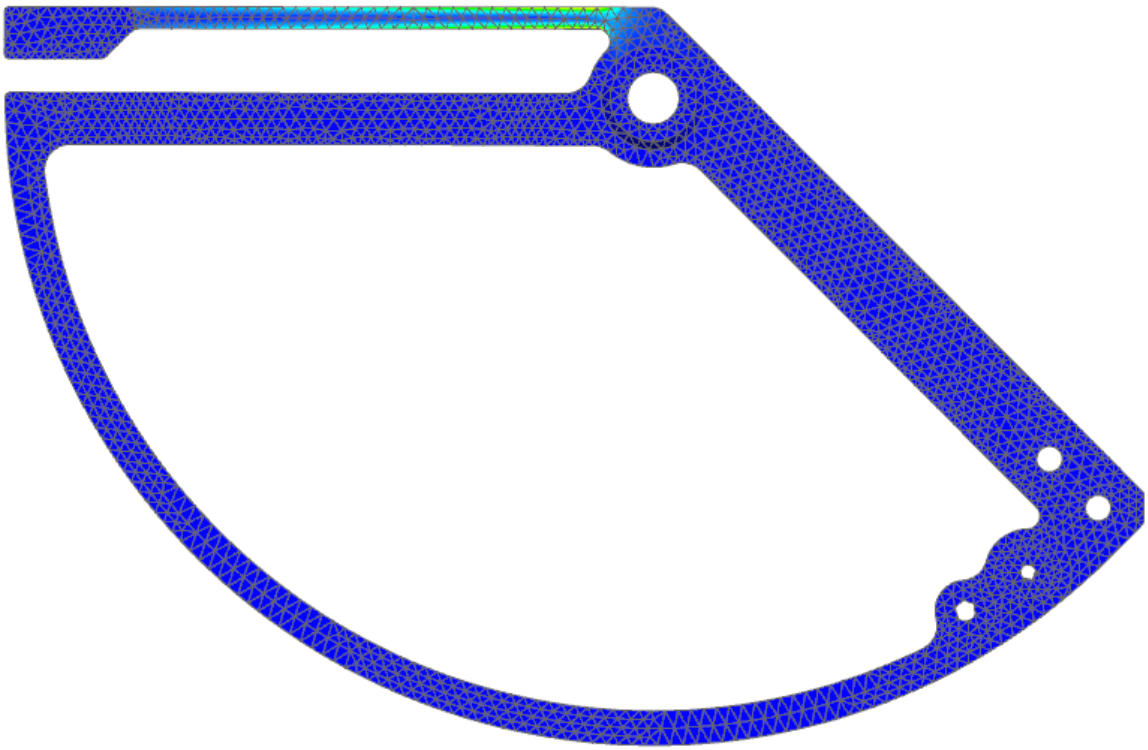

Figure 4.19: Finite element analysis of flexure showing beam in deflected state.

Although not pictured in the previous two figures, the flexure consists of the cable termination as well as a set screw at its end which is intended to lock out the beam and prevent it from deflecting further then desired. Not only does this help to remove the compliance of the flexure that would otherwise be introduced into the system but it also has the added advantage of being able to apply additional preload if necessary. This helps to compensate for the fact that the flexure stiffness cannot be easily changed. Furthermore, it helps to prevent the flexure from deflecting to the point of yielding, which could potentially render the flexure inoperable.

4.6 Rolling Elements

In order to minimize backlash and enable smooth, low friction operation of the actuator, rolling elements were incorporated into every joint. Specifically miniature, high-precision, stainless steel ball bearings were used. All of these bearings met a dimensional tolerance standard of 5 by the Annular Bearing Engineers Committee (ABEC). As a result all are made

to very tight tolerances with a shaft diameter tolerance of -0.005 mm to +0 mm. All the bearings are also pre-filled with grease, double-shielded to prevent the entry of particulates, and flanged for easy assembly. A table detailing the bearings used in the actuator is presented below.

Table 4.11: Ball bearing properties

Type	Style	Material	ABEC	Qty.	ID [mm]	OD [mm]	Dyn. Load [lbs.]
Ball	D-Shielded	440C SS	5	2	5	10	97
Ball	D-Shielded	440C SS	5	2	6	13	242

Despite the fact the bearings are high precision, they still possess a small amount of internal clearance. To remove this clearance and increase the accuracy and rigidity of the bearings a preload was applied in the axial direction to all the bearings in the assembly. A position preload, as opposed to a spring preload, is implemented as it results in a higher bearing stiffness and thus a greater assembly stiffness. The disadvantage of position preload is that it can vary under thermal expansion and wear. However, this is not an issue as the haptic controller will typically be used in a controlled environment and is not used often enough nor under sufficient external loading for wear to be a significant issue. In terms of the direction of the preload a configuration similar to a duplex back to back (DB), as opposed to a duplex face to face (DF), is implemented because it provides greater rigidity to moment loads. The basic preload configuration of the bearings for each of the joints can be seen in the following diagram. The preload must be carefully applied to each joint individually to ensure the preload is not excessive as this can induce undesired friction.

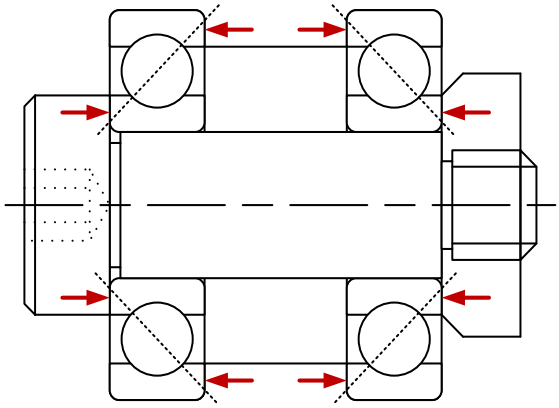

Figure 4.20: Diagram of the preload configuration used in the actuator's ball bearings.

4.7 Structural Elements

The structural elements of the actuator were designed to both decrease the perceived mass and inertia while increasing its stiffness whenever possible. The components of the actuator that were explicitly designed are shown in Figure 4.21. All of the components pictured were

manufactured with a CNC mill or lathe using 6061-T6 aluminum due to its high stiffness to weight ratio as well as its ease of machinability.

The structure that supports both the motor and the output sector pulley were designed to be exceptionally rigid. For these components in particular, weight was not a concern as it did not influence the perceived mass and inertia as seen by the operator. This principle also applies to the base. Thus these components exhibit a much greater stiffness with respect to the rest of the actuator. As for the input and output pulley, mass and inertia were critical and as such material was only allocated to support the necessary design features while still respecting the stiffness compromise.

Modularity was also a factor in the design although not as influential. Here the output of the actuator was designed as an interchangeable component independent of the output pulley. In doing so the moment arm could be modified without redesigning the rest of the actuator. Furthermore, not only can the actuator be mounted at multiple locations on its base, but the motor mount has an additional DoF via a slot so that it cannot only support other configurations and motors but so that the cable can be easily installed as well. To compensate for tolerances in the sliding surfaces of the slots, the main structural elements make use of dowel pins to ensure alignment of the input and output pulley and to reduce axial run-out.

Lastly, the design makes use of a single cylindrical hard stop to limit the range of motion of the actuator in the positive and negative direction. A single hard stop was used due to the restrictions of the design and the desire to not modify the output sector pulley. In this case the hard stop is a precision part as it is used to zero the incremental encoders of the motor on startup. Its cylindrical geometry ensures that a single point of contact is made during this initialization.

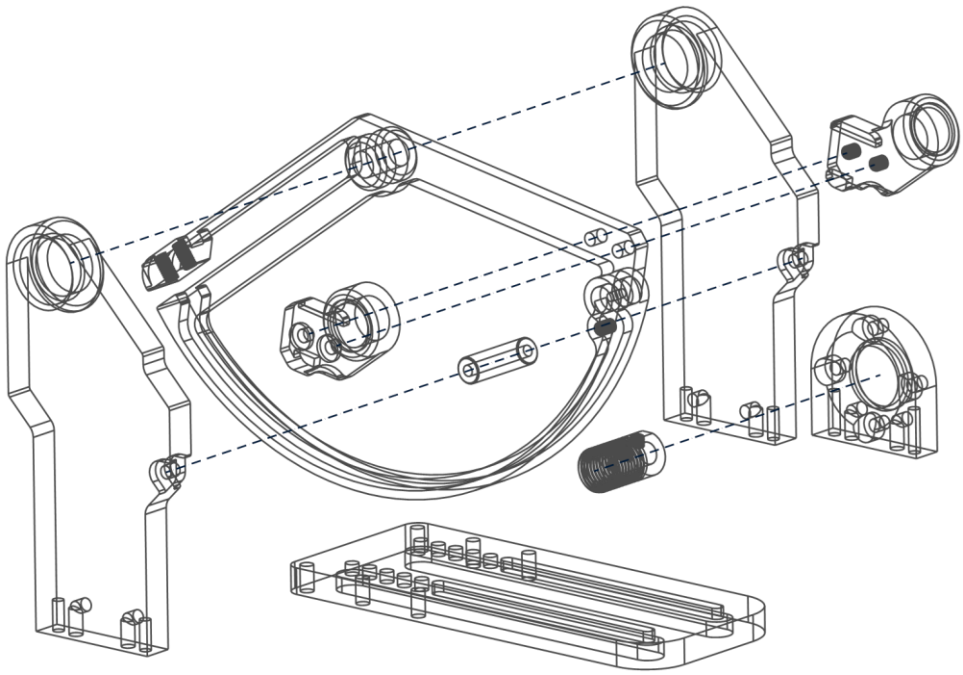

Figure 4.21: Exploded wireframe view of the structural elements used in actuator.

Chapter 5

Actuator Model

A system model was developed in order to gain a better understanding of how design changes would impact the performance of the actuator and its corresponding force control. Furthermore the model is valuable in terms of higher level controllers as it can be used as an observer or similar in a model-based control loop. The model takes the form of a linear, time-invariant, single-input, multiple-output, two-mass translational mechanical system of Figure 5.1 with corresponding free-body diagrams found in Figure 5.2. A translational equivalent of the rotary actuator was conceived as the model was developed from the view of the cable which is essentially a spring of stiffness k_1 joining two equivalent masses m_1 and m_2 representing the inertia of the input and output pulleys respectively. As for the remaining variables, $u_1(t)$ is the equivalent force from the motor torque, c_1 is the equivalent vicious damping coefficient of the input, k_2 is the equivalent spring stiffness of the output, c_2 is the equivalent vicious damping coefficient of the output, $z_1(t)$ is the equivalent displacement of the input pulley, and $z_2(t)$ is the equivalent displacement of the output pulley.

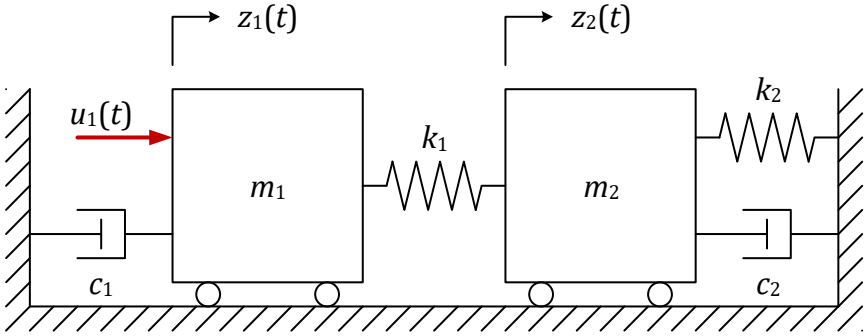

Figure 5.1: Equivalent translational mechanical system of the actuator.

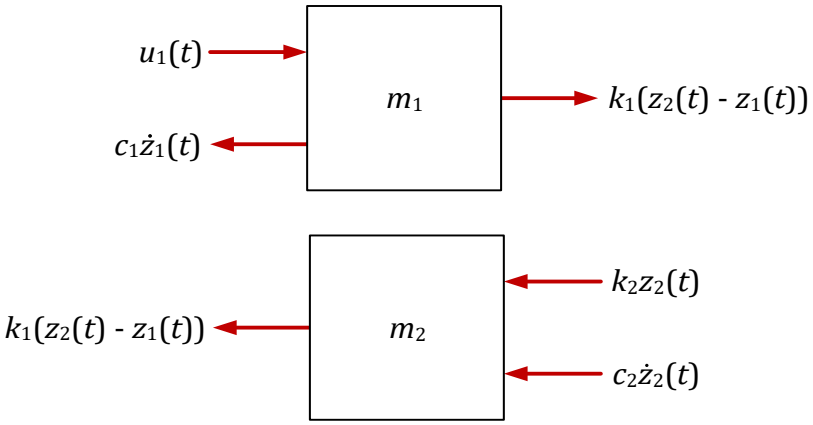

Figure 5.2: Free-body diagrams of the two equivalent system model masses.

5.1 Model Parameters

The equivalent model parameters had to be defined for each of the variables previously presented. Seeing as the model was developed from the perspective of the cable, all of the rotational based variables had to be converted to a translational equivalent. This was accomplished by using the following equations where m_i, c_i, and J_i is the mass, rotational viscous damping coefficient, and inertia respectively for $i = 1, 2$. The variable r_i in these equations represents the corresponding distance or radius from the axis of rotation.

$$m_i = \frac{J_i}{r_i^2} \quad i = 1, 2 \tag{5.1}$$

$$c_1 = \frac{b_1}{r_1^2} \tag{5.2}$$

As for the equivalent output stiffness k_2 and viscous damping coefficient c_2, the previous equations of 5.1 and 5.2 do not apply. This is a result of the fact that the actual output stiffness and damping coefficient are not rotational parameters but are translational. Furthermore, they are located at a radius other than the output pulley radius r_2 and thus cannot be directly substituted into the state space description. As a result, the following two equations were derived that convert the output stiffness k_o and viscous damping coefficient c_o to equivalent values as seen from the perspective of the cable. Here the variable r_o represents the radius of true output with respect to the axis of rotation.

$$k_2 = \left(\frac{r_o}{r_2}\right)^2 k_o \tag{5.3}$$

$$c_2 = \left(\frac{r_o}{r_2}\right)^2 c_o \tag{5.4}$$

Using the previously presented equations the equivalent translational model parameters for the final design can be seen in Table 5.1 at the end of this section. Each of the tabulated parameters is touched upon here for the sake of clarity.

First, in regards to the input, the inertia J_1 is the sum of the motor's rotor, encoder wheel, and input pulley inertia. The input radius r_1 is the effective radius of the input pulley as calculated in Section 4.4.2. The rotational viscous damping coefficient b_1 is the viscous damping due to the motor's rotor and is as defined in Section 4.1.1. And lastly the equivalent mass and damping coefficient were calculated using equations 5.1 and 5.2.

As for the output, the inertia J_2 consists of the inertia of the output sector pulley and associated components. The radius r_2 is the effective radius of the output pulley as calculated in Section 4.4.2. The output radius r_o is the moment arm from the rotational axis to the true output of the rotary actuator. And lastly, the output stiffness k_o and translational viscous damping coefficient c_o refers to the translational stiffness and damping at the true output of the actuator. Here the stiffness of the sensor used in the experiments of Chapter 6 is tabulated however these values will change depending on what is being actuated. It is also worth noting that the output viscous damping coefficient was included for completeness, however is not currently used in the model.

The last parameter to be defined is the cable stiffness k_1. Unfortunately, the stiffness of the cable is not a published value. Furthermore, most if not all cable drive designs either do not account for the cable stiffness or experimentally determine it from a tensile test. In this case the stiffness is approximated using the properties of the materials, the transmission design, and the metallic cross-sectional area of the cable. The generic equation for the axial stiffness of the cable is given by Equation 5.5

$$k_1 = S_1 \frac{E_1 A_1}{l_1} \tag{5.5}$$

where the variable E_1 is the modulus of elasticity of 302/304 (18-8) stainless steel and the variable A_1 is the metallic cross-sectional area of the cable as seen in Table 4.9. The effective length of the cable l_1 was approximated using Equations 4.45, 4.46, and 4.47 and the variable S_1 is included in the equation to act as a stiffness correction factor. Seeing as the stiffness of the cable is dependent upon the position of the actuator, the load history, as well as multiple other factors not being modeled nor of focus in this thesis, the correction factor was included to simplify the analysis and provide a means to better approximate the stiffness as well as tune the model to the true response. With that being said the stiffness of the cable is specific to the test setup to follow in the Experimental Results section. However, one could easily approximate the cable stiffness online, specifically as a function of position, and numerous publications do just this as mentioned in Chapter 2.

Table 5.1: System model parameters

Parameter	Value	Unit
Input		
Rotational		
Inertia, J_1	1.944e-06	kg·m^2
Radius, r_1	0.00500	m
Viscous damping coefficient, b_1	7.778e-04	Nm·s/rad
Translational		
Equivalent mass, m_1	0.0776	kg
Equivalent viscous damping coefficient, c_1	31.056	N·s/m
Output		
Rotational		
Inertia, J_2	2.117e-04	kg·m^2
Radius, r_2	0.0754	m
Radius, r_o	0.0800	m
Translational		
Sensor stiffness, k_o	9.8e7	N/m
Sensor viscous damping coefficient, c_o	0.0	N·s/m
Equivalent mass, m_2	0.0372	kg
Equivalent stiffness, k_2	1.104e+08	N/m
Equivalent viscous damping coefficient, c_2	0.0	N·s/m
Cable		
Translational		
Modulus of elasticity, E_1	1.9e+11	Pa
Metallic cross-sectional area, A_1	1.725e-7	m^2
Equivalent cable length, l_1	0.0612	m
Approximated spring stiffness	5.354e+05	N/m
Stiffness correction factor, S_1	0.225	-
Corrected stiffness, k_1	1.339e+05	N/m

5.2 State Space Description

Given the equivalent translational mechanical system of Figure 5.1, a mathematical system model was derived and then converted to a valid state-space representation. First a dynamic force balance was performed on each of the free-body diagrams seen in Figure 5.2 resulting in the following two linear, coupled, second-order ordinary differential equations of motion.

$$\sum F_1 = m_1\ddot{z}_1(t) = k_1[z_2(t) - z_1(t)] - c_1\dot{z}_1(t) + u_1(t) \tag{5.6}$$

$$\sum F_2 = m_2\ddot{z}_2(t) = -k_1[z_2(t) - z_1(t)] - k_2 z_2(t) - c_2\dot{z}_2(t) \tag{5.7}$$

Seeing as the equations of motion are both second-order, the state-space dimension must be four. Thus four state variables were defined according to the displacement and velocity for each mass as shown below where the state variables are given by $x_i(t)$ for $i = 1,2,3,4$.

$$
\begin{aligned}
x_1(t) &= z_1(t) \\
x_2(t) &= \dot{z}_1(t) = \dot{x}_1(t) \\
x_3(t) &= z_2(t) \\
x_4(t) &= \dot{z}_2(t) = \dot{x}_3(t)
\end{aligned}
\tag{5.8}
$$

The system can then be written as the coupled system of four first-order ordinary differential equations given by 5.9. Here the equations 5.6 and 5.7 have been substituted and normalized by their corresponding masses.

$$
\begin{aligned}
\dot{x}_1(t) &= x_2(t) \\
\dot{x}_2(t) &= \frac{-k_1}{m_1}x_1(t) + \frac{-c_1}{m_1}x_2(t) + \frac{k_1}{m_1}x_3(t) + \frac{1}{m_1}u_1(t) \\
\dot{x}_3(t) &= x_4(t) \\
\dot{x}_4(t) &= \frac{k_1}{m_2}x_1(t) + \frac{-(k_1+k_2)}{m_2}x_3(t) + \frac{-c_2}{m_2}x_4(t)
\end{aligned}
\tag{5.9}
$$

The state-space representation can then be represented in the general form given by the state differential equation and algebraic output equation of 5.10

$$
\begin{aligned}
\dot{\mathbf{x}}(t) &= \mathbf{A}\mathbf{x}(t) + \mathbf{B}u(t) \\
\mathbf{y}(t) &= \mathbf{C}\mathbf{x}(t) + \mathbf{D}u(t)
\end{aligned}
\tag{5.10}
$$

where the coefficient matrices **A**, **B**, **C**, and **D**, are given by the following four equations respectively.

$$
\mathbf{A} = \begin{bmatrix}
0 & 1 & 0 & 0 \\
\frac{-k_1}{m_1} & \frac{-c_1}{m_1} & \frac{k_1}{m_1} & 0 \\
0 & 0 & 0 & 1 \\
\frac{k_1}{m_2} & 0 & \frac{-(k_1+k_2)}{m_2} & \frac{-c_2}{m_2}
\end{bmatrix}
\tag{5.11}
$$

$$
\mathbf{B} = \begin{bmatrix}
0 \\
\frac{1}{m_1} \\
0 \\
0
\end{bmatrix}
\tag{5.12}
$$

$$
\mathbf{C} = \begin{bmatrix}
0 & 0 & k_2 & c_2 \\
1 & 0 & 0 & 0 \\
0 & 0 & 1 & 0
\end{bmatrix}
\tag{5.13}
$$

$$
\mathbf{D} = \begin{bmatrix}
0 \\
0 \\
0
\end{bmatrix}
\tag{5.14}
$$

Using these coefficient matrices results in the input to the system being the equivalent motor force and the outputs as the induced force in the equivalent output spring and damper as

well as the equivalent translational input and output pulley displacement. Here the displacements are measured from the neutral spring equilibrium location of each mass.

In order to have the motor current as the input and the outputs as the true output force and rotational input and output position in radians the coefficient matrices **B** and **C** were modified as shown in equations 5.15 and 5.16 respectively.

$$\mathbf{B} = \begin{bmatrix} 0 \\ \frac{k_t}{r_1 m_1} \\ 0 \\ 0 \end{bmatrix} \tag{5.15}$$

$$\mathbf{C} = \begin{bmatrix} 0 & 0 & \frac{r_2 k_2}{r_o} & \frac{r_2 c_2}{r_o} \\ \frac{1}{r_1} & 0 & 0 & 0 \\ 0 & 0 & \frac{1}{r_2} & 0 \end{bmatrix} \tag{5.16}$$

Using these coefficient matrices results in a system model completely analogous to the actuator.

Chapter 6

Experimental Results

The ability of the actuator to produce high fidelity forces was quantified via experimental means. This includes the frequency response as well as the step response of the open-loop force control of the actual system and the model. This section specifically focuses on these experiments and the validation of the design. The model of the experimental setup used to test the design can be seen in Figure 6.1 and its corresponding communication structure can be seen in the diagram of Figure 6.2. The test setup made use of a CNC mill not pictured to rigidly hold the base of the actuator in its vice as well as the shaft of the output load cell in its collet. A CNC mill was used as the test bench because it provided an exceptionally rigid structure to test the actuator in with little required modification or additional parts.

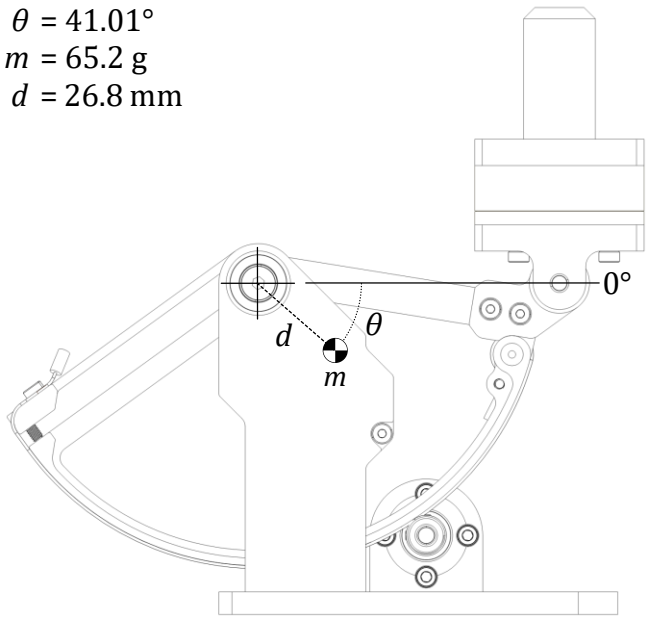

Figure 6.1: Model of the experimental setup used to test the actuator.

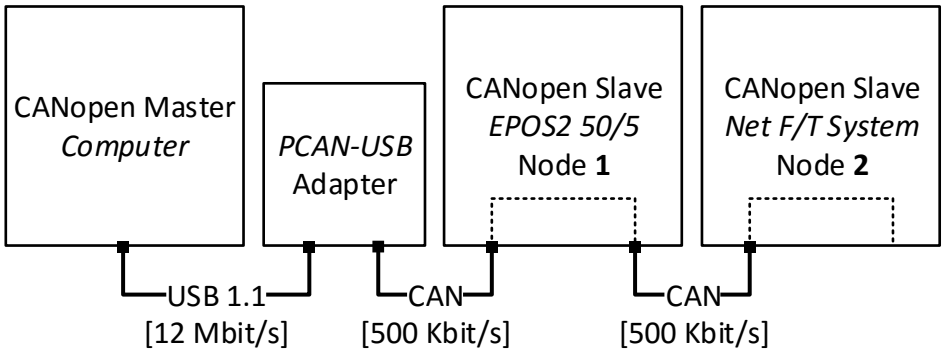

Figure 6.2: Communication diagram of the actuator test system.

The load cell used to measure the force output was an ATI Mini45 six-axis force torque transducer and its corresponding Net F/T signal conditioning board. Both the transducer and conditioning board can be seen in Figure 6.3. This transducer was chosen mostly as a result of availability in addition to its ability to be networked on a CAN bus. Consequently, its range is not idea for measuring the expected forces from the actuator. Despite this fact for a typical 16-bit data acquisition system the forces can be resolved accurately to less than a quarter of a Newton, and even more so when the noise is filtered from the signal. A benefit of the signal conditioning board is that it can be interfaced via the same CAN network as the motor controller. Unfortunately, as opposed to the 1 Mbit/s speeds of the motor controllers, the ATI signal conditioning board is only capable of 500 Kbit/s which restricted the speed of the bus and thus the sample rate to approximately 420 Hz in the test. Despite this the sensor proves sufficient in collecting the data to the necessary accuracy and speed to quantify the actuators performance.

Figure 6.3: ATI Mini45 six-axis force torque transducer and its corresponding Net F/T signal conditioning board.

It is worth noting that due to the inherent eccentric mass of the actuator design, as shown in Figure 6.1, a gravitational force is induced in the transducer. To prevent this induced force

from affecting the experimental results the force transducer was biased to zero prior to each test. When implementing the actuator in the haptic controller, a feedforward term is used to account for the eccentric mass and actively compensate for the gravitational effects so that they do not interfere with the force feedback.

6.1 Frequency Response

The first test performed on the actuator dealt with determining its frequency response. To excite all the frequencies of the actuator, a chirp signal also known as a swept-frequency cosine was used. The signal begins at 0.01 Hz and sweeps to 210 Hz logarithmically in approximately 40 seconds. A span of this length of time was chosen to produce 2^{14} samples at a sample rate of 420 Hz. The amplitude of the chirp signal was chosen to be 1.5 A which makes use of approximately half of the range of the max continuous current of the motor. A current of this amplitude was necessary to create a high signal to noise ratio as well as excite all the frequencies of the actuator. The resulting excitation signal can be seen in Figure 6.4 and the corresponding response signal in Figure 6.5.

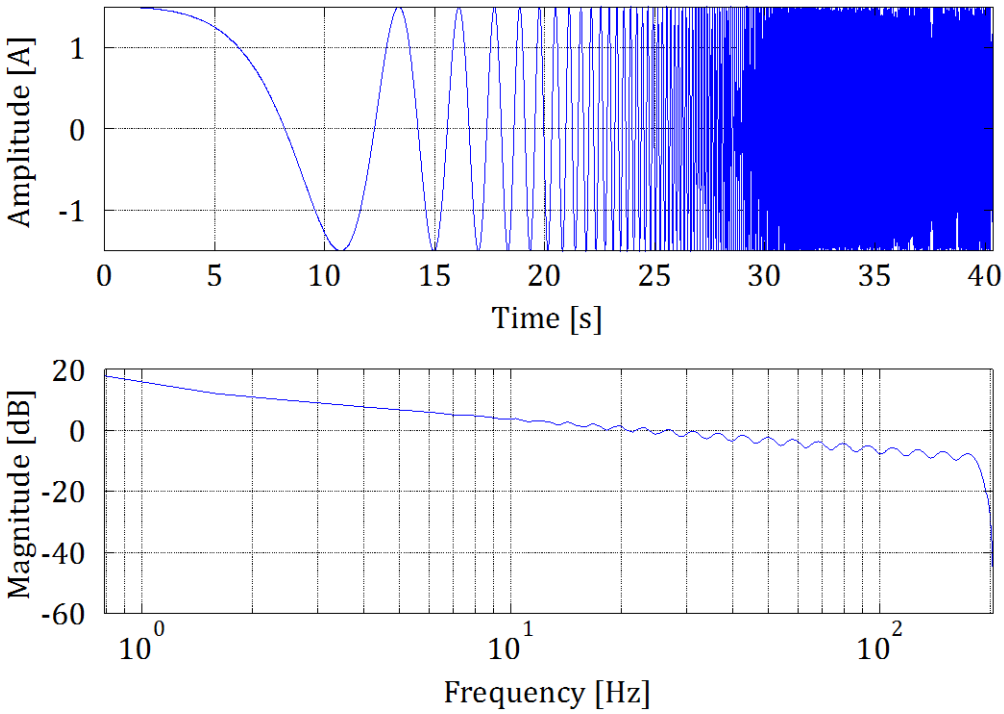

Figure 6.4: Power spectrum and time domain plot of the excitation signal.

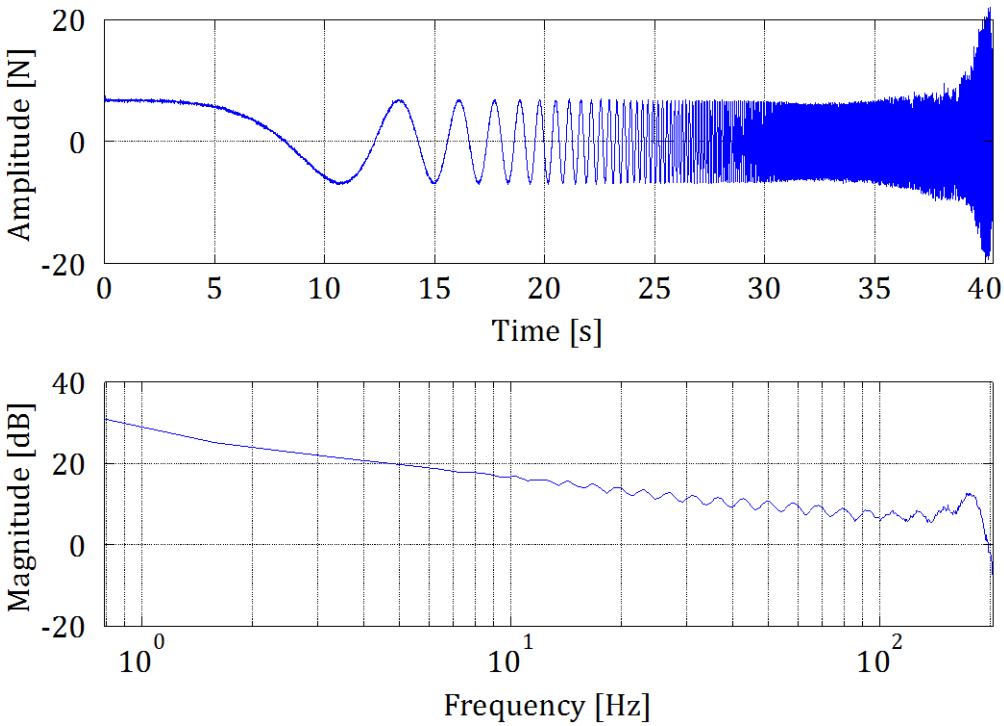

Figure 6.5: Power spectrum and time domain plot of the response signal.

Using the excitation and response signals, the frequency response function was constructed using the H1 estimator. Welch's method for spectral estimation was used to calculate the cross power spectral density used in the estimator. This was performed to reduce the effects of noise and produce a cleaner frequency response function. Ultimately 32 windows were used in Welch's method with an overlap of 50%, which resulted in a frequency resolution of approximately 0.820 Hz. In doing so the frequency response function of the actuator can be seen in Figure 6.6 for both the actual system and the model.

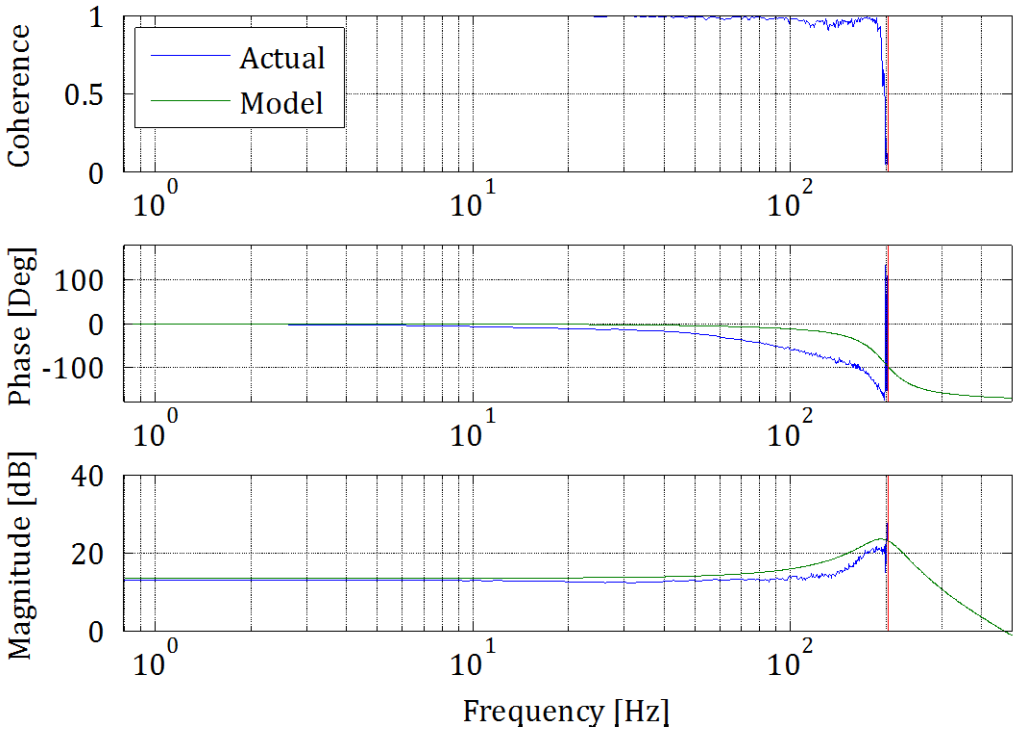

Figure 6.6: Frequency response function of the actual system and the system model.

As can be observed from the figure, not only does the model approximate the response of the system well, especially considering all the parameters were estimated, but the excitation and response of the actual system show very high coherence (>0.9) throughout the entire frequency range. Unfortunately the test setup was unable to sample at a high enough frequency to fully characterize the bandwidth of the actual system. However, the bandwidth can be estimated by the model as approximately 300 Hz, which represents the range of frequencies in which the actuator can replicate. It can also be observed that the bandwidth is relatively flat from DC to approximately 130 Hz which is a desired trait as the force amplitude is relatively invariant to its frequency in this range. However, near the resonance at approximately 190 Hz the force amplitude rises approximately 10 dB above the DC gain. This resonance can be avoided using a notch filter to reduce the amplitude at higher frequencies, however this is most likely not necessary since most imparted frequencies are below 130 Hz. In regards to the DC gain, the small offset (0.54 dB) can almost be entirely accounted for by the no load current that was not compensated for in the state space model. This is ideal as the no load current can easily be accounted for online, removing this disparity. However, at higher frequencies it appears there is additional viscous damping friction that is not being accounted which most likely originates from the output pulley and cable transmission. This viscous damping introduces additional phase shift into the system while also reducing the magnitude of the resonance peak. Fortunately this occurs at higher frequencies and thus is not much of a cause for concern.

As can be concluded from the frequency response, the actuator does exhibit properties that were desired, which includes a relatively flat and wide bandwidth with little phase shift. With a bandwidth of approximately 300 Hz, a multitude of frequencies can be replicated to the

operator. Furthermore, the higher level controller is capable of running at approximately twice the bandwidth of the actuator. This is ideal and necessary in order to take full advantage of the entire force reflection capability of the actuator.

6.2 Step Response

The second test performed dealt with determining the step response of the actuator. The step response is significant because the actuator is commanded via a discretized signal which upon closer observation is made up of small zero-order hold steps. As a result, the response of the actuator to a step input can be very resourceful in quantifying its performance, especially to discretized excitations. In this case a step of amplitude ± 1.5 Amps (± 7.2 N) and duration of approximately 1 second each was used to excite the actuator. The response of both the actual system and the discretized model to this excitation can be seen in Figure 6.7 and the corresponding performance measures of the actual system can be seen in Table 6.1.

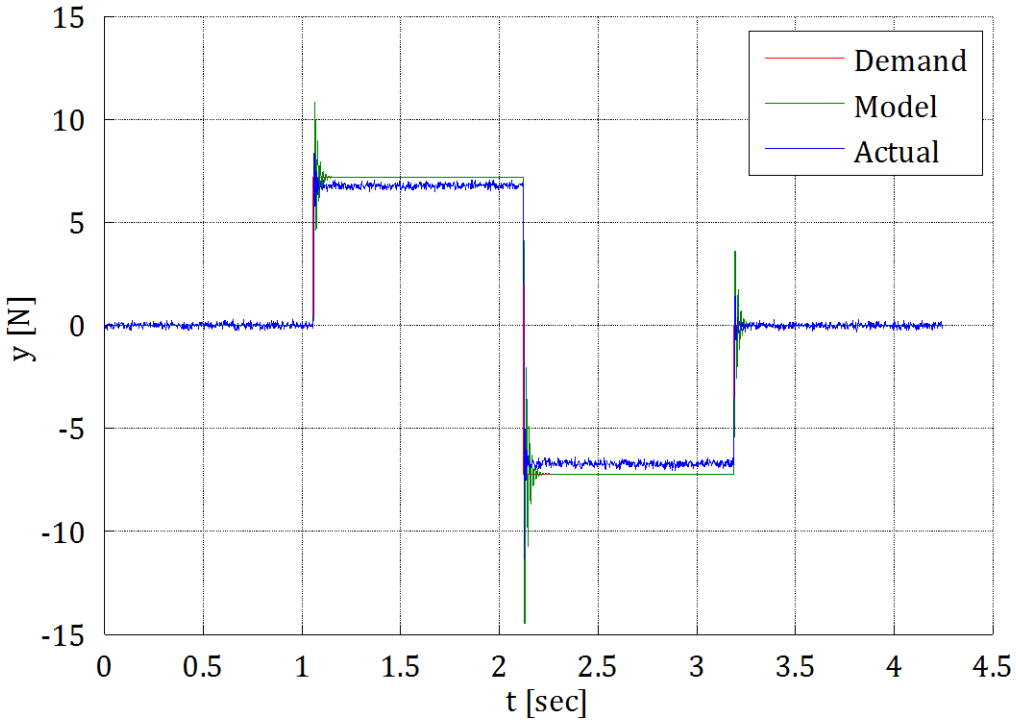

Figure 6.7: Step response of the actual system and the system model.

Table 6.1: Actuator step response performance measures

Parameter	Value	Unit
Sample rate	420	Hz
Sample period	2.4	ms
Rise time (10% to 90%)	3	sample periods
Time constant (63.2%)	2	sample periods
Settling time (2%)	15	sample periods
Overshoot	24	%
Undershoot	15	%
Steady-state error	0.45	N

From the figure it can be observed that the response of the actual system is quite fast with a rise time and time constant of only 3 and 2 sample periods respectively. However this is no surprise as the rise time and time constant are both related to the bandwidth of the system. Seeing as the bandwidth is so large, it was expected that these performance measures would be quite small. However, the system is so responsive that it exhibits an overshoot of approximately 24%, mostly a result of the cable elasticity. Seeing as the actuator is interfaced with an exceptionally rigid or relatively massive object with little viscous damping, overshoot was expected to occur. However, the operator will introduce additional damping into the system, via the output viscous damping c_o from section 5.1, which will counteract the overshoot and reduce the oscillation. As a result it is acceptable for the actuator to exhibit some means of overshoot as additional damping will occur from an external source when in use. As for the steady state error of 0.45 N (0.094 A), this can be entirely accounted for by the no load current of the motor (0.290 ± 0.145 A), which was also not accounted for in the state space model.

The system model, discretized using the zero-order hold method, exhibits a much greater overshoot with respect to the actual system. This is mostly a result of not accounting for the no load current as well as additional viscous damping in the transmission. It is apparent from the frequency response function and the step response that additional contributors to the damping coefficient are present in the actuator. However by using the frequency and step responses the model can be tuned using additional correction factors to better approximate the actual system if desired. Furthermore, as mentioned in section 6.1, the no load current can be easily incorporated into the input of the model and account for any steady-state discrepancies between the actual and demanded force in the step response as shown in Figure 6.8.

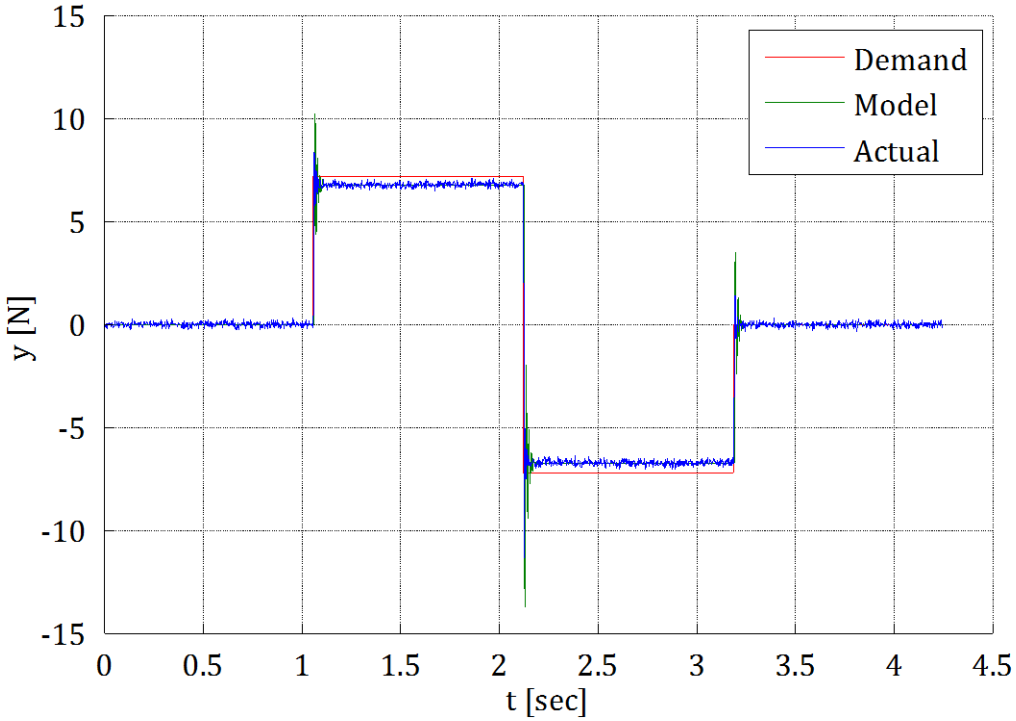

Figure 6.8: Step response of the actual system and the system model accounting for the no load current of 0.094 A.

A significant advantage of having a system model especially for a cable drive is the ability to actively compensate for the cable deflection online. Using the position outputs of the state space description, the encoder counts due to the cable deflection can be accounted for. The predicted quadcounts of the encoder versus the actual quadcounts observed during the step response can be seen in Figure 6.9. It can be observed that the model is capable of predicting the rotor rotation due to the cable deflection within 2 quadcounts at steady state, which can be further decreased to 1 quadcount when accounting for the no load current as shown in Figure 6.10. Furthermore there is no backlash evident in the response. This is extremely important in terms of haptic feedback as the position of the actuator determines the demanded force. Thus having an accurate approximation of the true position is essential to the stability and force fidelity of the actuator. By accounting for the cable deflection the true position can be more accurately quantified. A tuned system model could potentially even compensate for transients in addition to steady states, which could prove to be very powerful when commanding dynamic forces.

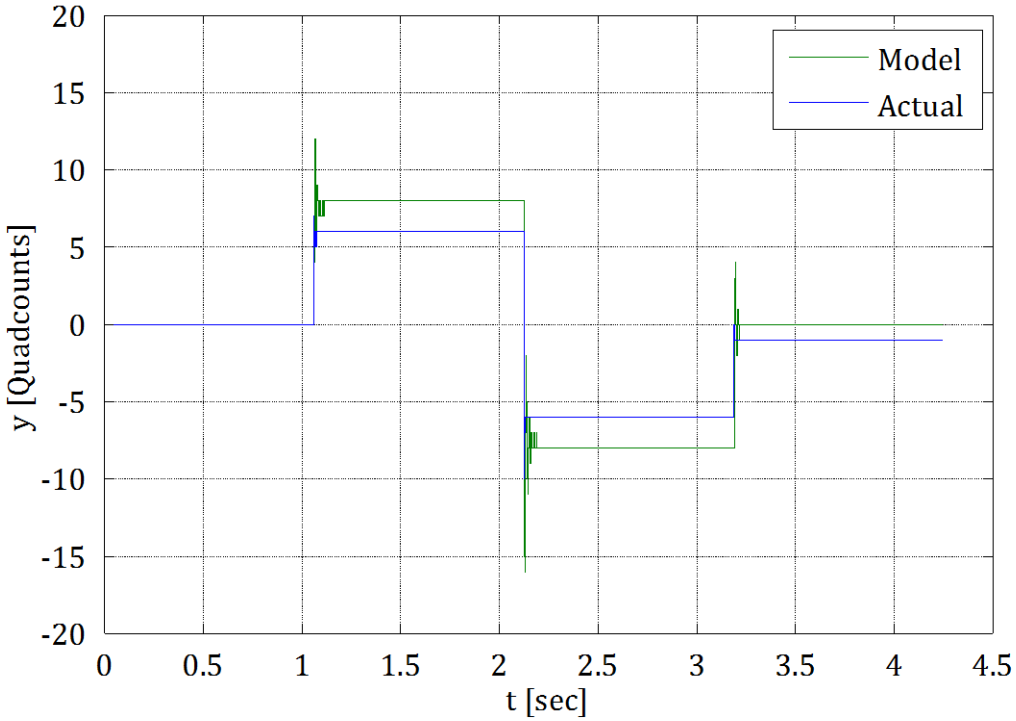

Figure 6.9: Actual quadcounts and predicted quadcounts resulting from the deflection of the cable during testing.

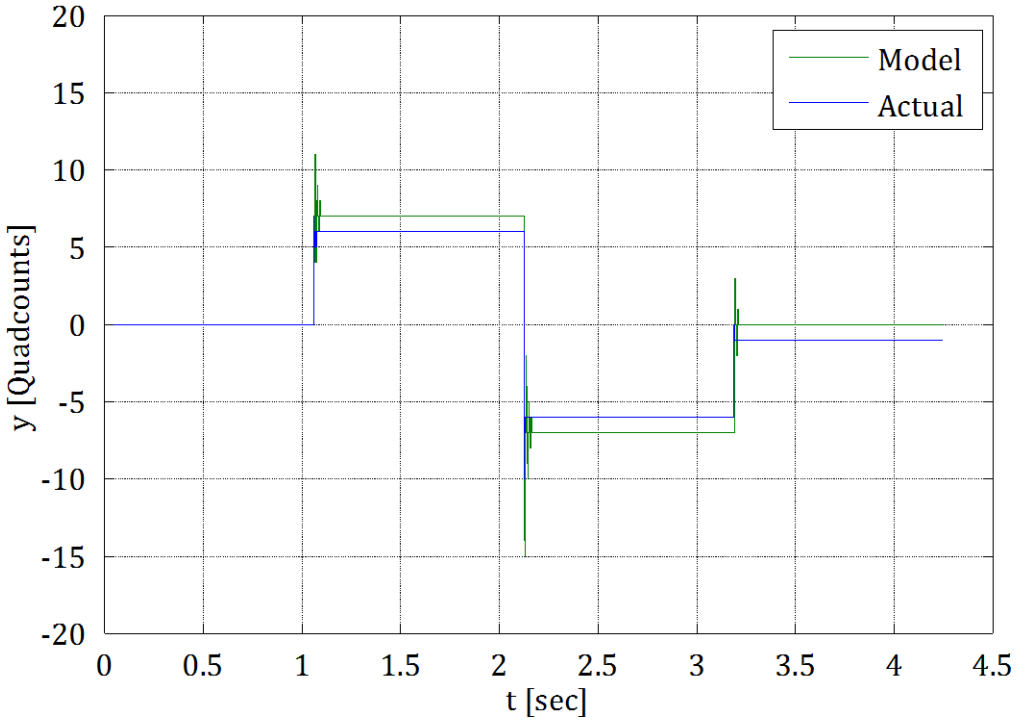

Figure 6.10: Actual quadcounts and predicted quadcounts resulting from the deflection of the cable during testing while accounting for the no load current of 0.094 A.

Chapter 7

Conclusion

This thesis sought to present the design of a cable-driven sectorial rotary actuator. This was accomplished by first presenting the review of research literature previously conducted for impedance-class haptic devices. This literature included current designs for haptic interfaces, the design principles that defined the presented designs, and the transmissions that drove them. Then an overview of the haptic controller in which the developed actuator was to be implemented was discussed. This discussion included the configuration of the controller, its corresponding kinematics and dynamics, its workspace, its force feedback properties, and a brief introduction to its actuation system. Once this framework was established, the actuator analysis and design was presented with a comprehensive discussion of each component of the design and its corresponding impact on the performance of the actuator. Having conveyed the design, an actuator model capable of simulating and weighing design tradeoffs in the actuator was then presented. Once both the actuator and corresponding model were conveyed, the experimental tests used to validate the design were then bestowed. A frequency response and a step response were ultimately used to quantify the ability of the actuator and the model to replicate forces accurately and realistically.

The goal of this study was to develop a high performance actuator for use as a force-source in a force feedback haptic controller. By upholding the strict design principles of an ideal force-source actuator as presented in the literature review, the designed actuator does successfully replicate forces accurately and realistically. Its capabilities are easily apparent as conveyed from the experimental results section. Any inaccuracies, specifically due to the small frictional forces, can almost entirely be accounted for by the no load friction of the motor. Thus the achieved performance is ultimately a result of the design possessing all of the desired properties which includes high backdrivability, zero backlash, high bandwidth, high stiffness, high resolution, low friction, low inertia, low mass, large range, and high isotropy. However this performance would not have been possible if it were not for the analytical tools conceived in the design including the simplified linear model of the actuator. These tools proved to be invaluable not only in the design but in the control of the actuator

as well. Although the model parameters were completely approximated, the model was still able to successfully predict the behavior of the actuator quite accurately in addition to the deflection of the cable. Thus this design and its corresponding analytical tools could prove to be quite resourceful to the development of other cable-driven designs.

7.1 Future Work

Due to the rate of progression of the haptic community numerous publications and areas of research are continually emerging for haptic interface devices. However, actuation performance is still a significant limitation to haptic interfaces. Thus any contributions to this area are significant. The initial tests conducted on the actuator presented in this thesis proved that it is very capable at reflecting forces via open-loop control. However, there are still a number of issues with the design which could benefit from additional research and these areas are presented below.

The stiffness of the cable is typically the limiting factor in the performance of a cable drive as is the case in this design. This is a mostly a consequence of the design implementing a single cable serially. However implementing multiple cables in parallel could potentially prove beneficial to increasing the stiffness of the drive without sacrificing other design criteria. Implementing multiple cables also has the benefit of increasing the load capability as well as the bandwidth of the system although sacrifice will be made in design complexity.

The preload of the cable is a significant factor in the induced friction and stresses in the assembly. However, the preload also plays a factor in the stiffness of the cable. Multiple publications report that the stiffness of the cable increases with greater preload. Thus it would be worthwhile to quantify the cable stiffness and induced friction as a function of preload. In doing so an optimal cable preload could be achieved for a desired cable stiffness and friction.

A significant limitation of the design is in the maximum continuous current of the motor. Seeing as the haptic controller is typically operated in a quasi-static configuration. The motor is under constant load and at times can and does approach and exceed the maximum continuous current. In order to increase the effective torque density of the motor, active cooling can be explored to dissipate the additional generated heat. This would thus have the benefit of allowing the motors to run at greater currents, which in turn means smaller motors with lower inertia can be used.

As currently designed, the actuator determines the position of the output from the encoder on the motor. Although this has the advantage of creating greater resolution at the output due to the transmission, it prevents the controller from knowing the true position of the output due to deflection and drift. As a result the system model must be used to compensate for the cable deflection. However, if this is not desired then an encoder on the output needs to be implemented so that the true position of the output can be known.

Lastly, when dealing with an open-loop control system, tolerances can become a significant issue. As it currently stands, the actuator components have not been fully characterized in terms of tolerances. Motor properties especially are known to fluctuate with respect to what is listed in their datasheets. Thus a relatively simple way to improve the performance of the actuator is to confirm all of the variables provided by manufacturers and to actually quantify those that are not.

Bibliography

[1] H. Tan, B. Eberman, M. Srinivasan and B. Cheng, "Human Factors for the Design of Force-Reflecting Haptic Interfaces," *Dynamic Systems and Control,* vol. 55, no. 1, pp. 353-359, 1994.

[2] V. Hayward and K. MacLean, "Do It Yourself Haptics: Part II," *Robotics & Automation Magazine, IEEE,* vol. 15, no. 1, pp. 104-119, March 2008.

[3] K. MacLean, "Haptic Interaction Design for Everyday Interfaces," *Reviews of Human Factors and Ergonomics,* vol. 4, no. 1, pp. 149-194, October 2008.

[4] V. Hayward and K. MacLean, "Do It Yourself Haptics: Part I," *Robotics & Automation Magazine, IEEE,* vol. 14, no. 4, pp. 88-104, Dec. 2007.

[5] M. O'Malley and A. Gupta, "Haptic Interfaces," in *HCI Beyond the GUI: Design for Haptic, Speech, Olfactory, and Other Nontraditional Interfaces*, San Francisco, Morgan Kaufmann Publishers Inc., 2008, pp. 25-73.

[6] H. S. Kim, "Mechanism Design of Haptic Devices," in *Advances in Haptics*, InTech, 2010, pp. 283-298.

[7] Haption, [Online]. Available: http://www.haption.com/.

[8] Geomagic, [Online]. Available: http://www.geomagic.com/.

[9] T. Massie and K. Salisbury, "The Phantom Haptic Interface: A Device for Probing Virtual Objects," *ASME Dynamic Systems and Control,* vol. 55, no. 1, pp. 295-299, 1994.

[10] M. Cavusoglu, D. Feygin and F. Tendick, "A Critical Study of the Mechanical and Electrical Properties of the Phantom Haptic Interface and Improvements for High Performance Control," *Presence,* vol. 11, no. 5, pp. 555-568, 2002.

[11] M. Cavusoglu and D. Feygin, "Kinematics and Dynamics of Phantom Model 1.5 Haptic Interface," *UC Berkeley ERL Memo M01/15,* 2001.

[12] A. Tahmasebi, B. Taati, F. Mobasser and K. Hashtrudi-Zaad, "Dynamic Parameter Identification and Analysis of a Phantom Haptic Device," in *IEEE Conference on Control Applications*, Toronto, Canada, 2005.

[13] Quanser, [Online]. Available: http://www.quanser.com/.

[14] Force Dimension, [Online]. Available: http://forcedimension.com/.

[15] Novint, [Online]. Available: http://www.novint.com/.

[16] L.-F. Lee, M. Narayanan, F. Mendel and V. Krovi, "Kinematics Analysis of In-Parallel 5 DOF Haptic Device," in *IEEE/ASME International Conference on Advanced Intelligent Mechatronics*, Montréal, Canada, 2010.

[17] A. Tobergte, P. Helmer, U. Hagn, P. Rouiller, S. Thielmann, S. Grange, A. Albu-Schaffer, F. Conti and G. Hirzinger, "The Sigma.7 Haptic Interface for MiroSurge: A New Bi-Manual Surgical Console," in *IEEE/RSJ International Conference on Intelligent Robots and Systems*, San Francisco, CA, 2011.

[18] S. Martin and N. Hillier, "Characterisation of the Novint Falcon Haptic Device for Application as a Robot Manipulator," in *Australasian Conference on Robotics and Automation (ACRA)*, Sydney, Australia, 2009.

[19] L. Birglen, C. Gosselin, N. Pouliot, B. Monsarrat and T. Laliberté, "SHaDe, A New 3-DOF Haptic Device," *IEEE Transactions on Robotics and Automation,* vol. 18, no. 2, pp. 166-175, 2002.

[20] J. Yoon and J. Ryu, "Design, Fabrication, and Evaluation of a New Haptic Device Using a Parallel Mechanism," *IEEE/ASME Transactions on Mechatronics,* vol. 6, no. 3, pp. 221-233, 2001.

[21] J. Arata, H. Kondo, M. Sakaguchi and H. Fujimoto, "A Haptic Device DELTA-4: Kinematics and its Analysis," *Third Joint Eurohaptics Conference and Symposium on Haptic Interfaces for Virtual Environment and Teleoperator Systems,* pp. 452-457, 2009.

[22] J.-W. Kim, D.-H. Park, H.-S. Kim and S.-H. Han, "Design of a Novel 3-DOF Parallel-Type Haptic Device with Redundant Actuation," *International Conference on Control, Automation and Systems,* pp. 2270-2273, 2007.

[23] J. Biggs and M. Srinivasan, "Haptic Interfaces," in *Handbook of Virtual Environments*, London, Lawrence Earlbaum, Inc., 2002, pp. 93-116.

[24] V. Hayward, O. Astley, M. Cruz-Hernandez, D. Grant and G. Robles-De-La-Torre, "Haptic Interfaces and Devices," *Sensor Review,* vol. 24, no. 1, pp. 16-29, 2004.

[25] J. Martin and J. Savall, "Mechanisms for Haptic Torque Feedback," in *Proceedings of the First Joint Eurohaptics Conference and Symposium on Haptic Interfaces for Virtual Environment and Teleoperator Systems*, 2005.

[26] B. Hannaford and A. Okamura, "Haptics," in *Springer Handbook of Robotics*, 2008, pp. 719-739.

[27] V. d. L. R.Q., L. P., F. E. and R. B., "The HapticMaster, a New High-Performance Haptic Interface," *Eurohaptics Conference,* pp. 1-5, 2002.

[28] V. Hayward and O. Astley, "Performance Measures for Haptic Interfaces," *Robotics Research: The 7th International Symposium,* pp. 195-207, 1996.

[29] D. Lawrence and J. Chapel, "Performance Trade-offs for Hand Controller Design," in *IEEE International Conference on Robotics and Automation*, 1994.

[30] O. Ma and J. Angeles, "Optimum Design of Manipulators Under Dynamic Isotropy Conditions," in *IEEE International Conference on Robotics and*, 1993.

[31] J. Abbott and A. Okamura, "Effects of Position Quantization and Sampling Rate on Virtual-Wall Passivity," *IEEE Transactions on Robotics,* vol. 21, no. 5, pp. 952-964, 2005.

[32] R. Brewer, A. Leeper and J. K. Salisbury, "A Friction Differential and Cable Transmission Design for a 3-DOF Haptic Device with Spherical Kinematics," in *IEEE/RSJ International Conference on Intelligent Robots and Systems*, San Francisco, CA, 2011.

[33] Barrett Technology Inc., [Online]. Available: http://www.barrett.com/.

[34] Y. Lu, D. Fan, D. Sheng and Z. Zhang, "Design Consideration for Precise Cable Drive," *Advanced Materials Research,* vol. 305, pp. 37-41, 2011.

[35] H. Jenkins and M. Nagurka, "Design and Control of Capstan-Pulley Draw System for Optical Fiber Manufacturing," in *Proceedings of the 9th Biennial ASME Conference on Engineering Systems Design and Analysis*, Haifa, Israel, 2008.

[36] S. Truong, J. Kieffer and A. Zelinsky, "A Cable-Driven Pan-Tilt Mechanism for Active Vision," in *Proceedings Australian Conference on Robotics and Automation*, 1999.

[37] J. Savall, J. Martín and A. Avello, "High-Performance Linear Cable Transmission," *Journal of Mechanical Design,* vol. 130, no. 6, 2008.

[38] G. Thomas, C. Gimenez, E. Chin, A. Carmedelle and A. Hoover, "Controllable, High-Force Application Using Elastic Cable Capstans," in *Proceedings of the ASME 2012 International Design Engineering Technical Conferences & Computers and Information in Engineering Conference*, Chicago, IL, 2012.

[39] E. Snow, "The Load/Deflection Behavior of Pretensioned Cable-Pulley Transmission Mechanisms," Massachusetts Institute of Technology, 1994.

[40] K. Cronin and J. Gleeson, "Variability in Output Torque of Capstan and Wrap Spring Elements," *Mechanism and Machine Theory,* vol. 68, pp. 49-66, 2013.

[41] J. Jung, N. Pan and T. Kang, "Capstan Equation Including Bending Rigidity and Non-Linear Frictional Behavior," *Mechanism and Machine Theory,* vol. 43, no. 6, p. 661–675, 2008.

[42] J. Jung, T. Kang and J. Youn, "Effect of Bending Rigidity on the Capstan Equation," *Textile Research Journal,* vol. 74, no. 12, pp. 1085-1096, 2004.

[43] J. Jung, N. Pan and T. Kang, "Generalized Capstan Problem: Bending Rigidity, Nonlinear Friction, and Extensibility Effect," *Tribology International,* vol. 41, no. 6, p. 524–534, 2008.

[44] A. J. Shashaty, "The Reduction of Capstan Effectiveness by Cable Bending Resistance," *Journal of Manufacturing Science and Engineering,* vol. 103, no. 3, pp. 319-323, 1981.

[45] J. Werkmeister and A. Slocum, "Theoretical and Experimental Determination of Capstan Drive Stiffness," *Precision Engineering,* vol. 31, no. 1, p. 55–67, 2007.

[46] L. Hu, T. Yonggang and S. Jun, "A Study on Drive Capstan Stiffness of Cable-Driven Picking Manipulator," *Applied Mechanics and Materials,* Vols. 220-223, pp. 1761-1766, 2012.

[47] O. Baser and E. I. Konukseven, "Theoretical and Experimental Determination of Capstan Drive Slip Error," *Mechanism and Machine Theory,* vol. 45, pp. 815-827, 2010.

[48] O. Baser and E. I. Konukseven, "Kinematic Model Calibration of a 7-DOF Capstan-Driven Haptic Device for Pose and Force Control Accuracy Improvement," in *Proceedings of the Institution of Mechanical Engineers, Part C: Journal of Mechanical Engineering Science*, 2013.

[49] M. Starkey and R. Williams, "Capstan as a Mechanical Amplifier," in *ASME 2011 International Design Engineering Technical Conferences & Computers and Information in Engineering Conference*, Washington, DC, 2011.

[50] M. Starkey, "Investigation of Capstan Friction and its Potential Use as a Mechanical Amplifier," Ohio University, 2010.

[51] A. Codourey, "Dynamic Modelling and Mass Matrix Evaluation of the DELTA Parallel Robot for Axes Decoupling Control," in *IEEE/RSJ International Conference on Intelligent Robots and Systems*, 1996.

[52] A. Olsson, "Modeling and Control of a Delta-3 Robot," Lund University, Lund Sweden, 2009.

Appendix A

Delta Kinematics

The delta kinematics of this Appendix were derived from the equations presented by Codourey, A. in Dynamic Modelling and Mass Matrix Evaluation of the DELTA Parallel Robot for Axes Decoupling Control [51] and Olsson, A. in Modeling and Control of a Delta-3 Robot [52]. However, the equations were modified to more accurately represent the haptic interface, which includes modified coordinate frames and geometric parameters.

A.1 Geometric Parameters

To define the kinematics of the delta configuration, geometric parameters needed to be defined to fully characterize the design. However, one of the issues with parallel structures is that they form a closed kinematic loop as opposed to serial structures which form an open kinematic loop. As a result the kinematics of parallel structures are significantly more difficult to solve. In order to simplify the model and reduce the complexity of the kinematics certain model assumptions were made. A particular property unique to the delta parallel mechanism is that the parallel linkages, represented by the color coded joints in Figure 3.3, constrain the end effector so that the end effector link and its reference frame always remain parallel to the base link and its corresponding frame. As a result, no relative rotation occurs between the end effector frame {E} and the base frame {B} thus the frames only translate with respect to one another. In doing so the mechanism decouples any rotations of the end effector, such as a joystick, from the translations of the device, which simplifies the control and facilitates modularity in terms of implementing different end effectors. More importantly, by assuming that the end effector frame only translates with respect to the base frame then the parallelogram linkages shown in Figure 3.3 can be approximated by a single linkage terminated at both ends by two perpendicular, collocated revolute joints that are perpendicular to the axis of the linkage. This approximation is represented in Figure A.1 by points $\mathbf{p_{2i}}$ and $\mathbf{p_{3i}}$ in addition to the geometric parameters defining the overall design. Only one serial chain of the parallel structure is defined as each of the chains are dimensionally identical and equally spaced about the base frame. To differentiate the chains each is

identified by an index i which increments counterclockwise about the base frame z axis from 1 to 3 beginning with the chain aligned with the y axis. For each respective chain, link 1 is defined as the base link which is common to all three chains connecting points $\mathbf{p_{1i}}$, link 2 is defined from point $\mathbf{p_{1i}}$ to $\mathbf{p_{2i}}$, link 3 is defined from $\mathbf{p_{2i}}$ to $\mathbf{p_{3i}}$, and link 4 is defined as the end effector link which is also common to all three chains connecting points $\mathbf{p_{3i}}$. Furthermore, the input to each serial chain is represented here by the angle θ_i where the point $\mathbf{p_{1i}}$ is the actuated joint and link 2 is the actuated link.

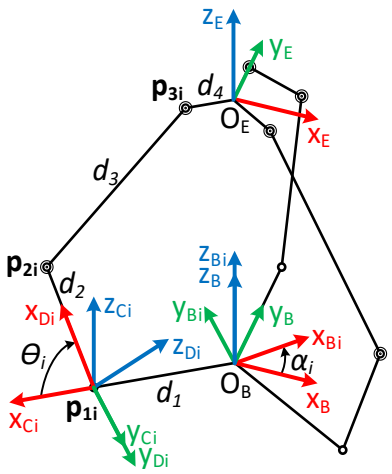

Figure A.1: Simplified delta mechanism defining the geometric parameters and coordinate frames.

Three additional coordinate frames, in addition to the base and end effector frame, are defined for each respective chain. Here each chain is designated a corresponding frame $\{B_i\}$ that coincides with the base frame $\{B\}$ but is rotated about its z axis by an angle $\alpha_1 = 90°$, $\alpha_2 = 210°$, and $\alpha_3 = 330°$ for each chain respectively. Thus the frames $\{B_i\}$ are oriented such that their corresponding x axis points towards its respective chain. The coordinate frames $\{C_i\}$ for $i = 1,2,3$ are oriented identically to the frames $\{B_i\}$ but their origins coincide with the actuated joints, points $\mathbf{p_{1i}}$. Thus their y-axis is collinear with the axis of rotation of the corresponding joint. The coordinate frame $\{D_i\}$ for $i = 1,2,3$ is oriented such that its origin is also collocated with point $\mathbf{p_{1i}}$ and its y axis is collinear to the axis of rotation, however its x axis is aligned with link 2 such that it intersects point $\mathbf{p_{2i}}$.

Below is another figure further clarifying the coordinate frames on the base and end effector links. As shown the origins of both the base and end effector frames are located at the convergence points of the three serial chains with the y axis pointing towards serial chain $i = 1$ and the z axis normal to the surface of the links.

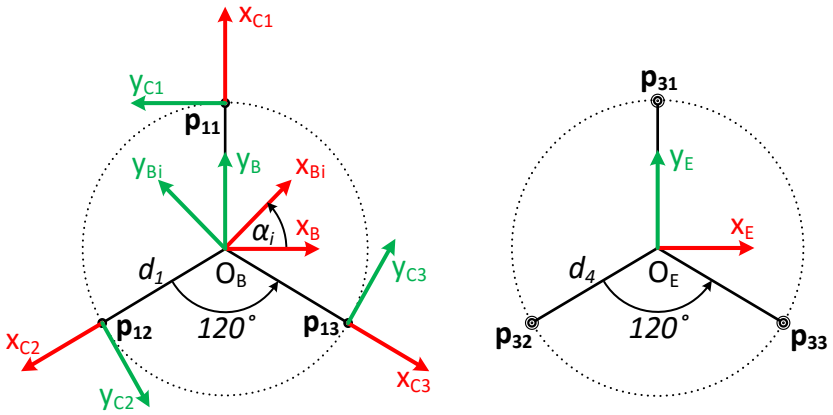

Figure A.2: Top view of the delta mechanism base and end effector frames.

Since the base frame and end effector frame never rotate with respect to one another and each of the chains are dimensionally identical and equally spaced about the base frame z axis, each of the chains can be translated inward by the dimension d_4 so that the points $\mathbf{p_{3i}}$, where $i = 1, 2, 3$, coincide at a single point, $\mathbf{p_3}$. This model simplification, which can be seen in the following figure, significantly reduces the complexity of the kinematics as will be seen in their formulation.

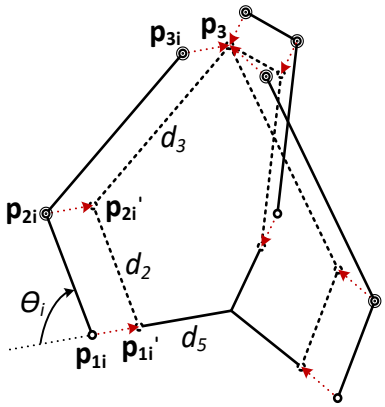

Figure A.3: Model simplification used to streamline the analysis of the delta mechanism.

By implementing this simplification, a new geometric parameter is defined which accounts for the translated distance and is given by the following equation.

$$d_5 = d_1 - d_4 \tag{A.1}$$

A.2 Forward Position Kinematics

The position of the end effector in Cartesian space is determined from the actuated joint positions in joint space via the forward position kinematics. The forward position kinematics for a parallel structure vary from the typical forward position kinematics of a serial structure as not all of the joint positions are measured. Specifically for the delta configuration, only the

joint positions of the actuated joints are measured. As a result, a different scheme must be implemented to solve for the end effector position. For the delta configuration, the position of the point $\mathbf{p_{2i}}'$ is known and the linkage length from $\mathbf{p_{2i}}'$ to $\mathbf{p_3}$ is also known, d_3. Thus the forward kinematics can be solved via the intersection of three spheres with radius d_3 and centers at points $\mathbf{p_{2i}}'$ for $i = 1, 2, 3$. The equations for the spheres can be formulated in a set of constraint equations linking the Cartesian and joint space variables given by

$$\left\| {}_{B}\mathbf{r}_{i} \right\|_2^2 - d_3^2 = {}_{B}\mathbf{r}_{i}^{T}\, {}_{B}\mathbf{r}_{i} - d_3^2 = 0 \tag{A.2}$$

where ${}_{B}\mathbf{r}_{i}$ is a vector representative of the sphere radius from the point ${}_{B}\mathbf{p}_{2i}'$ to the end effector position ${}_{B}\mathbf{p}_{3}$ for $i = 1,2,3$ as shown below.

$${}_{B}\mathbf{r}_{i} = {}_{B}\mathbf{p}_{3i} - {}_{B}\mathbf{p}_{2i} = {}_{B}\mathbf{p}_{3} - {}_{B}\mathbf{p}_{2i}' \tag{A.3}$$

Defining the center of the spheres $\mathbf{p_{2i}}'$ begins in the frame $\{B_i\}$ for $i = 1, 2, 3$ which results in the following equation.

$${}_{B_i}\mathbf{p_{2i}}'(\theta_i) = \begin{bmatrix} d_5 \\ 0 \\ 0 \end{bmatrix} + \begin{bmatrix} d_2\cos(\theta_i) \\ 0 \\ d_2\sin(\theta_i) \end{bmatrix} = \begin{bmatrix} d_5 + d_2\cos(\theta_i) \\ 0 \\ d_2\sin(\theta_i) \end{bmatrix} \tag{A.4}$$

To be used in the constraint equation ${}_{B_i}\mathbf{p_{2i}}'$ must be transformed from the frame $\{B_i\}$ to the base reference frame $\{B\}$ which is accomplished by the rotation matrix ${}^{B_i}_{B}\mathbf{R}$:

$${}^{B_i}_{B}\mathbf{R}(\alpha_i) = \mathbf{R_z}(\alpha_i) = \begin{bmatrix} \cos(\alpha_i) & -\sin(\alpha_i) & 0 \\ \sin(\alpha_i) & \cos(\alpha_i) & 0 \\ 0 & 0 & 1 \end{bmatrix} \tag{A.5}$$

Pre-multiplying ${}_{B_i}\mathbf{p_{2i}}'$ by the rotation matrix ${}^{B_i}_{B}\mathbf{R}$ results in

$${}_{B}\mathbf{p_{2i}}' = {}^{B_i}_{B}\mathbf{R}\, {}_{B_i}\mathbf{p_{2i}}' \tag{A.6}$$

where ${}_{B}\mathbf{p_{2i}}'$ is the location of the point $\mathbf{p_{2i}}'$ in the base frame $\{B\}$, which when expanded into its constituent components appears as shown in equation A.7.

$${}_{B}\mathbf{p_{2i}}'(\theta_i) = \begin{bmatrix} (d_5 + d_2\cos(\theta_i))\cos(\alpha_i) \\ (d_5 + d_2\cos(\theta_i))\sin(\alpha_i) \\ d_2\sin(\theta_i) \end{bmatrix} \tag{A.7}$$

Now ${}_{B}\mathbf{r}_{i}$ can be defined in terms of its own constituent components resulting in

$$ {}_{B}\mathbf{r}_{i} = \begin{bmatrix} x \\ y \\ z \end{bmatrix} - {}^{B_i}_{B}\mathbf{R} \begin{bmatrix} d_5 + d_2\cos(\theta_i) \\ 0 \\ d_2\sin(\theta_i) \end{bmatrix} \tag{A.8} $$

$$ {}_{B}\mathbf{r}_{i} = \begin{bmatrix} x - (d_5 + d_2\cos(\theta_i))\cos(\alpha_i) \\ y - (d_5 + d_2\cos(\theta_i))\sin(\alpha_i) \\ z - d_2\sin(\theta_i) \end{bmatrix} \tag{A.9} $$

where the point $\mathbf{p_3}$ is represented by the end effector coordinates in Cartesian space as x, y, and z. The equations for the three spheres can now be expressed in a more familiar form as

$$ \begin{cases} 1\colon (x - x_1)^2 + (y - y_1)^2 + (z - z_1)^2 = d_3^2 \\ 2\colon (x - x_2)^2 + (y - y_2)^2 + (z - z_2)^2 = d_3^2 \\ 3\colon (x - x_3)^2 + (y - y_3)^2 + (z - z_3)^2 = d_3^2 \end{cases} \tag{A.10} $$

where for notation simplification, the coordinates of points ${}_{B}\mathbf{p_{21}}'$, ${}_{B}\mathbf{p_{22}}'$, and ${}_{B}\mathbf{p_{23}}'$ are designated as (x_1, y_1, z_1), (x_2, y_2, z_2), and (x_3, y_3, z_3) respectively. Expanding these equations results in the three equations of A.11.

$$ \begin{cases} 1\colon x^2 + y^2 + z^2 + x_1^2 + y_1^2 + z_1^2 - 2x_1x - 2y_1y - 2z_1z = d_3^2 \\ 2\colon x^2 + y^2 + z^2 + x_2^2 + y_2^2 + z_2^2 - 2x_2x - 2y_2y - 2z_2z = d_3^2 \\ 3\colon x^2 + y^2 + z^2 + x_3^2 + y_3^2 + z_3^2 - 2x_3x - 2y_3y - 2z_3z = d_3^2 \end{cases} \tag{A.11} $$

In an effort to further simply the equations, another constant w_i for $i = 1,2,3$ is defined as shown below.

$$ w_i = x_i^2 + y_i^2 + z_i^2 \tag{A.12} $$

Incorporating this constant, and subtracting equation 2 of A.11 from 1 of A.11 and equation 3 of A.11 from 1 of A.11 results in the following two linear relations in terms of x, y, and z.

$$ \begin{cases} 1 - 2\colon (x_1 - x_2)x + (y_1 - y_2)y + (z_1 - z_2)z = (w_1 - w_2)/2 \\ 1 - 3\colon (x_1 - x_3)x + (y_1 - y_3)y + (z_1 - z_3)z = (w_1 - w_3)/2 \end{cases} \tag{A.13} $$

Solving this linear system of two equations for x and y in terms of z results in

$$ \begin{cases} 6\colon x = a_x z + b_x \\ 7\colon y = a_y z + b_y \end{cases} \tag{A.14} $$

where the coefficients a_x, b_x, a_y, and b_y are defined by the following equations.

$$ \begin{cases} a_x = \frac{(z_1 - z_2)(y_1 - y_3) - (z_1 - z_3)(y_1 - y_2)}{(x_1 - x_3)(y_1 - y_2) - (x_1 - x_2)(y_1 - y_3)} \\ b_x = \frac{-(w_1 - w_2)(y_1 - y_3) + (w_1 - w_3)(y_1 - y_2)}{2\left((x_1 - x_3)(y_1 - y_2) - (x_1 - x_2)(y_1 - y_3)\right)} \end{cases} \tag{A.15} $$

$$\begin{cases} a_y = \frac{-(z_1-z_2)(x_1-x_3)+(z_1-z_3)(x_1-x_2)}{(x_1-x_3)(y_1-y_2)-(x_1-x_2)(y_1-y_3)} \\ b_y = \frac{(w_1-w_2)(x_1-x_3)-(w_1-w_3)(x_1-x_2)}{2\left((x_1-x_3)(y_1-y_2)-(x_1-x_2)(y_1-y_3)\right)} \end{cases} \tag{A.16}$$

Substituting the equations from A.14 into sphere equation 1 of A.11 results in the following quadratic equation in terms of z.

$$\begin{aligned} \left(a_x^2 + a_y^2 + 1\right)z^2 + 2\left(a_x(b_x - x_1) + a_y\left(b_y - y_1\right) - z_1\right)z \\ + \left((b_x - x_1)^2 + \left(b_y - y_1\right)^2 + z_1^2 - d_3^2\right) = 0 \end{aligned} \tag{A.17}$$

This equation has the traditional form of

$$az^2 + bz + c = 0 \tag{A.18}$$

where the coefficients a, b, and c are defined by the following equations

$$\begin{cases} a = a_x^2 + a_y^2 + 1 \\ b = 2\left(a_x(b_x - x_1) + a_y\left(b_y - y_1\right) - z_1\right) \\ c = (b_x - x_1)^2 + \left(b_y - y_1\right)^2 + z_1^2 - d_3^2 \end{cases} \tag{A.19}$$

This quadratic equation can solved for z via the quadratic formula. However, prior to deriving the solution, the discriminant must be checked to ensure there is a real, existing point in which the spheres intersect. This is accomplished by calculating the discriminant as shown in the following equation.

$$b^2 - 4ac \geq 0 \tag{A.20}$$

If a real existing point exists then z can be solved for using the traditional quadratic formula given by A.21.

$$z = \frac{-b+\sqrt{b^2-4ac}}{2a} \tag{A.21}$$

Notice that the quadratic formula presented here only considers one root as opposed to two. This is a result of the fact that the actual solution will always be the greater of the two roots, thus this is accounted for in the equation. Once the z is known it can be substituted into the linear equations from A.14 to get the corresponding x and y coordinates.

A.3 Forward Velocity Kinematics

The velocity of the end effector in Cartesian space is determined from the actuated joint velocities in joint space via the forward velocity kinematics. In defining the velocity kinematics, it is typically desired to formulate the Jacobian matrix which maps the joint space velocities to the Cartesian space velocities. The Jacobian is simply a matrix consisting of the partial derivatives of the kinematic equations. In order to formulate the Jacobian matrix for the delta configuration, the first time derivative of the constraint equations linking the Cartesian and joint space variables is derived resulting in equation A.22.

$$\frac{d(\mathbf{r_i}^{\mathbf{T}}\mathbf{r_i}-d_3^2)}{dt} = \dot{\mathbf{r}}_\mathbf{i}^{\mathbf{T}}\mathbf{r_i} + \mathbf{r_i}^{\mathbf{T}}\dot{\mathbf{r}}_\mathbf{i} = 0 \tag{A.22}$$

This equation can then be reduced according to the commutative property resulting in equation A.23

$$\dot{\mathbf{r}}_\mathbf{i}^{\mathbf{T}}\mathbf{r_i} = \mathbf{r_i}^{\mathbf{T}}\dot{\mathbf{r}}_\mathbf{i} = 0 \tag{A.23}$$

where $\dot{\mathbf{r}}_\mathbf{i}$ is defined as shown in equation A.24.

$$\dot{\mathbf{r}}_\mathbf{i} = \begin{bmatrix}\dot{x}\\ \dot{y}\\ \dot{z}\end{bmatrix} - {}^{\mathrm{B_i}}_{\mathrm{B}}\mathbf{R}\begin{bmatrix}-d_2\sin(\theta_i)\\ 0\\ d_2\cos(\theta_i)\end{bmatrix}\dot{\theta}_i \tag{A.24}$$

In order to simplify the notation the equation for the first time derivative of $\mathbf{r_i}$ can be rewritten as equation A.25

$$\dot{\mathbf{r}}_\mathbf{i} = \dot{\mathbf{x}} - \mathbf{b_i}\dot{\theta}_i \tag{A.25}$$

where $\mathbf{b_i}$ and $\dot{\mathbf{x}}$ are defined as shown below.

$$\mathbf{b_i} = {}^{\mathrm{B_i}}_{\mathrm{B}}\mathbf{R}\begin{bmatrix}-d_2\sin(\theta_i)\\ 0\\ d_2\cos(\theta_i)\end{bmatrix} \tag{A.26}$$

$$\dot{\mathbf{x}} = \begin{bmatrix}\dot{x}\\ \dot{y}\\ \dot{z}\end{bmatrix} \tag{A.27}$$

Substituting this equation into the previous equation results in

$$\mathbf{r_i}^{\mathbf{T}}\dot{\mathbf{x}} - \mathbf{r_i}^{\mathbf{T}}\mathbf{b_i}\dot{\theta}_i = 0 \tag{A.28}$$

for one serial chain whereas accounting for all three chains results in the matrix form given by

$$\begin{bmatrix} \mathbf{r_1^T} \\ \mathbf{r_2^T} \\ \mathbf{r_3^T} \end{bmatrix} \dot{\mathbf{x}} - \begin{bmatrix} \mathbf{r_1^T b_1} & 0 & 0 \\ 0 & \mathbf{r_2^T b_2} & 0 \\ 0 & 0 & \mathbf{r_3^T b_3} \end{bmatrix} \dot{\mathbf{q}} = \begin{bmatrix} 0 \\ 0 \\ 0 \end{bmatrix} \tag{A.29}$$

where $\dot{\mathbf{q}}$ is defined as the vector of joint velocities given by equation A.30.

$$\dot{\mathbf{q}} = \begin{bmatrix} \dot{\theta}_1 \\ \dot{\theta}_2 \\ \dot{\theta}_3 \end{bmatrix} \tag{A.30}$$

In order to finally derive the Jacobian matrix, the previously presented equation must be manipulated to take the standard form defined by the following equation

$$\dot{\mathbf{x}} = \mathbf{J}\dot{\mathbf{q}} \tag{A.31}$$

where $\mathbf{J}$ is the Jacobian matrix. This results in the following equation defining the Jacobian.

$$\mathbf{J} = \begin{bmatrix} \mathbf{r_1^T} \\ \mathbf{r_2^T} \\ \mathbf{r_3^T} \end{bmatrix}^{-1} \begin{bmatrix} \mathbf{r_1^T b_1} & 0 & 0 \\ 0 & \mathbf{r_2^T b_2} & 0 \\ 0 & 0 & \mathbf{r_3^T b_3} \end{bmatrix} \tag{A.32}$$

It is worth noting that the Jacobian matrix for serial kinematic chains are typically dependent on the joint positions only. However in this case, since not all of the joint positions are known, the Jacobian becomes dependent on the end effector position as well. As a result, the forward position kinematics must be calculated prior to calculating the Jacobian and the corresponding forward velocity kinematics.

A.4 Forward Acceleration Kinematics

The acceleration of the end effector in Cartesian space is determined from the actuated joint accelerations in joint space via the forward acceleration kinematics. The formulation of the forward acceleration kinematics is similar to the forward velocity kinematics, however the second time derivative of the constraint equations is derived as shown here.

$$\frac{d^2(\mathbf{r_i^T r_i} - d_3^2)}{dt^2} = \dot{\mathbf{r}}_\mathbf{i}^\mathbf{T}\dot{\mathbf{r}}_\mathbf{i} + \mathbf{r}_\mathbf{i}^\mathbf{T}\ddot{\mathbf{r}}_\mathbf{i} = 0 \tag{A.33}$$

The second time derivative of $\ddot{\mathbf{r}}_\mathbf{i}$ can be found by taking another time derivative of the previous equation resulting in equation A.34.

$$\ddot{\mathbf{r}}_\mathbf{i} = \ddot{\mathbf{x}} - \dot{\mathbf{b}}_\mathbf{i}\dot{\theta}_i - \mathbf{b}_\mathbf{i}\ddot{\theta}_i \tag{A.34}$$

Substituting $\ddot{\mathbf{r}}_\mathbf{i}$ and $\dot{\mathbf{r}}_\mathbf{i}$ into the equation and manipulating the variables results in

$$\mathbf{r_i^T}\ddot{\mathbf{x}} + \dot{\mathbf{r}}_\mathbf{i}^\mathbf{T}\dot{\mathbf{x}} - \mathbf{r_i^T b_i}\ddot{\theta}_i - \left(\dot{\mathbf{r}}_\mathbf{i}^\mathbf{T}\mathbf{b_i} + \mathbf{r_i^T}\dot{\mathbf{b}}_\mathbf{i}\right)\dot{\theta}_i = 0 \tag{A.35}$$

for a single serial chain. This equation can be written in matrix form for all three chains as shown below.

$$\begin{bmatrix}\mathbf{r_1^T}\\ \mathbf{r_2^T}\\ \mathbf{r_3^T}\end{bmatrix}\ddot{\mathbf{x}} + \begin{bmatrix}\dot{\mathbf{r}}_\mathbf{1}^\mathbf{T}\\ \dot{\mathbf{r}}_\mathbf{2}^\mathbf{T}\\ \dot{\mathbf{r}}_\mathbf{3}^\mathbf{T}\end{bmatrix}\dot{\mathbf{x}} - \begin{bmatrix}\mathbf{r_1^T b_1} & 0 & 0\\ 0 & \mathbf{r_2^T b_2} & 0\\ 0 & 0 & \mathbf{r_3^T b_3}\end{bmatrix}\ddot{\mathbf{q}} - \begin{bmatrix}\dot{\mathbf{r}}_\mathbf{1}^\mathbf{T}\mathbf{b_1} + \mathbf{r_1^T}\dot{\mathbf{b}}_\mathbf{1} & 0 & 0\\ 0 & \dot{\mathbf{r}}_\mathbf{2}^\mathbf{T}\mathbf{b_2} + \mathbf{r_2^T}\dot{\mathbf{b}}_\mathbf{2} & 0\\ 0 & 0 & \dot{\mathbf{r}}_\mathbf{3}^\mathbf{T}\mathbf{b_3} + \mathbf{r_3^T}\dot{\mathbf{b}}_\mathbf{3}\end{bmatrix}\dot{\mathbf{q}} = \begin{bmatrix}0\\0\\0\end{bmatrix} \tag{A.36}$$

Solving for $\ddot{\mathbf{x}}$ results in

$$\ddot{\mathbf{x}} = \dot{\mathbf{J}}\dot{\mathbf{q}} + \mathbf{J}\ddot{\mathbf{q}} \tag{A.37}$$

where the first time derivative of the Jacobian is given by

$$\dot{\mathbf{J}} = \begin{bmatrix}\mathbf{r_1^T}\\ \mathbf{r_2^T}\\ \mathbf{r_3^T}\end{bmatrix}^{-1}\left(-\begin{bmatrix}\dot{\mathbf{r}}_\mathbf{1}^\mathbf{T}\\ \dot{\mathbf{r}}_\mathbf{2}^\mathbf{T}\\ \dot{\mathbf{r}}_\mathbf{3}^\mathbf{T}\end{bmatrix}\mathbf{J} + \begin{bmatrix}\dot{\mathbf{r}}_\mathbf{1}^\mathbf{T}\mathbf{b_1} + \mathbf{r_1^T}\dot{\mathbf{b}}_\mathbf{1} & 0 & 0\\ 0 & \dot{\mathbf{r}}_\mathbf{2}^\mathbf{T}\mathbf{b_2} + \mathbf{r_2^T}\dot{\mathbf{b}}_\mathbf{2} & 0\\ 0 & 0 & \dot{\mathbf{r}}_\mathbf{3}^\mathbf{T}\mathbf{b_3} + \mathbf{r_3^T}\dot{\mathbf{b}}_\mathbf{3}\end{bmatrix}\right) \tag{A.38}$$

A.5 Inverse Position Kinematics

The position of the joints is determined from the position of the end effector in Cartesian space via the inverse position kinematics. The formulation of the inverse position kinematics is similar to the forward position kinematics in terms of the equations used, however the joint positions are solved for as opposed to the end effector position. Here the expanded constraint equations that are used are shown.

$$\begin{aligned}&(x - (d_5 + d_2\cos(\theta_i))\cos(\alpha_i))^2\\ &+(y - (d_5 + d_2\cos(\theta_i))\sin(\alpha_i))^2\\ &+(z - d_2\sin(\theta_i))^2 - d_3^2 = 0\end{aligned} \tag{A.39}$$

These equations can be reduced by first expanding and then substituting the following two trigonometric identities

$$\begin{cases}\cos(\theta_i)^2 + \sin(\theta_i)^2 = 1\\ \cos(\alpha_i)^2 + \sin(\alpha_i)^2 = 1\end{cases} \tag{A.40}$$

which after simplification results in

$$\begin{aligned}(2d_2z)\sin(\theta_i) - \big(2d_2(d_5 - x\cos(\alpha_i) - y\sin(\alpha_i))\big)\cos(\theta_i) \\ = \big(x^2 + y^2 + z^2 + d_2^2 - d_3^2 + d_5^2 - 2d_5(x\cos(\alpha_i) + y\sin(\alpha_i))\big)\end{aligned} \tag{A.41}$$

where the right side of the equation is constant. This equation can now be manipulated to take the form presented below

$$a\sin(\theta_i) - b_i\cos(\theta_i) = A_i\sin(\theta_i - \beta_i) = c_i \tag{A.42}$$

where coefficients a, b_i, and c_i are given by equation A.43 for $i = 1, 2, 3$.

$$\begin{cases} a = 2d_2z \\ b_i = 2d_2(d_5 - x\cos(\alpha_i) - y\sin(\alpha_i)) \\ c_i = x^2 + y^2 + z^2 + d_2^2 - d_3^2 + d_5^2 - 2d_5(x\cos(\alpha_i) + y\sin(\alpha_i)) \end{cases} \tag{A.43}$$

Solving for A_i and β_i from equation A.42 in terms of coefficients a, b_i, and c_i results in equation A.44.

$$\begin{cases} A_i = \sqrt{a^2 + {b_i}^2} \\ \beta_i = \tan^{-1}\left(\frac{b_i}{a}\right) \end{cases} \tag{A.44}$$

Then finally solving for the input joint position θ_i results in equation A.45.

$$\theta_i = \sin^{-1}\left(\frac{c_i}{A_i}\right) + \beta_i \tag{A.45}$$

As opposed to the forward position kinematics, a discriminant is not calculated thus there is no defined way to ensure the resolved joint position is real or achievable. To circumvent this issue each of the three resolved joint positions is checked to ensure it lies in the range of motion of the joint. If just one of the three joints results in a non-existent position then the entire result for that end effector position is deemed indeterminate.

Appendix B

Delta Dynamics

The delta dynamics of this Appendix were derived from the equations presented by Codourey, A. in Dynamic Modelling and Mass Matrix Evaluation of the DELTA Parallel Robot for Axes Decoupling Control [51] and Olsson, A. in Modeling and Control of a Delta-3 robot [52]. However, the equations were modified to more accurately represent the haptic interface, which includes modified coordinate frames and dynamic parameters.

B.1 Dynamic Parameters

To derive the dynamics of the delta configuration, dynamic parameters were defined to fully characterize the design. However, analogous to the kinematics, the closed loop structure of this parallel mechanism significantly increases the complexity of the dynamics. In order to simplify the model, certain model simplifications were made. In this case the complexity originates from the movement of the passive parallelogram linkages represented by link 3 for each respective chain. Thus it is ideal if these linkages were removed from the model altogether. This can be accomplished with little impact to the model accuracy by assuming that the mass of these linkages can be broken into two parts and placed at its extremes, $\mathbf{p_{2i}}$ and $\mathbf{p_{3i}}$, for each chain. Since these linkages can be approximated as rods, their inertia about one end takes the form

$$I_{3i} = \frac{1}{3} m_{3i} d_3^2 \tag{B.1}$$

where m_{3i} is the mass of the linkage and I_{3i} is its inertia. Thus in an attempt to preserve the inertia of the linkages the masses can be partitioned such that $1/3$ of the mass is at point $\mathbf{p_{3i}}$ and $2/3$ is at $\mathbf{p_{2i}}$. Despite the mass of the linkages being broken into two parts, the forces from the actuated joints to the end effector still act along the direction defined by their respective linkage.

In order to incorporate this model simplification, the additional mass has to be accounted for on the respective links. As a result the effective mass of the end effector $\bar{m}_4$ is given by the following equation

$$\bar{m}_4 = m_4 + \sum_{i=1}^{3}(1-r)m_{3i} + m_p \tag{B.2}$$

where m_4 is the nominal link 4 mass, m_{3i} is the mass of each respective link 3, m_p is the mass of any additional payload, and r is the ratio of link 3's mass at the point $\mathbf{p_{2i}}$ which in this case is $2/3$. It is worth noting that the mass m_{3i} is a factor of the chain index in order to account for the additional mass resulting from cable routing along specific linkages.

The effective mass $\bar{m}_{2i}$ of the actuated link, link 2, for each respective chain is given by

$$\bar{m}_{2i} = m_2 + rm_{3i} \tag{B.3}$$

where m_2 is the nominal link 2 mass. This mass allocation has the effect of shifting the effective centroid for link 2, which must be accounted for. Figure B.1 below details the mass distribution of link 2 where each component is labeled with its corresponding mass and respective coordinates in the frame {D_i}.

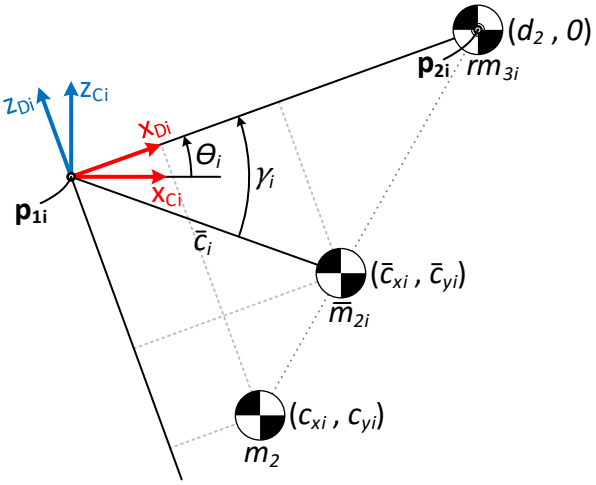

Figure B.1: Mass distribution of link 2 accounting for model simplifications.

The location of the effective centroid in terms of Cartesian coordinates is defined by $\bar{c}_{xi}$ and $\bar{c}_{yi}$ using the masses as weighting as shown below.

$$\bar{c}_{xi} = \frac{m_{2i}c_{xi} + rm_{3i}d_2}{\bar{m}_{2i}} \tag{B.4}$$

$$\bar{c}_{yi} = \frac{m_{2i}c_{yi}}{\bar{m}_{2i}} \tag{B.5}$$

However, in terms of implementation it is desired to have the location of the centroid defined in terms of polar coordinates, resulting in

$$\gamma_i = \tan^{-1}\left(\frac{\bar{c}_{yi}}{\bar{c}_{xi}}\right) \tag{B.6}$$

$$\bar{c}_i = \sqrt{\bar{c}_{xi}^2 + \bar{c}_{yi}^2} \tag{B.7}$$

where γ_{ci} is the offset angle from the x axis and d_{ci} is the distance from the coordinate frame origin, $\mathbf{p_{1i}}$, to the corresponding centroid. These equations are especially useful in terms of compensating for gravitational effects, which will be seen shortly in defining the dynamic equations.

The effective inertia $\bar{I}_{2i}$ of link 2 also becomes a function of the mass m_{3i} as shown below

$$\bar{I}_{2i} = I_{2i} + I_{mi}k_r^2 + rm_{3i}d_2^2 \tag{B.8}$$

where I_{2i} is the nominal link 2 inertia, I_{mi} is the motor inertia, and k_r is the gear transmission constant. The inertial values for each chain can then be expressed in matrix form as shown below.

$$\mathbf{\bar{I}_2} = \begin{bmatrix} \bar{I}_{21} & 0 & 0 \\ 0 & \bar{I}_{22} & 0 \\ 0 & 0 & \bar{I}_{23} \end{bmatrix} \tag{B.9}$$

It is worth noting, and can be easily realized here, that it is desirable to reduce the motor inertia and gear ratio as much as possible as it has a direct and significant impact on the inertia of the device.

B.2 Inverse Dynamics

The torques in joint space required to reflect a desired force at the end effector in Cartesian space are determined via the inverse dynamics. The inverse dynamics, especially for a parallel structure as complex as the delta configuration, are typically difficult to define. However, a useful principle in defining the dynamics is known as the virtual work principle. Virtual work, in this case, consists of a force or torque multiplied by a corresponding infinitesimal displacement. It is practical in that the virtual work performed by the end effector in Cartesian space is equivalent to the virtual work performed by the actuated joints in joint space as demonstrated by the following equation.

$$\mathbf{f}^{\mathrm{T}}\delta\mathbf{x} = \boldsymbol{\tau}^{\mathrm{T}}\delta\mathbf{q} \tag{B.10}$$

where $\mathbf{f}$ is the forces acting on the end effector, $\delta\mathbf{x}$ is the infinitesimal Cartesian displacements, $\boldsymbol{\tau}$ is the torques acting on the joints, and $\delta\mathbf{q}$ is the infinitesimal joint displacements. In order to relate the infinitesimal Cartesian and joint displacements, the

forward velocity equation previously presented can be expressed in terms of virtual displacements resulting in equation B.11.

$$\delta\mathbf{x} = \mathbf{J}\delta\mathbf{q} \tag{B.11}$$

Substituting this equation into the virtual work equation and manipulating the variables results in equation B.12.

$$\boldsymbol{\tau} = \mathbf{J}^{\mathrm{T}} \cdot \mathbf{f} \tag{B.12}$$

As can be concluded from the equation, the Jacobian is especially significant because it can not only be used to map the joint space velocities to Cartesian space velocities, but it can also be used to map the Cartesian space forces to joint space torques and vice versa.

In this case, there are three forces acting on the mechanism that have to be mapped into joint space: gravitational forces, inertial forces, and the external disturbance from the user. The gravitational forces will first be defined. The magnitude and direction of the acceleration of gravity will be represented by a scalar and a unit vector respectively provided by the following equations.

$$g = 9.80665 \tag{B.13}$$

$$_{\mathrm{B}}\mathbf{g} = g\begin{bmatrix} 0 \\ 0 \\ -1 \end{bmatrix} \tag{B.14}$$

In this case, gravity will be defined in the negative z direction with respect to the base frame. Thus the effective gravitational forces seen by link 2, $_{\mathrm{B}}\mathbf{f_{g1i}}$, and link 4, $_{\mathrm{B}}\mathbf{f_{g2}}$, will be defined as in equations B.15 and B.16 respectively.

$$_{\mathrm{B}}\mathbf{f_{g1i}} = \bar{m}_{2i}\ {}_{\mathrm{B}}\mathbf{g} \tag{B.15}$$

$$_{\mathrm{B}}\mathbf{f_{g2}} = \bar{m}_{4}\ {}_{\mathrm{B}}\mathbf{g} \tag{B.16}$$

The resultant torque due to the gravitational force $_{\mathrm{B}}\mathbf{f_{g1i}}$ can be found by first defining the location of the centroids in the frames $\{C_i\}$ which results in equation B.17.

$$_{\mathrm{C_i}}\mathbf{p_{ci}}(\theta_i) = \begin{bmatrix} \bar{c}_i \cos(\theta_i - \gamma_i) \\ 0 \\ \bar{c}_i \sin(\theta_i - \gamma_i) \end{bmatrix} \tag{B.17}$$

Seeing as the gravitational forces $_{\mathrm{B}}\mathbf{f_{g1i}}$ are defined in terms of the base frame, they must be transformed into the $\{C_i\}$ frame using a rotation matrix as shown below.

$$ {}^{B}_{C_i}\mathbf{R}(\alpha_i) = {}^{B_i}_{B}\mathbf{R}^{T}(\alpha_i) \tag{B.18} $$

$$ {}_{C_i}\mathbf{f_{g1i}} = {}^{B}_{C_i}\mathbf{R}\ {}_{B}\mathbf{f_{g1i}} \tag{B.19} $$

The torque do to the eccentric mass can then be determined by taking the cross product of the centroid location and the gravitational force acting through the centroid in each respective $\{C_i\}$ frame. Arranging the cross products in a column vector for each chain results in the first gravitational term given by equation B.20.

$$ \boldsymbol{\tau}_{\mathbf{g1}} = \begin{bmatrix} {}_{C_1}\mathbf{p_{c1}} \times {}_{C_1}\mathbf{f_{g11}} \\ {}_{C_2}\mathbf{p_{c2}} \times {}_{C_2}\mathbf{f_{g12}} \\ {}_{C_3}\mathbf{p_{c3}} \times {}_{C_3}\mathbf{f_{g13}} \end{bmatrix} \tag{B.20} $$

As for the gravitation force acting at the end effector, the resulting torques can simply be found through the use of the Jacobian transpose as shown in the following equation.

$$ \boldsymbol{\tau}_{\mathbf{g2}} = \mathbf{J}^{T}\mathbf{f_{g2}} \tag{B.21} $$

Summing the two gravitation components results in the total torque $\boldsymbol{\tau}_{\mathbf{g}}$ due to gravitational effects defined by

$$ \boldsymbol{\tau}_{\mathbf{g}} = \boldsymbol{\tau}_{\mathbf{g1}} + \boldsymbol{\tau}_{\mathbf{g2}} \tag{B.22} $$

Similar to the gravitation terms, there are two inertial components that need to be defined. The first inertial term $\boldsymbol{\tau}_{\mathbf{I1}}$ accounts for the inertia of the actuated links, link 2, and is given by the following equation

$$ \boldsymbol{\tau}_{\mathbf{I1}} = \bar{\mathbf{I}}_{\mathbf{2}}\ddot{\mathbf{q}} \tag{B.23} $$

where $\ddot{\mathbf{q}}$ is the joint space accelerations. The second inertial term $\boldsymbol{\tau}_{\mathbf{I2}}$ accounts for the mass of the end effector and is given by the following equation

$$ \boldsymbol{\tau}_{\mathbf{I2}} = \mathbf{J}^{T}(\bar{m}_4\ddot{\mathbf{x}}) = \bar{m}_4\mathbf{J}^{T}\mathbf{J}\ddot{\mathbf{q}} + \bar{m}_4\mathbf{J}^{T}\dot{\mathbf{J}}\dot{\mathbf{q}} \tag{B.24} $$

where $\ddot{\mathbf{x}}$ is the Cartesian space accelerations. Here the equation for the forward acceleration kinematics, A.37, has been substituted for $\ddot{\mathbf{x}}$ to get the equation in terms of joint space variables. Summing the two inertial terms results in the total torque $\boldsymbol{\tau}_{\mathbf{I}}$ due to the inertial effects defined by equation B.25.

$$ \boldsymbol{\tau}_{\mathbf{I}} = \boldsymbol{\tau}_{\mathbf{I1}} + \boldsymbol{\tau}_{\mathbf{I2}} = (\bar{\mathbf{I}}_{\mathbf{2}} + \bar{m}_4\mathbf{J}^{T}\mathbf{J})\ddot{\mathbf{q}} + \left(\bar{m}_4\mathbf{J}^{T}\dot{\mathbf{J}}\right)\dot{\mathbf{q}} \tag{B.25} $$

The last force component that needs to be mapped into joint space is the external disturbance from the user, $\mathbf{f_e}$. The contribution of this force can simply be found through the Jacobian transpose and is provided by the following equation.

$$\boldsymbol{\tau}_\mathbf{e} = \mathbf{J}^{\mathrm{T}}\mathbf{f_e} \tag{B.26}$$

Summing all the non-inertial components and equating them to the inertial terms results in

$$\boldsymbol{\tau}_\mathbf{I} = \boldsymbol{\tau}_\mathbf{u} + \boldsymbol{\tau}_\mathbf{g} + \boldsymbol{\tau}_\mathbf{e} \tag{B.27}$$

where $\boldsymbol{\tau}_\mathbf{u}$ is the input torques to the actuated links. Expanding the inertial term and rearranging results in equation B.28.

$$(\bar{\mathbf{I}}_\mathbf{2} + \bar{m}_4\mathbf{J}^{\mathrm{T}}\mathbf{J})\ddot{\mathbf{q}} + \left(\bar{m}_4\mathbf{J}^{\mathrm{T}}\dot{\mathbf{J}}\right)\dot{\mathbf{q}} - \boldsymbol{\tau}_\mathbf{g} - \boldsymbol{\tau}_\mathbf{e} = \boldsymbol{\tau}_\mathbf{u} \tag{B.28}$$

The components of the inertial term can then be written in the more standard format

$$\mathbf{M}(\mathbf{q})\ddot{\mathbf{q}} + \mathbf{C}(\mathbf{q}, \dot{\mathbf{q}})\dot{\mathbf{q}} - \boldsymbol{\tau}_\mathbf{g}(\mathbf{q}) - \boldsymbol{\tau}_\mathbf{e}(\mathbf{q}, \mathbf{f_e}) = \boldsymbol{\tau}_\mathbf{u} \tag{B.29}$$

where $\mathbf{M}$ is the inertia matrix and $\mathbf{C}$ is the matrix comprising the centrifugal and Coriolis forces. This equation can then be used with the corresponding kinematic equations to define the required torques necessary to follow a desired end effector trajectory.